Measurement of the s-channel Single Top Quark Cross Section at the CDF Experiment and Contributions to the Evidence of $H \to bb$ at the Tevatron

Hao Liu
Jiangsu, China

B.Eng., Tsinghua University, 2008
M.Phil., The University of Hong Kong, 2011

A Dissertation presented to the Graduate Faculty
of the University of Virginia in Candidacy for the Degree of
Doctor of Philosophy

Department of Physics

University of Virginia
August, 2014

Abstract

In this thesis, we present the measurement of the s-channel single top quark production cross section. In the cross section measurement we use data generated by proton-antiproton collisions at the center-of-mass energy $\sqrt{s} = 1.96$ TeV and collected by the CDF Run II detector. The total data set corresponds to an integrated luminosity of 9.4 fb^{-1}. We select events consistent with the s-channel process including two jets identified as originating from b quarks and one leptonically decaying W boson. The observed significance is 3.8 standard deviations with respect to the background-only hypothesis. Assuming a top-quark mass of 172.5 GeV/c^2, we measure the s-channel cross section to be $1.41^{+0.44}_{-0.42}$ pb. When combined with other measurements at the CDF and D0 experiments, the observed significance increases to 6.4 standard deviations, which is interpreted as the first observation of the single top quark s-channel production process.

While the s-channel measurement is the centerpiece of this thesis, the author also contributed to the Higgs boson search. The techniques of the single top quark analysis were adapted from the search for the standard model Higgs boson produced in association with a W boson, since these two processes have the same final-state particles. The author's improvements implemented in the WH search are also described, and the final Higgs boson results are reported. 95% credibility level upper limits are set on the WH production cross section times the $H \to b\bar{b}$ branching ratio as a function of the Higgs boson mass hypothesis. First evidence of the $H \to b\bar{b}$ process is also found when all searches in this Higgs boson decay mode from the CDF and D0 experiments are combined.

Acknowledgement

First of all, I would like to thank my advisor Prof. Robert Craig Group for his encouragement and support through my PhD study. During the years, I was impressed by his passionate in particle physics and deep insight of physics problems. Nothing can be achieved in this challenging measurement without his guidance and help. I especially want thank him for all his efforts in improving my English writing.

I would also like to thank all my colleagues in the *WH* Group at the CDF experiment: Yuri Oksuzian, Federico Sforza, Zhenbin Wu, and Tom Junk. They helped me a lot in setting up the whole analysis using the powerful software framework WHAM. I also benefited a lot from the discussions with them when I encountered any problems in the analysis.

I would like to thank Prof. Bob Hirosky, Eugene Kolomeisky, and Tingting Zhang for squeezing time out of their busy schedules to serve on my thesis committee. I would also like to thank my colleagues at UVa: Chuanzhe Lin, Huong Nguyen, and Pei Wang, for all their help during my study in the beautiful Charlottesville.

Finally, I want to thank my parents for their patience, encouragement in the years of my PhD study. Without their help, I would not be in the US pursuing my PhD. I also want to thank Baiyu for sharing her life with me, especially for her accompanying during my thesis writing. It is her support that made this thesis finishing in time possible.

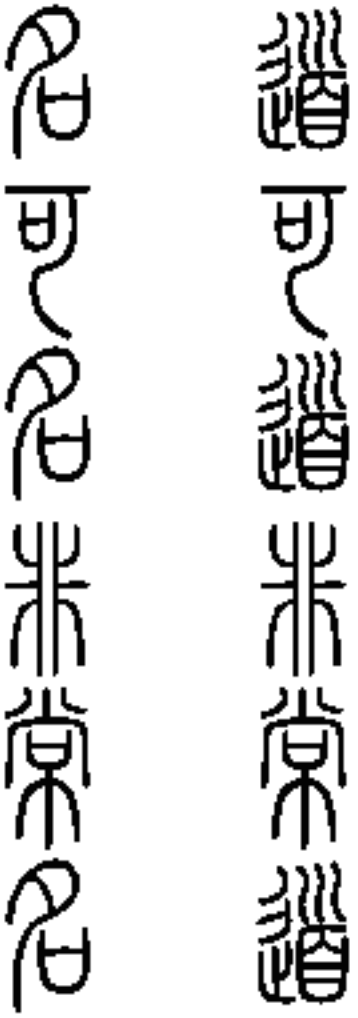

The Way that can be told of is not an unvarying way;

The names that can be named are not unvarying names.

Lǎozi *Dào Dé Jīng*

Contents

List of Figures

List of Tables

Chapter 1

Introduction

What is the fundamental structure of matter?

Humans have always asked this question to themselves. In ancient Greece, Democritus first coined the word "átomos" to denote the smallest indivisible particles of matter. Over the next thousands years, atoms were believed to be the most "fundamental" part of matter. However, in 1897 J.J Thomson discovered that every atom has electrons by the cathode ray experiment. It was the first time that substructure of atoms was observed. After considerable work by many physicists in the early 20th century, protons and neutrons were also discovered and together with electrons were believed to the fundamental particles. However, during the mid-20th century hundreds of additional "fundamental" particles were discovered, which indicated that maybe all of those particles were not truly fundamental. To solve this problem, the Standard Model (SM) theory was developed. In this theory a limited number of fundamental particles could describe the long list of discovered particles, when incorporated with the electromagnetic, weak, and strong interactions. After years of effort made by theorists and experimentalists, the Standard Model theory has been finalized and verified by a long list of particle experiments.

Nowadays, there are two colliders working at the energy frontier in the world. One is the Tevatron near Chicago, which collides protons with antiprotons at the center-of-mass energy of 1.96 TeV. The other one is the Large Hadron Collider (LHC) near Geneva with designed center-of-mass energy of 14 TeV for proton-proton collisions.

In this chapter, we first briefly discuss the Standard Model in Section 1.1.1 and then

include a more detailed discussion about theories involved in this thesis in Section 1.1.2 and 1.1.3. Finally, the current status of single top quark cross-section measurements and the Higgs boson search are discussed in Section 1.2 and 1.3.

1.1 The Standard Model

A relativistic quantum field theory has been used to describe the SM theory. This widely accepted theory is based on the group theory $SU(3) \otimes SU(2) \otimes U(1)$, where the $SU(3)$ group is for strong interaction, while the $SU(2) \otimes U(1)$ describes the electroweak interaction after spontaneous symmetry breaking by the Higgs mechanism.

The building blocks of the SM theory are the fundamental particles listed in Figure 1.1, which are treated as the excited state of quantum fields. Different particles are regulated by different types of quantum fields. Quarks and leptons are described by spin-$\frac{1}{2}$ quantum fields, while the force mediators, gauge bosons, are described by spin-1 quantum fields. In the SM, both leptons and quarks are divided into three generations. The gauge bosons, $W^{\pm}, Z^0$, and γ, mediate the electromagnetic and weak interactions, and the gluons carry the strong force.

1.1.1 The Gauge Theory

The Lagrangians used in the SM theory are required to be invariant under gauge transformation, and this type of quantum field theory is called a gauge theory. The simplest example to describe how a gauge theory incorporates interactions is Quantum Electrodynamics (QED). QED describes the electrons and the positrons and the interaction mediated by photons.

The QED theory can be derived by requiring the the global $U(1)$ symmetry of the free particle field described by

$$\mathcal{L}_0 = \overline{\psi}(\gamma^\mu \partial_\mu - m)\psi, \tag{1.1}$$

where the ψ is the quantum field with mass m, and γ^μ are the Dirac matrices.

The $U(1)$ symmetry requires the Lagrangian to be invariant under a local gauge trans-

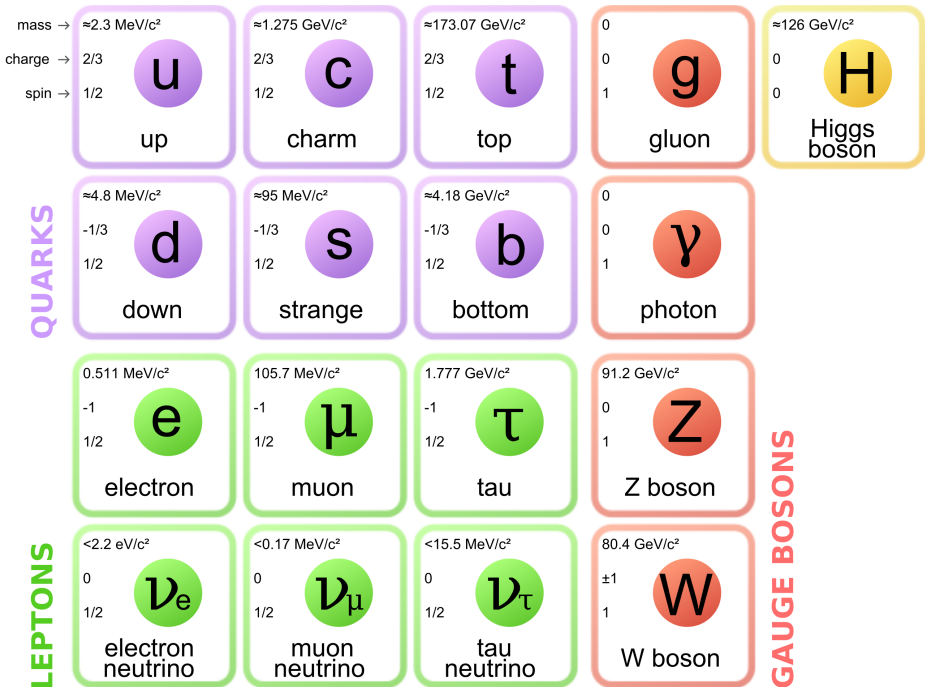

Figure 1.1: Elementary particles and gauge bosons of the Standard Model [1].

formation

$$\psi(x) \rightarrow \psi'(x) = e^{i\alpha(x)}\psi(x), \tag{1.2}$$

in order to maintain the gauge invariance of Eq (1.1). The minimal substitution of the derivative is

$$\partial_\mu \rightarrow D_\mu = \partial_\mu - ieA_\mu, \tag{1.3}$$

where the vector field A_μ follows

$$A_\mu(x) \rightarrow A'_\mu(x) = A_\mu(x) + \frac{1}{e}\partial_\mu\alpha(x), \tag{1.4}$$

under the gauge transformation.

After implementing the gauge transformation and minimal substitution, Eq (1.1) becomes

$$\mathcal{L} = \overline{\psi}(i\gamma^\mu D_\mu - m)\psi = \mathcal{L}_0 + e\overline{\psi}\gamma^\mu\psi A_\mu = \mathcal{L}_0 + \mathcal{L}_{int}. \tag{1.5}$$

The missing kinetic term of A_μ can be fixed by adding

$$\mathcal{L}_A = -\frac{1}{4} F_{\mu\nu} F^{\mu\nu}, \tag{1.6}$$

where

$$F_{\mu\nu} = \partial_\mu A_\nu - \partial_\nu A_\mu. \tag{1.7}$$

Now the A_μ term is the field of photon obeying Maxwell's equation.

Finally, we construct the interaction term $\mathcal{L}_{int}$ that describes the interaction between the fermions and the electromagnetic field, photons, by implementing the local gauge invariance requirement to a free particle field.

The Lagrangian that describes both electromagnetism and weak interactions should be invariant under $SU(2) \times U(1)$ symmetry, instead of the $U(1)$ gauge theory. In this electroweak theory, leptons and quarks are divided into left-handed doublets and right-handed singlets,

$$\begin{pmatrix} \nu_e \\ e \end{pmatrix}_L, \begin{pmatrix} \nu_\mu \\ \mu \end{pmatrix}_L, \begin{pmatrix} \nu_\tau \\ \tau \end{pmatrix}_L, e_R, \mu_R, \tau_R \tag{1.8}$$

$$\begin{pmatrix} u \\ d \end{pmatrix}_L, \begin{pmatrix} c \\ s \end{pmatrix}_L, \begin{pmatrix} t \\ b \end{pmatrix}_L, u_R, d_R, c_R, s_R, t_R, b_R. \tag{1.9}$$

The quantum number weak isospin I_3 and the weak hypercharge Y are used to classify these doublets and singlets. For doublets $I_3 = 1/2$ and $I_3 = 0$ for singlets. Both I_3 and Y are related to the electric charge Q of each particle by the Gell-Mann-Nishijima relation

$$Q = I_3 + \frac{Y}{2}. \tag{1.10}$$

This structure can be incorporated into the quantum field theory by requiring the Lagrangian to be invariant under the group of gauge transformation. The $SU(2) \times U(1)$ group has four generators,

$$T_a = I_a (a = 1, 2, 3) \quad \text{and} \quad T_4 = Y, \tag{1.11}$$

where I_a are the isospin operators, and Y is the hypercharge operator. The algebra relations between these operators are

$$[I_a, I_b] = i\epsilon_{abc} I_c, \quad [I_a, Y] = 0. \tag{1.12}$$

The Lagrangian of electroweak interaction in the SM theory are combined with gauge, Higgs, fermion, and Yukawa interactions,

$$\mathcal{L}_{\mathrm{EW}} = \mathcal{L}_G + \mathcal{L}_H + \mathcal{L}_F + \mathcal{L}_Y. \tag{1.13}$$

In order to give mass to some gauge bosons, $W^{\pm}, Z$, and keep the other gauge boson γ massless, the symmetry of electroweak interaction has to be broken via the Higgs mechanism. This is called spontaneous symmetry breaking.

The Higgs sector and the charge current interactions between $W^{\pm}$ and quarks after symmetry breaking in the electroweak theory are the foundations for the analysis described in this thesis.

1.1.2 Spontaneous Symmetry Breaking and Higgs Boson

In the SM theory, the $SU(2) \times U(1)$ symmetry has to be broken via the Higgs mechanism. First, a single isospin doublet of complex scalar fields with hypercharge Y = 1 is introduced and coupled to the gauge field. The Higgs field is described by

$$\Phi(x) = \begin{pmatrix} \phi^+(x) \\ \phi^0(x) \end{pmatrix}, \tag{1.14}$$

The Higgs field couples to the gauge field via minimal substitution

$$D_\mu = \partial_\mu - ig_2 \frac{\sigma_a}{2} W_\mu^a + i\frac{g_1}{2} B_\mu, \tag{1.15}$$

similar to Eq (1.3). Then, the Higgs Lagrangian is

$$\mathcal{L}_H = (D_\mu \Phi)^\dagger (D^\mu \Phi) - V(\Phi), \tag{1.16}$$

with the Higgs potential

$$V(\Phi) = -\mu^2 \Phi^\dagger \Phi + \frac{\lambda}{4}(\Phi^\dagger \Phi)^2. \tag{1.17}$$

When $\mu^2, \lambda > 0$, this potential has a minimal value for non-vanishing field with $\Phi^\dagger \Phi = 2\mu^2/\lambda$, and the vacuum expectation value is

$$< \Phi >= \frac{1}{\sqrt{2}} \begin{pmatrix} 0 \\ v \end{pmatrix} \quad \text{with} \quad v = \frac{2\mu}{\sqrt{\lambda}}. \tag{1.18}$$

This expectation value $< \Phi >$ is not symmetric under the gauge transformation $SU(2) \times U(1)$, although the Lagrangian started with this symmetry. We say that the symmetry was spontaneously broken here.

By choosing a particular gauge, denoted as the unitary gauge, so that $\phi^+ = \chi = 0$, the Higgs field Eq (1.14) has the simplest form

$$\Phi(x) = \frac{1}{\sqrt{2}} \begin{pmatrix} 0 \\ v + H(x) \end{pmatrix}. \tag{1.19}$$

Also the Higgs potential becomes

$$V = \mu^2 H^2 + \frac{\mu^2}{v} H^3 + \frac{\mu^2}{4v^2} H^4, \tag{1.20}$$

where the Higgs boson mass $m_H = \sqrt{2}\mu$.

1.1.3 The Yukawa Potential and the CKM Matrix

The Yukawa interaction between quarks and the Higgs boson gives the mass to the quarks, and also induces the quark mixing between different quark generations. The Yukawa potential, which describes this interaction, is defined as following

$$\mathcal{L}_Y^{\text{quarks}} = -G_{ij}^d \overline{Q}_L^i \Phi d_R^j - G_{ij}^u \overline{Q}_L^i \Phi^c u_R^j + h.c., \tag{1.21}$$

where G^u, G^d are the Yukawa coupling terms, Φ is the Higgs field, and Q_L^i are the three left handed doublets. Replacing the Higgs field with its vacuum expectation value, the Lagrangian for the Yukawa potential becomes

$$-\frac{v}{\sqrt{2}}G_{ij}^d\overline{d}_L^i d_R^j - \frac{v}{\sqrt{2}}G_{ij}^u\overline{u}_L^i u_R^j + h.c. \tag{1.22}$$

Four matrices, $V_{L,R}^{u,d}$, are introduced to diagonalize the bilinear term in the quark field. This Yukawa potential becomes

$$\frac{v}{\sqrt{2}}V_L^q G_q V_R^{q\dagger}, \tag{1.23}$$

with $q = u, d$. Now this potential term is decoupled for different quark masses.

By introducing these four matrices, the charge current $W^{\pm}$ interaction with the physical quarks contained in Eq (1.13) becomes

$$\frac{-v}{\sqrt{2}}(\overline{u_L}, \overline{c_L}, \overline{t_L})\gamma^\mu W_\mu^+ V_{CKM}\begin{pmatrix} d_L \\ s_L \\ b_L \end{pmatrix} + h.c., \tag{1.24}$$

with $V_{CKM} \equiv V_L^u V_L^{d\dagger}$. This Cabibbo-Kobayashi-Maskawa (CKM) matrix is a 3×3 unitary matrix, and can be written as

$$V_{CKM} = \begin{pmatrix} V_{ud} & V_{us} & V_{ub} \\ V_{cd} & V_{cs} & V_{cb} \\ V_{td} & V_{ts} & V_{tb} \end{pmatrix}. \tag{1.25}$$

1.2 Electroweak "Single" Top Quark Production

The top quark, first discovered at the Tevatron collider in 1995 [7, 8], is the heaviest known elementary particle. The observation of the top quark verified the prediction of the $SU(3) \times SU(2) \times U(1)$ gauge theory. Moreover, the heavy mass provides a unique opportunity to precisely study the strong and electroweak interactions. Unlike other quarks, the short life time of the top quark allows us to study the decay of a free quark,

where the decay products carry the spin and kinematic properties. The top quark is also strongly coupled to the Higgs boson, which will provide some constraints on the Higgs boson search.

In this thesis, we will focus on the electroweak production process of a single top quark. We will first discuss the production channel of top quarks at hadron colliders in Section 1.2.1, then the decay modes of top quarks in Section 1.2.2. Finally, we will review the current search results of electroweak top quark production.

1.2.1 Production

At hadron colliders, the top quark can either be produced in pairs through the strong interaction or singly through the electroweak interaction.

At the Tevatron, the dominant channel of top quark pair production is through quark-antiquark annihilation, about 85% of the total rate, as shown in Figure 1.2. The other mode, production through gluons fusion, is suppressed to 15% of the total rate because of the relatively low center-of-mass energy at the Tevatron compared to the mass of the top quark.

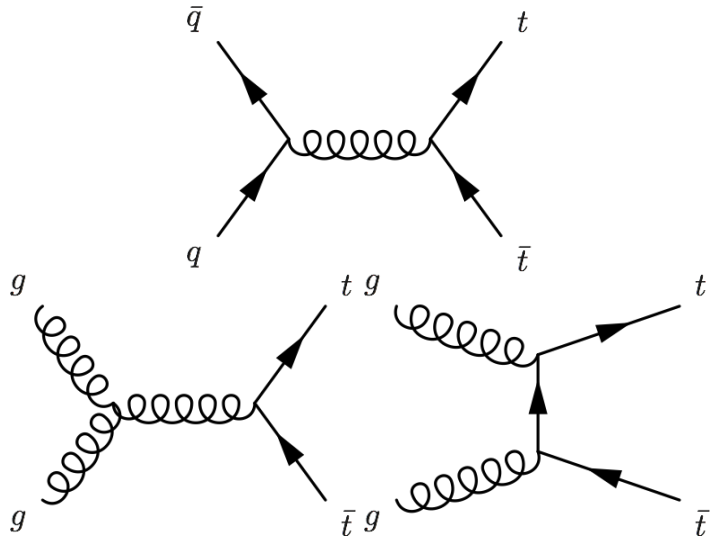

Figure 1.2: Top quark pair production modes.

The top quark can also be produced through electroweak interactions. The production modes are divided into three categories according to the virtuality of the W boson in the

process, as shown in Figure 1.3.

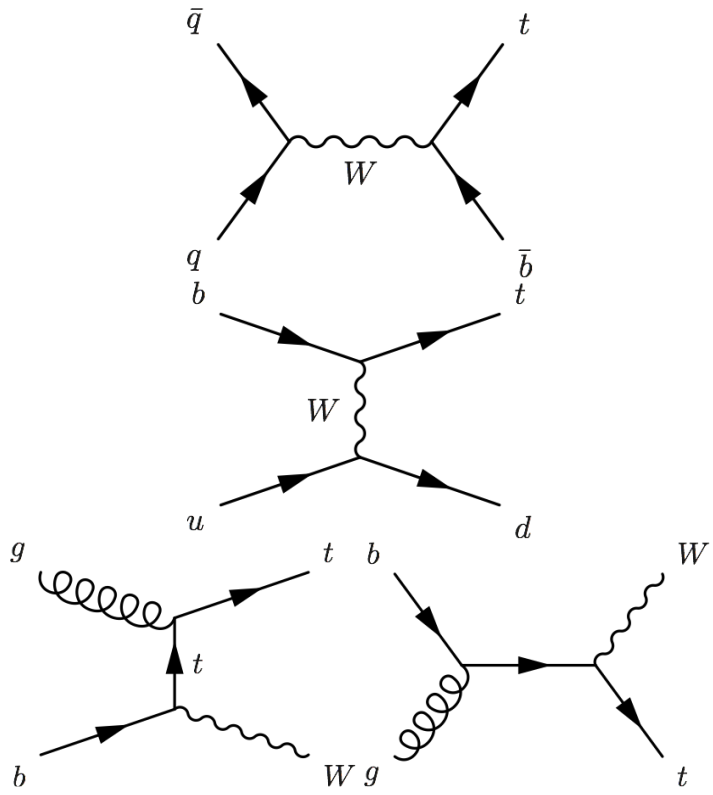

Figure 1.3: Single top quark production modes.

The top process shown in Figure 1.3 is referred to as the s-channel process. In this process, a time-like W boson is produced from quark-antiquark annihilation. Then, this W boson decays into a top quark and an antibottom quark through the Wtb coupling. At the Tevatron, the charge-conjugate process has the same cross section as the process described above. In this thesis, this process and the charge-conjugate process are combined together.

The middle process shown in Figure 1.3 is referred to as the t-channel process. In this process, a bottom quark exchanges a space-like W boson with another quark and transforms into an antitop quark.

The bottom process shown in Figure 1.3 is referred as tW-channel process. In this process, the top quark is produced in association with a W boson. However, since the production rate for this process is too small at the Tevatron, it is ignored in this study.

The cross sections of all production channels calculated up to next-to-next-to-leading-order(NNLO), including pair production and single production, are listed in Table 1.1.

The numbers at both Tevatron and LHC are listed for comparison.

Cross section (pb)	$t\bar{t}$	s-channel	t-channel	tW-channel
Tevatron (1.96 TeV)	7.08	1.05	2.08	0.25
LHC (8 TeV)	234	5.55	87.2	22.2

Table 1.1: Predicted production cross section of single top quark and top quark pair process at the Tevatron and the LHC [4].

1.2.2 Decay

As this study is carried out under the SM framework, the CKM matrix mentioned in the Section 1.1.3 is a 3×3 matrix. The coupling strength of a top quark decaying into a $W^{\pm}$ boson and another quark is regulated by the V_{td}, V_{ts}, and V_{tb} elements in this matrix. Since $V_{tb} \gg V_{td}, V_{ts}$, we assume the banching ratio of a top quark decaying into a W boson and a bottom quark is 100% in all simulations used in our study.

The decay modes of the W boson are listed in Table 1.2. Thus, taking the decay modes of the W boson into account, the final decay products of a top quark will be either $\ell\nu b$ or $q\bar{q}'b$, where $q\bar{q}'$ is the first two generations of quarks.

Decay mode	Branching ratio
$e\nu$	(10.75±0.13)%
$\mu\nu$	(10.57±0.15)%
$\tau\nu$	(11.25±0.20)%
hadrons	(67.60±0.27)%

Table 1.2: Decay modes and branching ratios of W boson [2].

1.2.3 Motivations and Previous Studies

The heavy mass of top quark provides a unique opportunity to test the SM theory and search for physics beyond the SM.

As mentioned in Section 1.1.3, the elements in the CKM matrix are input parameters to the SM. Thus, constraining the value of each element of the CKM matrix is crucial for the SM theory. The $|V_{tb}|$ element, which determines the coupling between the third generation quarks, can be constrained indirectly to $0.999146^{+0.000021}_{-0.000046}$ [2] by requiring the

CKM matrix to be a 3×3 unitary matrix. It is also interesting to measure this parameter directly. Since $|V_{tb}|^2$ is proportional to the single top quark production cross section, the magnitude of this parameter can be constrained directly by measuring the cross section of single top quark production. This measurement is complimentary to the top quark decay branching ratio measurement which can also be used to constrain the $|V_{tb}|$ parameter.

The single top quark production rate is sensitive to physics beyond the SM. Also, different new physics theories would change the cross section of s-channel and t-channel differently. Thus, measuring the cross section of these two process independently would provide a better constraint on new physics theories. For example, the s-channel process is sensitive to new gauge bosons, such as a heavy W' boson, while the t-channel process is sensitive to anomalous Wtb coupling and flavor-changing neutral currents [9].

The Tevatron was shut down in September 2011. The single top quark measurement from the Tevatron is a legacy measurement of the $p\bar{p}$ collider with a center of mass energy of 1.96 TeV. Moreover, as listed in Table 1.1, the cross section for the s-channel process is relatively lower at the LHC compared to other top quark processes. This is because of the valence antiquarks that are available from the antiprotons at the Tevatron but are far less likely in initial states from the proton-proton collisions at the LHC. So, measuring the s-channel cross section is an important measurement and a unique opportunity for the full Tevatron data set.

Because of all the motivations stated above, many studies of single top quark processes have already been conducted. Single top quark production was first observed independently at the Tevatron by the CDF and D0 experiments in 2009 [10, 11]. The t-channel process was first observed in 2011 by the D0 experiment [12]. Later on, this process was also observed by the ATLAS and CMS experiments at the LHC in 2012 [13, 14]. The ATLAS and CMS experiments also found evidence for the tW-channel [15, 16]. Recently, the D0 experiment announced the first evidence for the s-channel process [17]. This thesis documents the legacy s-channel measurement from the CDF experiment [18].

1.3 Higgs Boson

1.3.1 Production and Decay

The Higgs boson coupling to gauge bosons, Higgs bosons, and fermions can be summarized in the following Lagrangian,

$$\mathcal{L} = -g_{Hff}\bar{f}fH + \frac{g_{HHH}}{6}H^3 + \frac{g_{HHHH}}{24}H^4 + \delta_V V_\mu V^\mu (g_{HVV}H + \frac{g_{HHVV}}{2}H^2), \tag{1.26}$$

where

$$g_{Hff} = \frac{m_f}{v}, g_{HVV} = \frac{2m_V^2}{v}, g_{HHVV} = \frac{2m_V^2}{v^2}, \tag{1.27}$$

$$g_{HHH} = \frac{3m_H^2}{v}, g_{HHHH} = \frac{3m_H^2}{v^2}, \tag{1.28}$$

and $V = W^\pm, Z$; $\delta_W = 1$; $\delta_Z = 1/2$. Since the coupling strength of each term is proportional to the particle mass, the dominant processes for Higgs boson production and decay are coupled to W or Z bosons or third generation quarks.

From the Lagrangian, the Higgs boson production cross section at the Tevatron and the LHC for different Higgs mass points are calculated and shown in Figure 1.4. The branching ratio of each Higgs boson decay mode is also calculated for each Higgs boson mass hypothesis, and shown in Figure 1.5.

1.3.2 Status of Higgs Boson Search

Considering the background process of each channel, the most sensitive channel for Higgs boson search at the LHC is the $H \to \gamma\gamma$ and $H \to ZZ \to \ell\ell\ell\ell$. However, both of these channels measure the coupling of the Higgs boson to gauge bosons. Studying the Higgs boson at the Tevatron is still interesting, since the most sensitive channel at the Tevatron is the Higgs boson associated production with vector bosons, in which the Higgs boson decays into two bottom quarks. The study at the Tevatron will provide constraints on the Higgs boson coupling to fermions, which is important to determine whether a Higgs boson is the SM Higgs boson or not.

Moreover, as shown in Figure 1.6, the number of Higgs bosons produced per fb^{-1}

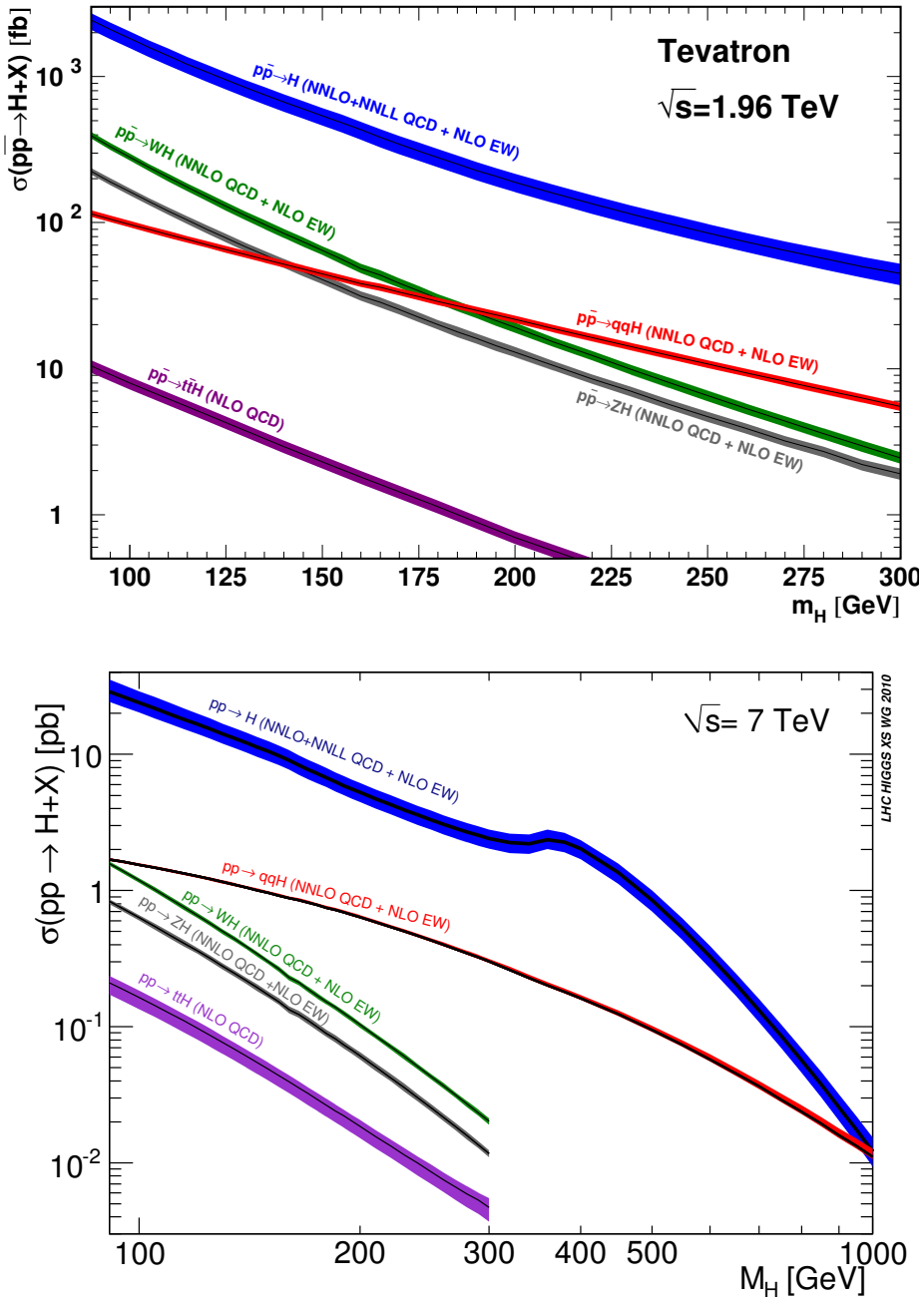

Figure 1.4: Theoretical calculation for the Higgs boson production cross section in different channels at the Tevatron and the LHC [2].

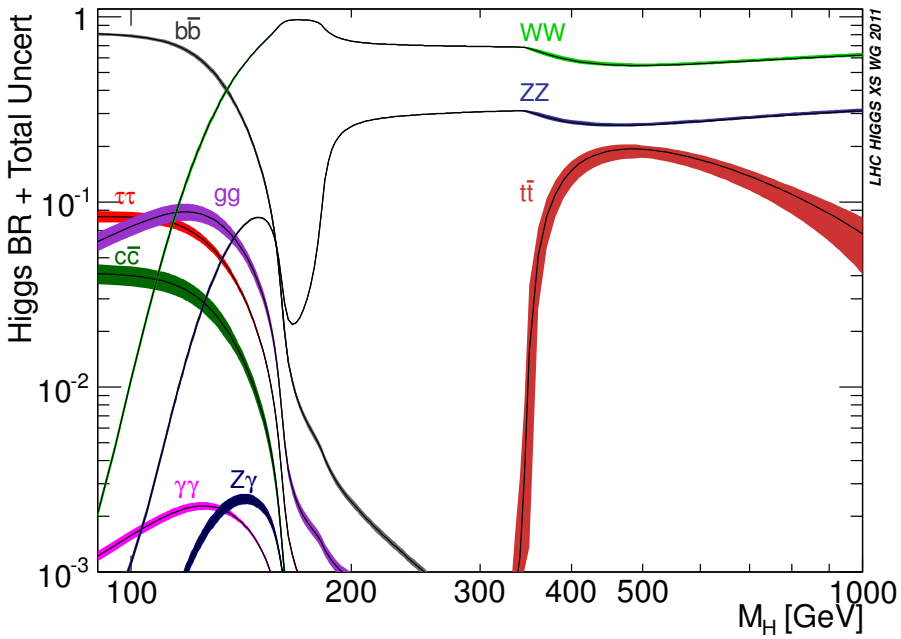

Figure 1.5: Theoretical calculation for the banching ratios of various Higgs boson decay modes for a range of Higgs boson mass hypotheses [2].

is about 50. With the integrated luminosity of 10 fb^{-1}, and combining the CDF and D0 experiments together, there is about 1000 Higgs bosons generated at the Tevatron. Thus, it is practical to study the Higgs boson at the Tevatron.

During my PhD study, both the CMS and ATLAS experiments announced the observation of the SM-like Higgs boson with a mass of 125 GeV/c^2 [19, 20]. Moreover, the Tevatron also claimed evidence of a Higgs boson decaying into two bottom quarks via a combined result of the CDF and D0 experiments that includes this thesis work [21].

As we will see, the most sensitive search channel for the Higgs boson at the Tevatron has a similar signature to that of the electroweak single top quark production. In fact, most of the experimental techniques can be applied to both measurements. In this thesis, we will explain the experimental apparatus used to take the data, the experimental and statistical techniques applied to extract the results, and the important results of this work with impacts for the Higgs sector and evidence for a new process which probes the charge current interactions between the W boson and top and bottom quarks.

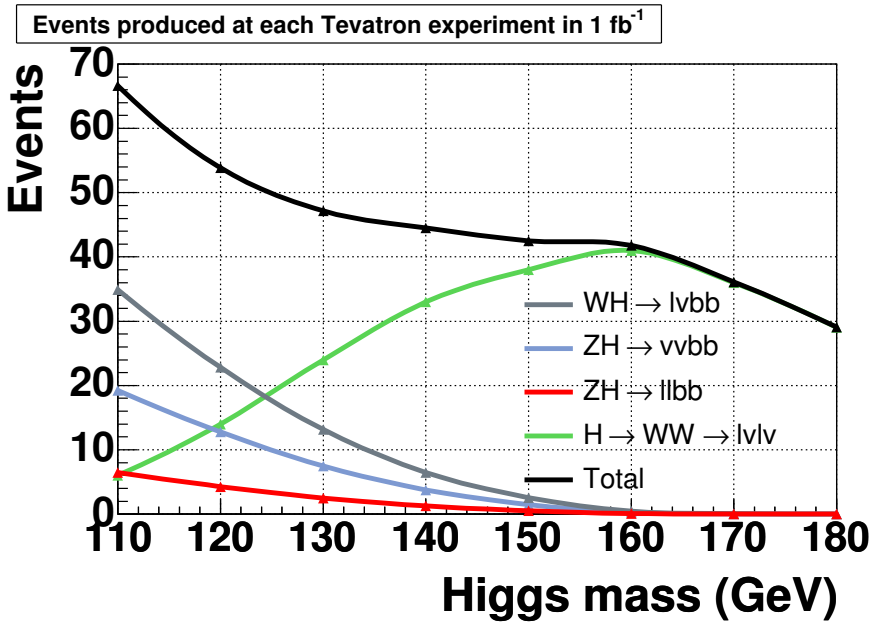

Figure 1.6: Number of Higgs boson events at each experiment at the Tevatron per fb^{-1} as a function of Higgs boson mass.

Chapter 2

Experimental Setup

In order to study the properties of the massive top quark, collision events generated with large center-of-mass energy are required. Also, a general purpose particle detector is necessary to collect all of the particles generated from the collisions. In this study, collision events are generated by the Tevatron collider, and detected by the CDF Run II detector.

In this chapter, we first discuss the accelerator, which generates high-energy protons and antiprotons in Section 2.1. Then, the details of the CDF general-purpose detector are described in Section 2.2. Finally, we introduce the data acquisition system in Section 2.3.

2.1 The Tevatron Collider

The Tevatron is the first accelerator to reach the TeV energy scale. It also was the most powerful collider until 2009 when the LHC surpassed it in energy. A schematic view of the Tevatron accelerator complex is shown in Figure 2.1. With the series of accelerators described below, protons and antiprotons are both accelerated to 0.98 TeV.

2.1.1 Proton Production and Acceleration

The acceleration process for protons starts from the production of H^- ions. Ions are produced in the pre-accelerator (Preacc) and accelerated to 750 keV. After the first acceleration, ions are transferred into Linear Accelerator (Linac), and accelerated to 400 MeV.

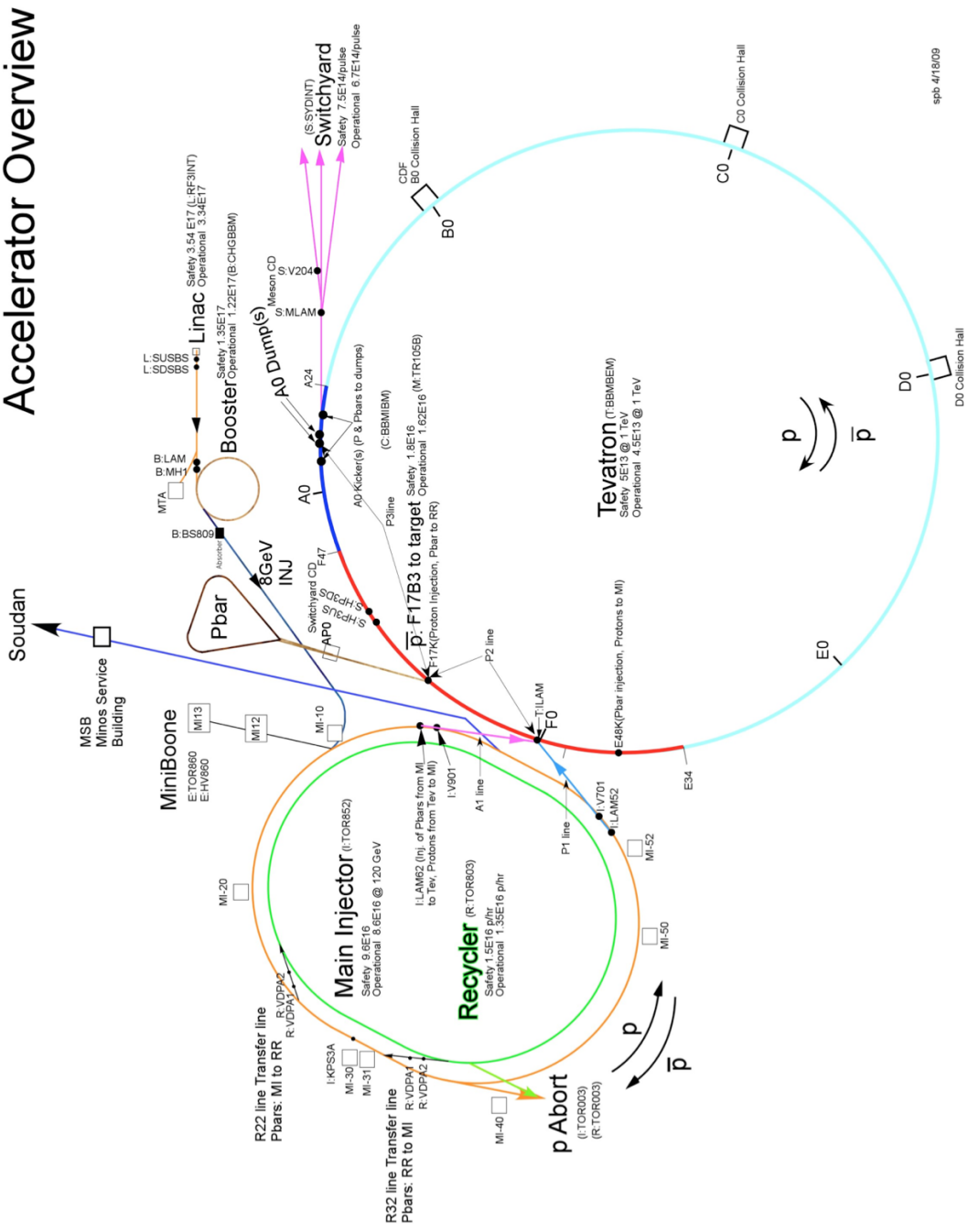

Figure 2.1: The schematic view of Tevatron accelerator complex [3].

The next stage of acceleration is the Booster, which is the first circular accelerator (synchrotron) in the chain of accelerators. The radius of the Booster is 75 meters. The H^- ions are stripped of electrons when they enter the Booster in order to convert the beam into protons. The protons are accelerated to 8 GeV in the booster before entering the next accelerator stage.

The Main Injector follows the Booster and is also a synchrotron but with seven times the circumference. Here, protons are accelerated to different energy depending on their destination. Protons are accelerated to 150 GeV before being injected into the Tevatron collider. For antiproton generation, protons are accelerated to 120 GeV.

2.1.2 Antiproton Production and Acceleration

The antiproton generation starts from the Main Injector. Protons with 120 GeV energy are directed to a target made from nickel alloy and the collision generates many types of secondary particles. The antiprotons with about 8 GeV of energy are collected and transferred to the antiproton source (pbar source) which is based on two synchrotrons.

The purpose of these two synchrotrons is not to increase the energy of the antiprotons, but to bunch and accumulate antiprotons. The Debuncher, the first of the two synchrotrons, is a rounded triangle-shaped accelerator. The main purpose of the Debuncher is to efficiently capture the high momentum spread antiprotons. The Accumulator sits in the same tunnel as the Debuncher. It is the storage ring for antiprotons before they are transferred to the Recycler. The accumulation process often takes many hours before there are enough antiprotons for a new store.

The Recycler is an antiproton storage ring in the Main Injector tunnel. The Recycler was originally designed to recycle the antiprotons from the Tevatron. Instead, the Recycler only accepts the antiprotons from the pbar source and further cools them before they are transferred to the Main Injector. In the Main Injector, antiprotons are accelerated from 8 GeV to 150 GeV, and prepared for injection into the Tevatron collider.

2.1.3 Tevatron Collision

The Tevatron is the final and also the largest accelerator in the chain of accelerators. The circumference of the Tevatron is about 4 miles. The Tevatron can accept both protons and antiprotons and accelerate them from 150 GeV to 980 GeV. In order to be able to run at such high energy, the magnets used in the Tevatron are made of superconducting material and are cooled to 4K when running. Both protons and antiprotons are kept running in the Tevatron for many hours before the accumulation of antiprotons is ready for a new store.

There are two collision points in the Tevatron collider, B0 and D0, where the 1.96 TeV collisions occur. There is one large general-purpose detector at each point, the Collider Detector at Fermilab (CDF) at B0 and the D0 detector at D0.

2.2 The CDF Detector

The Collider Detector at Fermilab (CDF) is a general-purpose particle detector as shown in Figure 2.2. The CDF detector consists of many different detector subsystems designed to measure different properties of different particles. There are three major detector systems: the tracking system, the calorimeter system, and the muon system.

The commonly-used coordinate system at CDF is the spherical system. The z axis is along the beamline, and the direction that the protons travel defines the positive z direction, while the interaction point is defined as $z = 0$. The polar angle θ is defined so that $\theta = 0$ is the $+z$ direction and $\theta = \pi$ is the $-z$ direction. The azimuthal angle φ is defined so that $\varphi = 0$ is the north and $\varphi = \pi$ is the south. The last important variable, pseudorapidity, is defined to be $\eta = -\ln(\tan(\theta/2))$. Pseudorapidity is closely related to the rapidity of a particle, $y = \frac{1}{2}\ln\frac{E+p_z}{E-p_z}$, which is Lorentz invariant. The pseudorapidity is a good approximation of the rapidity when the energy of a particle is much larger than the mass of the particle, which is often the case at the Tevatron.

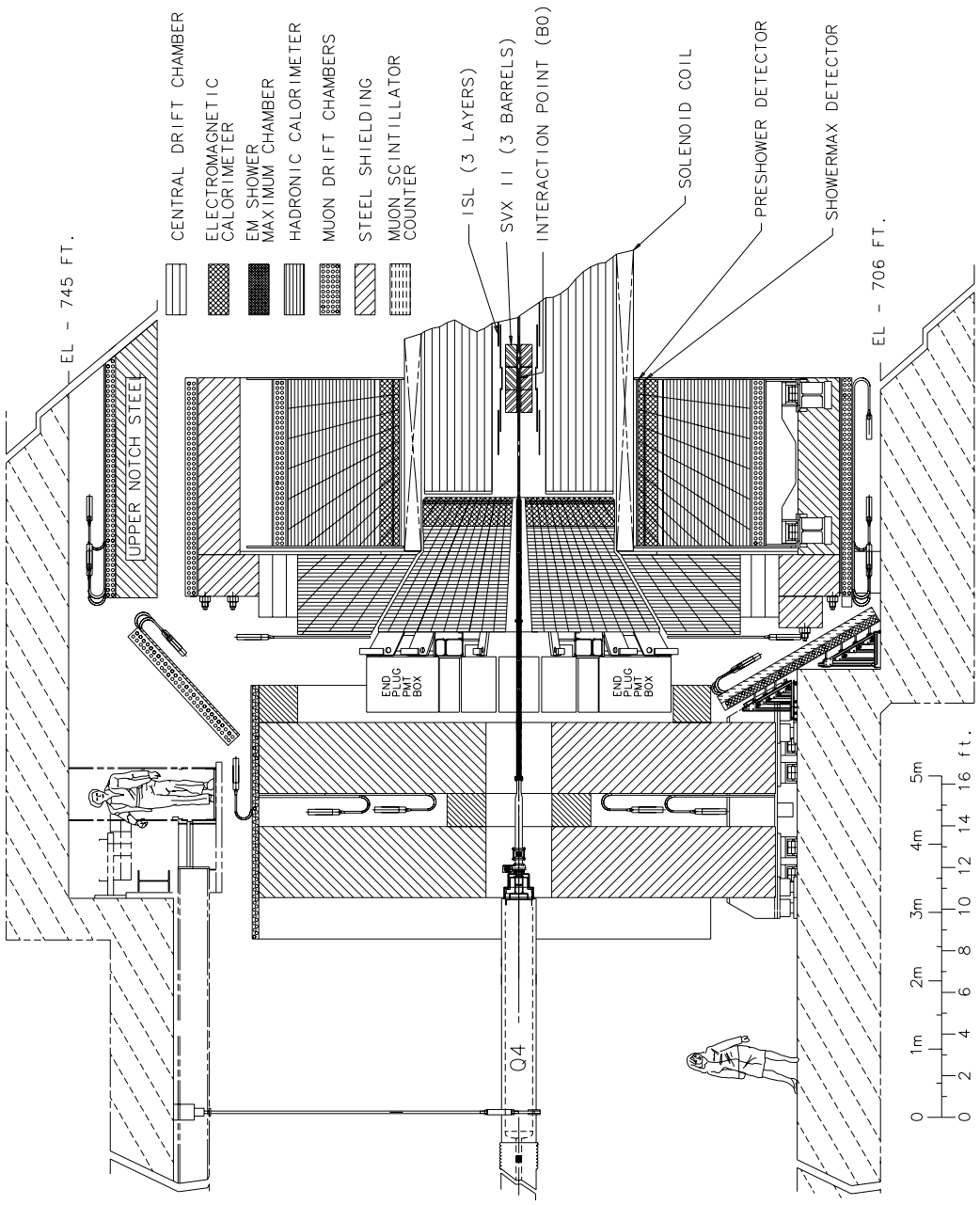

Figure 2.2: The bulkhead view of CDF Run II detector.

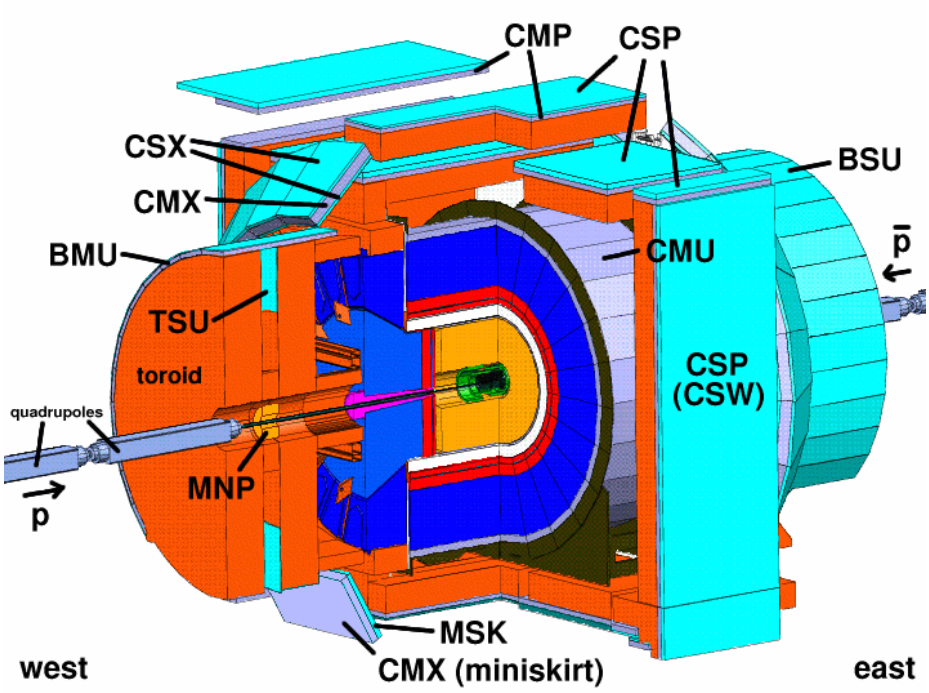

Figure 2.3: The cutaway view of the CDF Run II detector.

2.2.1 Tracking System

The tracking system is used to reconstruct the trajectories of charged particles. It is the innermost system of the CDF detector, and located inside a superconducting solenoid magnet. The solenoid is 4.8-meter long, and its inner radius is 1.5 m. The magnetic field inside the solenoid is 1.4 T, the direction of which is parallel to the beamline. The tracking system at CDF consists of three different parts, from inside to outside: the silicon detectors, the central outer tracker, and the time-of-flight detector.

The tracking system can measure the momentum of the charged particles from the curvature of charged tracks in the magnetic field. Precise resolution of momentum and impact parameter is achieved by using the silicon detectors that are located very close to the interaction point. The resolution of the silicon tracking system is crucial in reconstructing the secondary vertex, which is an important property for identifying the decays of B hadrons.

Silicon Detectors

The silicon detector is built with p-type silicon doped with thin strips of n-type silicon. A reverse bias voltage is applied on the p-n junction. When a charged particle hit the strip, electron-hole pairs will be created. Under the high voltage, electrons will be collected at one end, holes at the other. With information from axial strips and stereo strips, the hit position can be determined. Silicon detectors are precise, but as a downside, they are also expensive and sensitive to radiation damage.

The silicon detectors are the most precise detectors at CDF [22]. At CDF Run II, the silicon detectors consist of three subsystems and cover a radius from 1.5 cm to 28 cm from the beam line. The layers of the silicon detectors are shown in Figure 2.4. All three silicon detectors combined have a resolution of 40 µm of impact parameter and 70 µm in z direction.

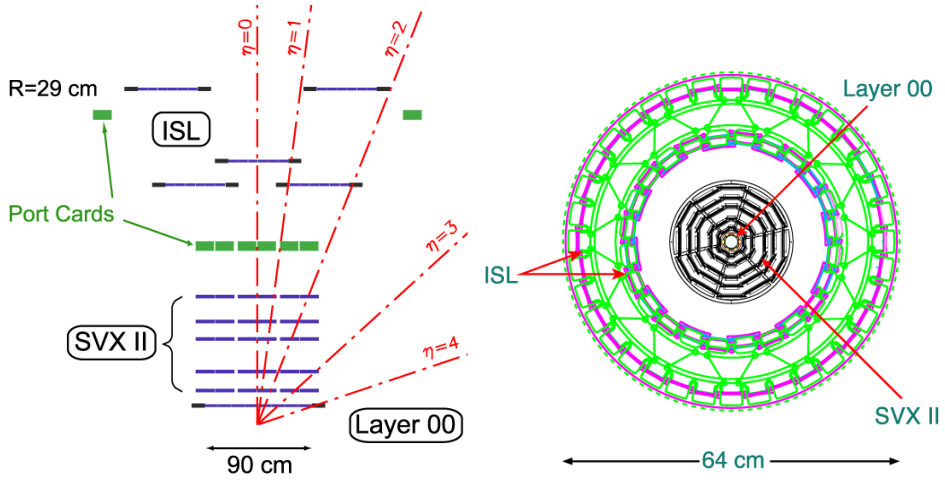

Figure 2.4: The side view and front view of silicon detectors at CDF.

The inner most silicon detector is L00, which is only one layer and is a single-sided silicon detector [22]. L00 adopts the design of the LHC to handle an extreme radiation environment. It is named L00 because it is inside the layer 0 of SVX II detector. It was proposed during the construction of SVX II to improve the resolution of secondary vertices. The L00 detector is about 94 cm long and covers η less than 4.0.

The Silicon Vertex Detector (SVX) [23] consists of 5 layers, from layer 0 to layer 4, extending from $r = 2.1$ cm to $r = 17.3$ cm, covering $|\eta| < 2.0$. All layers are double sided.

Strips are aligned axially on one side, with 90-degree stereo strips on the other side for layer 0, 1, and 3. For layer 2 and 4, stereo strips are aligned with 1.2 degree with respect to the axial strips.

The Intermediate Silicon Layer (ISL) [24] is located between the SVX II and COT detector. It contains a single layer silicon detector for $|\eta| < 1$ at $r = 22$ cm and double layer detector when $1 < |\eta| < 2$ at $r = 20$ cm and $r = 28$ cm. Its purpose is to provide enhanced tacking ability in the central region, and to increase the tracking capability in the forward region where the drift chamber only has full coverage up to $|\eta| < 1.0$.

Central Outer Tracker (COT)

The COT is an open cell drift chamber [25] with eight super layers, from layer 1 to layer 8, shown in Figure 2.5. This detector uses a mixture of argon-ethane gas. When a charged particle passes through the chamber, the gas will be ionized. Electrons and ions created from ionization will be collected by wires to reconstruct tracks. The COT detector extends from $r = 40$ cm to $r = 138$ cm, and covers $|\eta| < 1.0$. Wires in super layer 2, 4, 6, and 8 are aligned along the beam line, while other layers are at small stereo angle (2 degrees) with respect to beam line. This kind of structure will provide track information on $\phi - z$ direction respectively.

Time of Flight Detector (TOF)

Timing information of a particle reaching a certain position of the detector can be used to discriminate particles, such as K and π. Although this information is not used directly in this analysis, it is used to remove background cosmic ray events.

The TOF detector at CDF is made of a ring of scintillators [26]. Charged particles generate photons when passing through the scintillators which are collected by photo-multiplier tubes (PMT). The TOF measures the time difference between the collision and the the arrival of particles.

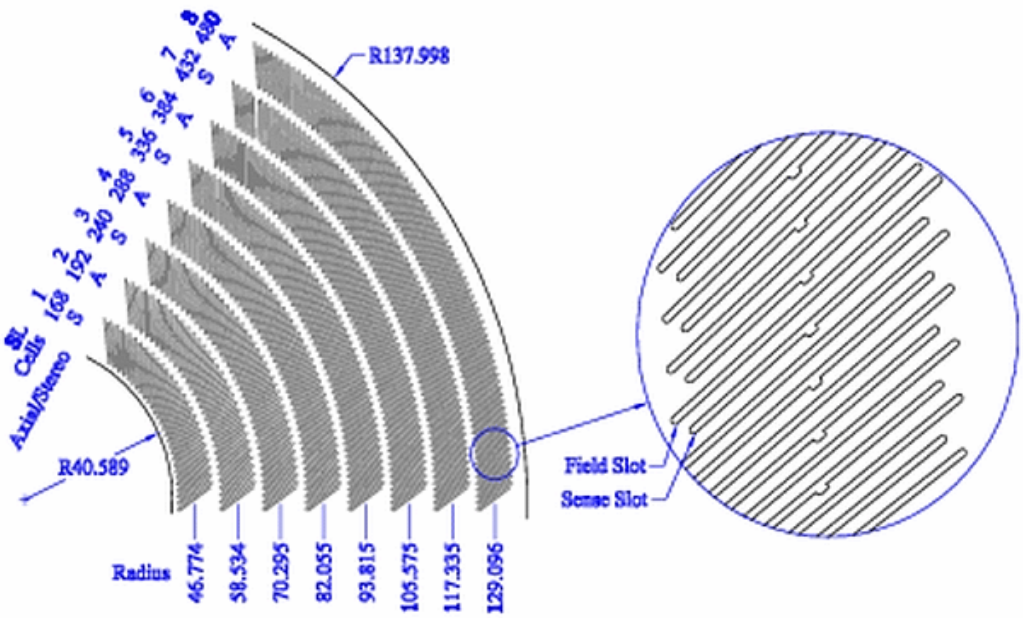

Figure 2.5: The structure of the COT detector.

2.2.2 Calorimeter System

In addition to the tracking information and the measured momentum of each particle, the energy also must be determined. At CDF, the energy of particles is measured by the calorimeter system. The calorimeter system uses scintillator to sample the energy of incident particles. The excited photons are collected using wavelength shifting fibers, and eventually measured by photon multiplier tubes (PMT).

When a high-energy particle passes through a material, it generates a set of less-energetic secondary particles through inelastic scattering with nuclei of the material or pair production, creating a shower of particles. These secondary particles will create more particles. Thus, the number of particles will increase. As more and more generations of secondary particles are created, the energy of these particles are decreasing through inelastic scattering and ionization and finally will be absorbed by material. The total number of particles will eventually decrease. Measuring the profile of the whole shower versus depth provides a better estimation of the particle energy.

In order to reduce the amount of scintillator material required, CDF placed absorber material between each layer of scintillators to reduce the depth of the shower generated

from incident particles. This type of calorimeter is called a sampling calorimeter. The energy resolution is sacrificed by reducing the size of the calorimeter.

The calorimeter system at CDF is generally divided into an electromagnetic (EM) calorimeter and a hadronic calorimeter. This split is natural since electrons and photons interact with materials through the electroweak interaction, while mesons and hadrons interact through the strong interaction. The energy resolution of the hadronic calorimeter is worse than the EM calorimeter since unlike the EM one, there is about 30% of the hadronic energy that cannot be measured by the hadronic calorimeter.

Calorimeters can be divided into two main categories: central calorimeters and plug calorimeters, according to the $|\eta|$ coverage of the detector.

The central calorimeters cover the $|\eta| < 1.1$, the EM calorimeter is immediately outside the solenoid and surrounded by the hadronic calorimeters. All the layers are parallel to the beam line.

Central Electromagnetic Calorimeter (CEM) [27] This calorimeter consists of 31 alternating layers of lead and scintillator. It is segmented into 24 towers in ϕ direction and 10 towers in η in order to be able to match to a track.

Central Electromagnetic Shower Maximum Detector (CES) [27] This detector is located at the depth where the shower is at maximum. This detector is made of strip and wire chambers so that it can measure the position information to a much better precision than CEM. This information is important for particle identification.

Central Hadronic Calorimeter (CHA) [28] The hadronic calorimeter is composed of 32 alternating layers of iron and scintillator. It has the same number of segments in the ϕ direction as the CEM, but only 8 segments in η. Thus, it only covers up to $|\eta| < 0.9$.

Wall Hadronic Calorimeter (WHA) [28] Because the CHA has the same length as the CEM, and is located outside of the CEM, the *eta* coverage of CHA is smaller than CEM. In order to improve the coverage, the WHA is added to fill the gap, which covers $0.8 < |\eta| < 1.2$. The WHA is made of 15 layers of alternating iron and

scintillator. The layers are perpendicular to the beam line and are segmented into six towers in η.

The plug calorimeters cover the range of $1.1 < |\eta| < 3.6$ with all the calorimeter layers are perpendicular to the beam line.

Plug Electromagnetic Calorimeter (PEM) [29] This calorimeter comes with 23 layer of alternating lead and scintillator. It is segmented into 12 towers in η.

Plug Electromagnetic Shower Maximum Detector (PES) [30] PES is composed of scintillator strips. Based on the same idea as the CES, the PES is designed to measure accurate positioning information of a shower.

Plug Hadronic Calorimeter (PHA) [31] This hadronic calorimeter is composed of 23 layers of alternating iron and scintillator. It covers the range of $1.2 < |\eta| < 3.6$, and it has basically the same segmentation as PEM, except it has one fewer tower in η.

2.2.3 Muon System

Since muons are massive and do not interact with materials through the strong interaction, they only leave minimum ionizing energy in the calorimeters. They must be measured separately.

At CDF, muon detectors are mounted outside the calorimeter detectors. They are made of single-wire drift chambers. In each muon detector, there are four layers of chambers. A muon stub in the detector requires that three out of four layers are fired. In order to reject cosmic ray muons, there are also scintillators paired with each muon detector to provide timing information in muon identification. The muon stub also needs to be matched to one track in the track detector. The energy of the muon will be calculated from the well-measured muon mass and the momentum measured from the track.

The muons detectors used at the CDF experiment are list below

Central Muon Detector (CMU) [32] This muon detector is built just outside the CHA. It covers the region of $|\eta| < 0.6$.

Central Muon Upgrade (CMP) [33] The drawback of the CMU is that it does not have shielding. The CMP is designed to address this problem. It uses the return yoke of the solenoid as the shielding. Thus this detector is built with a box geometry.

Central Muon Extension (CMX) [34] This detector covers $0.6 < |\eta| < 1.0$. This detector consists of three separate parts: the arches, the keystone, and the miniskirt, which together provide a full angular coverage.

Barrel Muon Detector (BMU) [34] The BMU extends the muon coverage in η from 1.0 to 1.5. This detector is attached to the shielding steel which is at the ends of the detector.

2.3 Data Acquisition System (DAQ)

Proton bunches and antiproton bunches at the Tevatron are divided into 3 trains, with 12 bunches in each train. The abort gap between each train is 4.3 μs. At the Tevatron, the collision happens every 396 ns, and the collision rate is 1.7 MHz. Each time a collision happens, the DAQ system sends a signal to the CDF detector to take a measurement. However, it is impossible and unnecessary for the DAQ system to record all of the collision events. Only those events that are interesting to physicists need to be recorded. Online selection systems, usually known as triggers, are implemented in the DAQ system to select interesting events.

The trigger system at CDF is divided into three levels, as shown in Figure 2.6. At each level, a fraction of events will be rejected, and finally, the event rate will be reduced to around 100 Hz.

2.3.1 Level 1 Trigger

The lowest level trigger needs to reduce the event rate from around 1.7 MHz to about 40 kHz. Because of the time requirement, the level 1 trigger needs to make a decision in 5.5 μs. All of the level 1 trigger requirements are built into the hardware. Tracks are reconstructed by the Extremely Fast Tracker (XFT) [35], which uses a dedicated processor, and

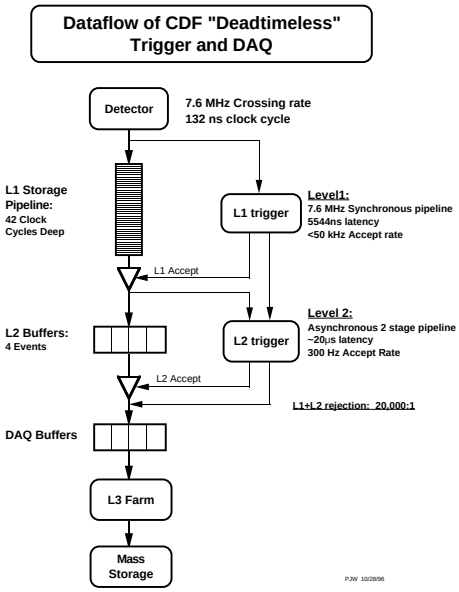

Figure 2.6: The functional diagram for the DAQ system of the CDF detector.

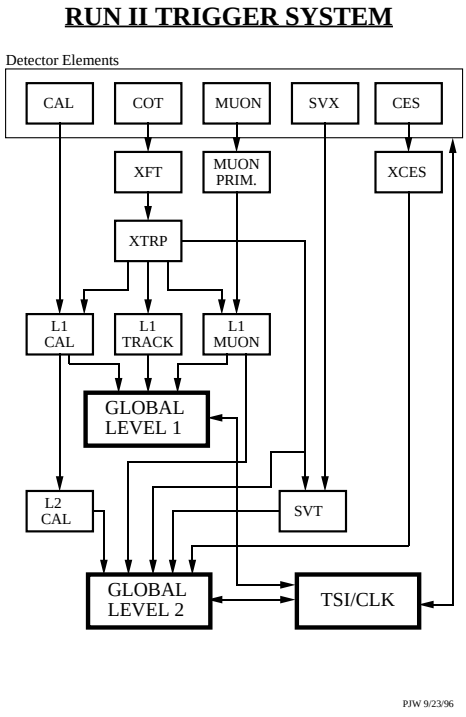

Figure 2.7: The block diagram for the trigger system of the CDF detector.

can match reconstructed tracks to electromagnetic-calorimeter clusters or muon stubs to find electrons or muons. Figure 2.7 shows the level 1 trigger and the limited information from tracks, energy measured in calorimeters, and muons used to make decisions.

2.3.2 Level 2 Trigger

With lower incoming event rate, the level 2 trigger is running in asynchronous mode in order to process information obtained from silicon detectors. The level 2 trigger is required to finish processing within 20 µs.

The track information from the silicon detector is analyzed by the Silicon Vertex Tracker (SVT) [36]. The main improvement of including silicon detector information is that the events now can be triggered by a secondary vertex, which can be used to select the hadronic decay of a b quark. Also, with a much more precise measurement of tracks by the silicon detectors, the resolution of the momentum of tracks is better than the calculation by the level 1 trigger. The angular matching between tracks and muon stubs is also improved.

The level 2 accept signal initiates a full detector readout for the triggered event.

2.3.3 Level 3 Trigger

At level 3, the information from all subdetectors of events that passed that level 2 trigger is assembled and analyzed to make the final decision. Events are reconstructed by Event Builder (EVB), which is a simplified version of the offline reconstruction code. Events which pass the level 3 trigger are ready to be recorded on the disk.

Since some triggers are fired at very high rate, one method called prescaling is implemented. This method is designed to bring down the event rate by only recording a fraction of triggered events. For example, a prescale of 10 means only 1 out of 10 triggered events is recorded to disk. Moreover, since the collision luminosity is higher at the beginning of each run, dynamical prescale is also introduced. This will change the prescale number depending on the instantaneous luminosity.

Finally, events are recorded to the disk by Consumer Server/Logger (CSL). CSL cat-

egorizes all the events into different trigger streams based on which triggers were fired. This program will also pick some events for online data-quality monitoring.

2.4 Monte Carlo Simulation

In order to do a complicated analysis on a particle detector, an accurate simulation of all physics processes involved is necessary. At CDF, a Monte Carlo (MC) method is adopted, which randomly generates simulated events of different physics processes. The steps of the simulation process are: generate initial particles according to the parton distribution function, generate final state particles at parton level, shower and hadronize all partons in the event, and finally simulate the detector response to all the hadronized particles.

2.4.1 Parton Distribution Function (PDF)

All physics processes involved in this analysis starts from two quarks or gluons. There are no free quarks or gluons in nature. In the collision process happened at the Tevatron, and all quarks and gluons are confined in either protons or antiprotons. Quarks or gluons involved in the collision come from the valence quarks or the virtual particle seas of the protons, and it is impossible to measure on event-by-event basis the initial properties of these partons. (Partons include quarks and gluons.) Parton distribution functions (PDFs) are employed to overcome this problem. PDFs predicts the probability density as a function of momentum transfer Q^2 between all kinds of partons in the interaction. This analysis uses leading order CTEQ5L [37] PDFs.

2.4.2 Event Generator

Once the two partons are extracted from the PDFs, a hard scattering is calculated for the desired process. The matrix element for the scattering is based on leading-order diagrams or next-to-leading-order diagrams (An NLO PDF is employed for the NLO generator). The software used is called an event generator. In this analysis, different event generators are used for different physics processes. ALPGEN [38] for W+jets and Z+jets; PYTHIA [39]

for WW, WZ, ZZ, $t\bar{t}$, and Higgs; and POWHEG [39] for single top quark processes. The radiated photons, gluons, or leptons are taken care of by the parton showering algorithm.

2.4.3 Parton Showering and Hadronization

All events are passed to PYTHIA for parton showering, which takes care of gluons from initial state radiation and final state radiation. Parton showering also includes the decaying of gluons from the matrix element calculation and from beam remnants or multiple interactions.

Gluons and quarks produced in parton showering also need to be hadronized, to create bayrons or mesons in which the total colorness of the confined quarks is neutral. The hadrons created from hadronization are usually unstable, and will decay into secondary particles before being detected. In PYTHIA, this process is calculated according to the branching fraction measured for each hadron from experiment. This step generates jets of hadrons originating from quarks or gluons in the detector.

2.4.4 Detector Simulation

Once all the relatively long lived particles are generated, it is important to simulate the detector response to all these particles. At CDF, GEANT [40] is employed to simulate the tracking system and the muon detector. In order to save computing time, GFLASH [41], a parametric simulator tuned to the test beam data is used to simulate the response from the calorimeter.

Chapter 3

Event Reconstruction

Once the raw data has been recorded, either from real collisions or Monte Carlo simulation, physics objects need to be reconstructed from this information. This reconstruction process is divided into two steps: high-level detector objects, and particles. High-level detector objects are tracks, reconstructed from hits in the tracking system, and calorimeter clusters, reconstructed using information from both hadron and electromagnetic calorimeters. Then, these objects are identified as particles or physics objects, such as electrons, muons, jets, and neutrinos. All of which will be used in the analysis.

3.1 High Level Detector Objects

High-level-object reconstruction is the intermediate step of particle reconstruction. The tracks identified in this step provide important input information for identifying electrons and muons, and for calculating the energy and momentum of those particles.

3.1.1 Tracking

A precise and efficient track-identification algorithm is essential for lepton and jet reconstruction. Several tracking algorithms are employed to reconstruct tracks in different $|\eta|$ regions of the CDF detector [42].

Outside-In Algorithm

This is the most reliable track reconstruction algorithm. It starts from the COT detector. In the COT detector, track segments are first reconstructed in each superlayer, then combined to form a track. The superlayers of the COT detector are divided into axial and stereo layers. Track reconstruction starts from the outermost axial superlayer and looks for the segments in other axial superlayers which give the best fit. After all axial superlayers are searched, information from the stereo superlayers is included to perform the same fitting again to fully reconstruct the track in three dimensions.

In order to identify a vertex that is located away from the beam line, which is crucial for bottom-quark jet (b jet) identification, tracking information from the silicon detector must also be included. In this algorithm, tracks reconstructed in the COT detector are propagated into the silicon detector. If a hit is found to be aligned with an existing track within the uncertainties, then the hit will be added to the track. By adding the additional hits from the silicon detector, the track resolution is improved.

The impact parameter resolution after combining hits from both detectors is found to be approximately 20 µm. The $|\eta|$ coverage of reconstructed tracks using this algorithm is limited to $|\eta| < 1.0$ by the COT detector.

Silicon-Stand-Alone Algorithm

In order to cover a larger region in η, an algorithm that only uses the silicon detector is also employed. This algorithm can reconstruct tracks with $|\eta| < 2.0$, and also provides limited capability up to $|\eta| < 2.8$. Similar to the outside-in algorithm, this one starts from the axial strips, then adds stereo strips to reconstruct the tracks in three dimensions. The resolution of momentum and impact parameter of this algorithm is not as good as the outside-in one, so tracks reconstructed with this algorithm are not used to look for a secondary vertex.

Inside-Out Algorithm

For tracks with $1.0 < |\eta| < 1.8$, covered by the inner cylinder of the COT detector, the resolution of track momentum and impact parameter from the silicon-stand-alone algorithm can be improved by adding hits in the COT detector to the reconstruction process. The reconstructed tracks in the silicon detector are used as seeds to look for hits in the COT detector. After all superlayers of the COT detector are searched, the track will be fit again with the COT hits included.

PHOENIX Algorithm

Information from other subdetectors, other than tracking system, could also be used as seeds to reconstruct tracks. The PHOENIX algorithm starts from clusters (see Section 3.2.1 for clustering details) in the plug calorimeter and the primary vertex. It uses the cluster and the primary vertex (see Section 3.1.2 for primary vertex definition) as the two ends of a track, and estimates the momentum of the track, from the energy of the cluster. Based on this *a priori* information, this algorithm looks for hits in the tracking system.

In this analysis, we include tracks from the outside-in, silicon-stand-alone, and inside-out algorithms. The PHOENIX tracks are only used to reconstruct electrons in the forward region.

3.1.2 Primary Vertex

The point where the collision between the proton and the antiproton occurs is referred to as the primary vertex of the event. Since the bunch length is about 28 cm at the Tevatron, the collision point could change dramatically from event to event. Thus, accurately measuring the location of the primary vertex is crucial to the correction of the measured transverse energy. Also, accurate reconstruction of the primary vertex will make the secondary vertex measurement possible.

Reconstructing the primary vertex starts by fitting for the vertex position with the thirty most energetic tracks. With the fitted value, all the tracks that satisfy the $\chi^2 < 10$ cut will be kept. Then a new fit with the remaining tracks will be performed. Iteration

of the χ^2 cut and the fitting process is repeated until all remaining tracks pass the χ^2 requirements. The position from the final fit result is taken as the position of the primary vertex.

3.2 Physics Object Identification

With the reconstructed tracks, now it is possible to reconstruct physics objects. In the analyses discussed in this thesis, leptons, jets, and missing transverse energy are required. In the following sections, reconstruction of these objects is discussed. However, further requirements, besides those discussed in this chapter, are necessary in order to remove fake reconstructed objects and this additional selection will be described in the next chapter.

3.2.1 Lepton Identification

The leptons discussed in this thesis only include electrons and muons[1]. At CDF, we identify two tight electron categories and two tight muon categories. In order to improve the muon coverage, six more loose muon categories are included. We also included isolated tracks as a supplemental muon reconstruction algorithm. The coverage for two electron categories are shown in Figure 3.1, and the coverage for muon categories are shown in Figure 3.2.

Electron Identification

An identified electron consists of a well-reconstructed isolated track in the tracking subdetector and a cluster in the EM calorimeter matched with the track. The tracking information is used to remove photons which also generate similar showers in the EM calorimeter.

The cluster in the EM calorimeter is reconstructed using the following algorithm. All towers in the EM calorimeter are listed in decreasing order of energy deposited in the tower. There are two lists of calorimeter tower energies: the usable list ($>$ 100 MeV) and the seed list ($>$2 GeV). The algorithm starts from the most energetic tower in the seed

[1]The leptonically decayed τs are also included by identifying the decay products, electrons or muons.

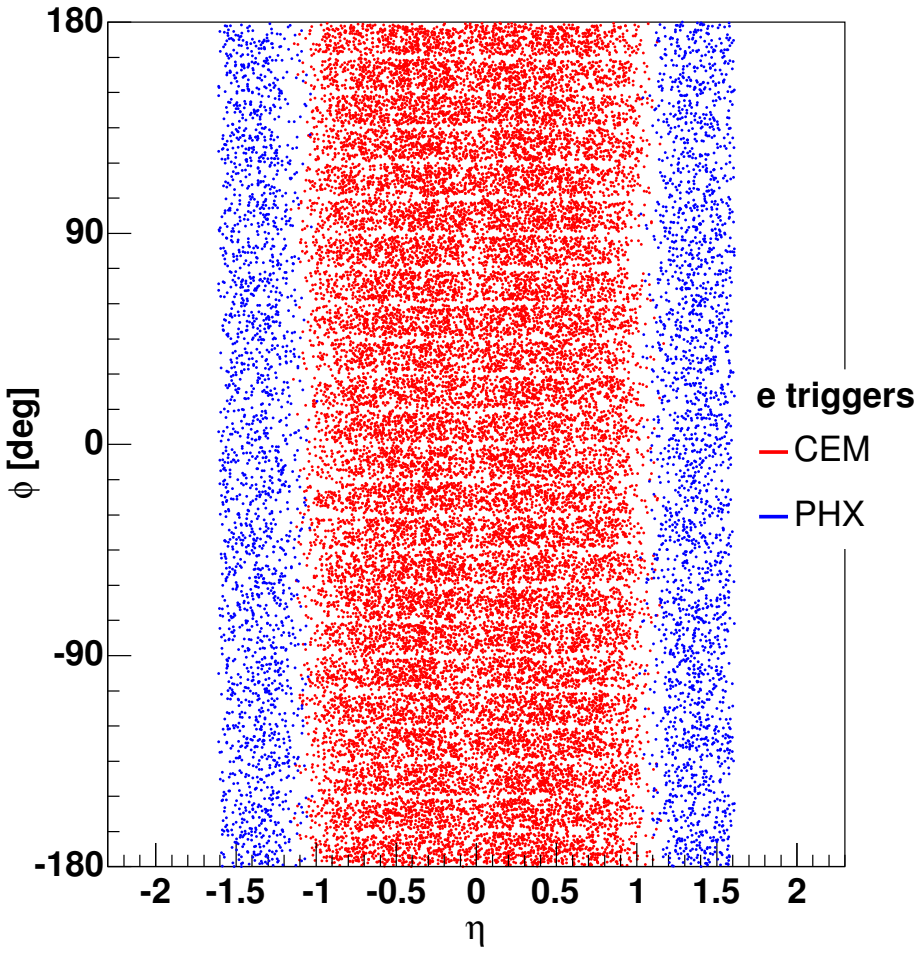

Figure 3.1: The distribution of electron categories in the $\eta - \phi$ plane.

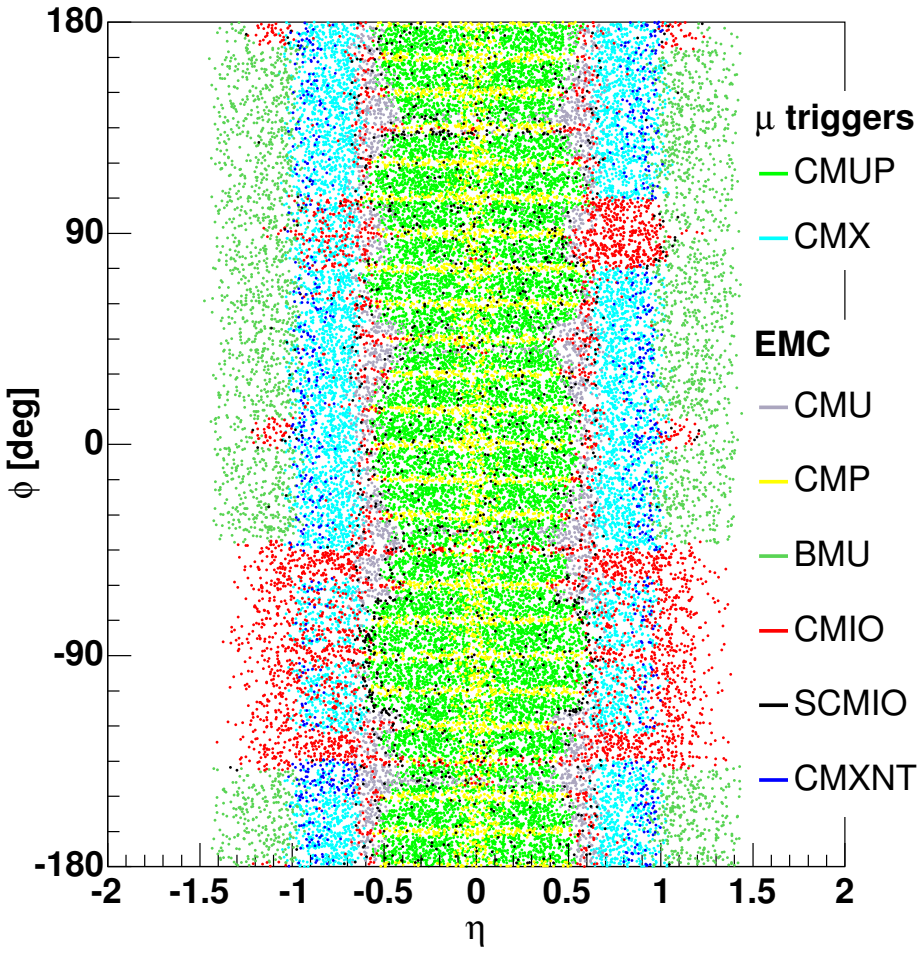

Figure 3.2: The distribution of muon categories in the $\eta - \phi$ plane.

list and then adjacent towers in the usable list are added to form a 2×2 (for the forward region) or 3×3 tower region (for the CEM detector). An EM cluster is found if

$$E_{HAD}/E_{EM} < 0.125, \tag{3.1}$$

where E_{HAD} is the energy deposited in the hadron calorimeter in the region, and E_{EM} is the energy in the EM calorimeter. The used towers are removed from the list, and the next seed tower in the list is selected to repeat the algorithm until all of the towers in the seed list are used.

For a reconstructed cluster, the energy is then corrected by the position in the tower, the online calibration, and the response of the calorimeter measured by test beam. Energy information from other detectors are also used, such as the pre-shower detector and the shower maximum detector. The profile of the cluster measured in the shower maximum detector is also used to distinguish an electron from a photon, and improve the position measurement of the cluster.

The isolation requirement is also applied to reconstruct a tight electron. The isolation is defined to be the ratio of the transverse energy that is not from the cluster, but is deposited within the 0.4 cone in the $\eta - \phi$ plane of the cluster, to the transverse energy of the cluster. The isolation for a tight electron is required to be less than 0.1. This means that there is little activity around the electron, so the reconstructed electron is less likely to be a jet misidentified as an electron.

There are two types of a successfully reconstructed electron, CEM and PHX, depending on the detector where the cluster is reconstructed. Further requirements are applied for a reconstructed electron and the full list is given in Table 3.1.

Muon Identification

Since a muon is much heavier than an electron, the radiative effect of the muon interacting with matters is not present in the energy range in this analysis. Thus, it is a minimum ionizing particle (MIP), which leaves a minimum amount of energy when it passes through materials. At CDF, muons only deposit a limited amount of energy in

Lepton	Variable	Reconstruction requirement
Both	Geometry	fiducial
	E_T	> 20 GeV
	χ^2_{strip}	< 10
	Isolation	< 0.1
CEM	Track	Pass the quality requirement
	Photon conversion	Pass the conversion requirement
	E_{HAD}/E_{EM}	$< 0.055 + 0.00045E$
	E/p	< 2.0, if $E_T < 100$ GeV
	$Q \times \Delta x$	>-1.5 cm and < 3.0 cm
	$\lvert\Delta z\rvert$	< 3.0 cm
	$Lshr$	< 0.2
PHX	E_{HAD}/E_{EM}	< 0.05
	E_5/E_9	> 0.65
	$\Delta R_{\text{PEM}-\text{PES}}$	< 3 cm
	$N_{silicon}$	> 3

Table 3.1: The identification requirements for a tight electron [5].

both the EM and hadron calorimeters and high-energy muons usually pass through the calorimeters. Therefore, the CDF muon system consists of several different muon chambers located outside of the calorimeters to identify a muon.

A registered particle in a muon chamber is referred to as a "stub", and reconstructed muons are named according to the muon chamber in which they were detected. A reconstructed muon is a high-quality track which points to a stub in the muon detector, and has only minimal energy observed in the calorimeters along the path connecting the track and stub.

Since the acceptance rate for a tight muon is limit by the coverage of the muon chambers, a set of loose muons is defined to increase the muon coverage.

For a reconstructed muon, the detailed identification requirements are listed in the Table 3.2.

Isolated Track

Isolated tracks are the last category of leptons used in this analysis. An isolated track is defined to be a high-quality track, but is isolated from other tracks. Isolated tracks are not required to be matched to a cluster in the EM calorimeters or a stub in the muon chambers. Similar to the isolation definition in calorimeters, isolation of tracks are calculated

Lepton	Variable	Reconstruction requirement
General	p_T	> 20 GeV/c
	E_{EM}	2.0 + max(0, 0.0115(p-100)) GeV
	E_{HAD}	6.0 + max(0, 0.028(p-100)) GeV
	d_0	< 0.2 or < 0.02, if with silicon hits
	χ^2_{track}	< 2.3
	Track	Pass the quality requirement
	Isolation	< 0.1
CMUP	Fiducial requirement	CMU, CMP
	$\Delta x_{CMU}(trk, stub)$	< 7 cm
	$\Delta x_{CMP}(trk, stub)$	< 5 cm
CMX	Fiducial requirement	CMX
	ρ_{COT}	< 140 cm
	$\Delta x_{CMX}(trk, stub)$	< 6 cm
BMU	Fiducial requirement	BMU
	COT Hits Frac	> 0.6
	$\Delta x_{BMU}(trk, stub)$	< 9 cm
CMU	Fiducial requirement	CMU
	$\Delta x_{CMU}(trk, stub)$	< 7 cm
CMP	Fiducial requirement	CMP
	$\Delta x_{CMP}(trk, stub)$	< 5 cm
SCMIO	Fiducial requirement	Stub not fiducial
	$E_T^{EM} + E_T^{HAD}$	> 0.1 GeV
CMIO	Stub	No stub
	$E_T^{EM} + E_T^{HAD}$	> 0.1 GeV
CMXNT	Fiducial requirement	CMX
	$\Delta x_{CMX}(trk, stub)$	< 6 cm
	ρ_{COT}	< 140 cm
	Trigger	CMX trigger not fired

Table 3.2: Summary of muon identification requirements [6].

as the momentum of the candidate track divided by the total momentum of all tracks within the 0.4 cone of the candidate track. When the track isolation is 1, this means there is no other tracks in the 0.4 cone of the candidate track. In this analysis, the cut for the track isolation is at 0.9. Moreover, an isolated track will be removed if it is within the 0.4 cone of any tight jets (see Section 3.2.2 for a discussion of jet reconstruction).

Since this kind of lepton only requires the information from the tracking subdetector, it will recover charged leptons lost due to the inefficiencies and incomplete coverage of the calorimeter and muon systems.

3.2.2 Jet Identification

Due to the confinement properties of QCD, the partons (quarks and gluons) generated from the hard scattering cannot exist as free particles. They must form colorless hadrons. This process is called hadronization or showering. In this process, a large number of stable particles are generated and they are traveling in approximately the same direction. Thus, in this analysis, a jet is defined as a cluster of energy in the calorimeters that is not associated with a reconstructed electron.

The algorithm [43] used to reconstruct jets is similar to the clustering algorithm used for electrons. The algorithm for jets only utilizes the information from the calorimeter system. This algorithm starts with a seed list, which includes all of the towers with more than 1 GeV of energy deposited and sorted in decreasing order of energy. Starting with the highest energy seed tower, all of the towers are combined with the seed that have more than 100 MeV of energy and are located within the 0.4 radius in the $\eta - \phi$ plane. Then the energy-weighted center with all of the added towers is calculated and is used as the new center of the jet cone. The towers of the jet are recalculated with the new center. This process is iterated until the center position is stable between iterations.

After running the clustering algorithm on each seed tower, jets may overlap with each other. If the total energy of all overlapping towers is larger than 75% of the lower energy jet, then the two jets are combined. Otherwise, the overlapping towers are assigned to the jets with the closer center.

Jet Energy Scale Correction

The ultimate goal for the jet-reconstruction algorithm is to obtain the energy and the momentum of the parton that the jet originates from. However, this is a difficult physics quantity to estimate.

Among all the secondary particles generated inside a jet cone, neutrons leave only limit amount of energy in the EM calorimeter, while neutrinos leave no energy at all in both EM and hadron calorimeters. In addition, some secondary particles may leave energy outside the jet cone. Also the jet energy response is different in different regions of the calorimeter. Thus, jet energy corrections are applied to the raw energy measured for each jet cone.

For analysis of the CDF jet data, there are five levels of energy correction available [44]. L1, η-dependent response, f_{L1}; L4, effects of multiple interactions, A_{L4}; L5, absolute energy scale, f_{L5}; L6, underlying event, A_{L6}; and L7, out-of-cone correction, A_{L7}. All of the corrections can be applied to the raw energy according to the following equation:

$$E^{corr} = (E^{raw} f_{L1} - A_{L4}) f_{L5} - A_{L6} + A_{L7} \tag{3.2}$$

In this analysis only corrections up to level 5 are used. Since the L6 and L7 corrections are only important to the particle mass measurement, they are not crucial in this cross section measurement, in which only the relative ratio between the data and the simulation is important.

The uncertainty (σ_{JES}) on the final corrected jet energy is based on different corrections. The relative values of the individual uncertainties are shown in Figure 3.3.

A recent study of CDF data [45] shows that the jet energy correction depends on the type of the parton initiating the jet. For jets originating from gluons, the jet-energy correction needs to be lowered by about two times the correction uncertainty ($-2\sigma_{JES}$), as shown in Figure 3.4. This correction is implemented in the analysis described here. However, the effects of this correction are negligible, since the signal region used in this analysis is defined in the heavy-flavor region, where the fraction of gluon jets is quite small.

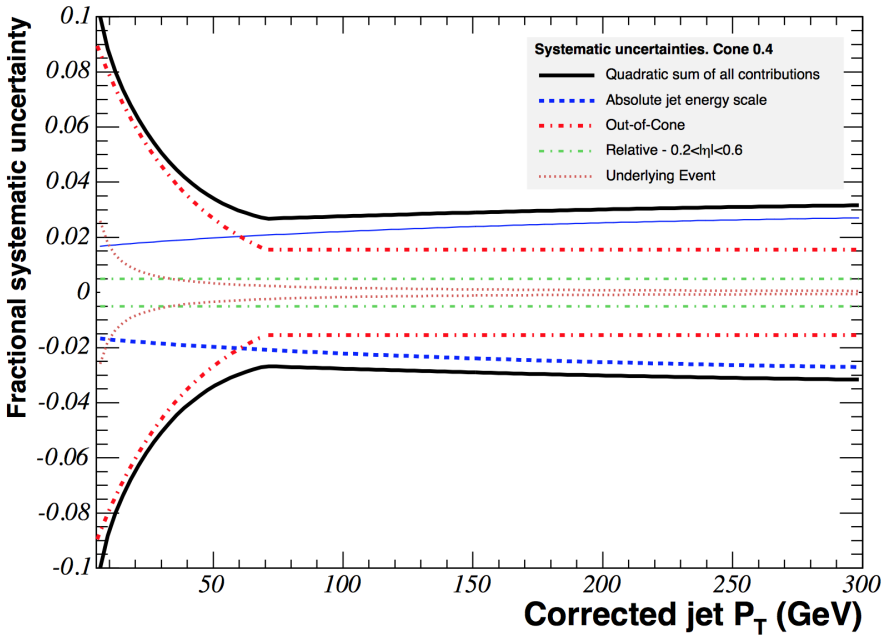

Figure 3.3: The relative uncertainty of different jet-energy-correction terms versus the jet p_T.

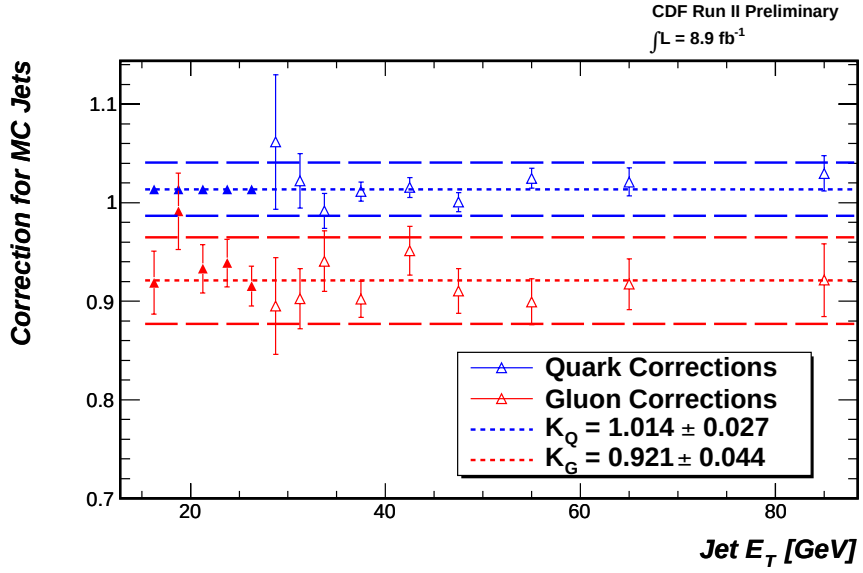

Figure 3.4: Correction for both simulated gluon and quark jets as dependence of jet E_T.

η-dependent correction The performance of the calorimeters in different η regions varies due to the different clustering performance of the central and plug calorimeter and also due to cracks between the calorimeters. The correction is calculated using dijet samples, requiring that one jet (trigger jet) is in the $0.2 < |\eta| < 0.6$ region, where the calorimeter performs best, the other one (probe jet) is in the region $|\eta| < 3.6$. The correction factor is calculated by adjusting the probe jet to balance the transverse momentum. The factor calculated depends on both η and jet p_T, as shown in Figure 3.5.

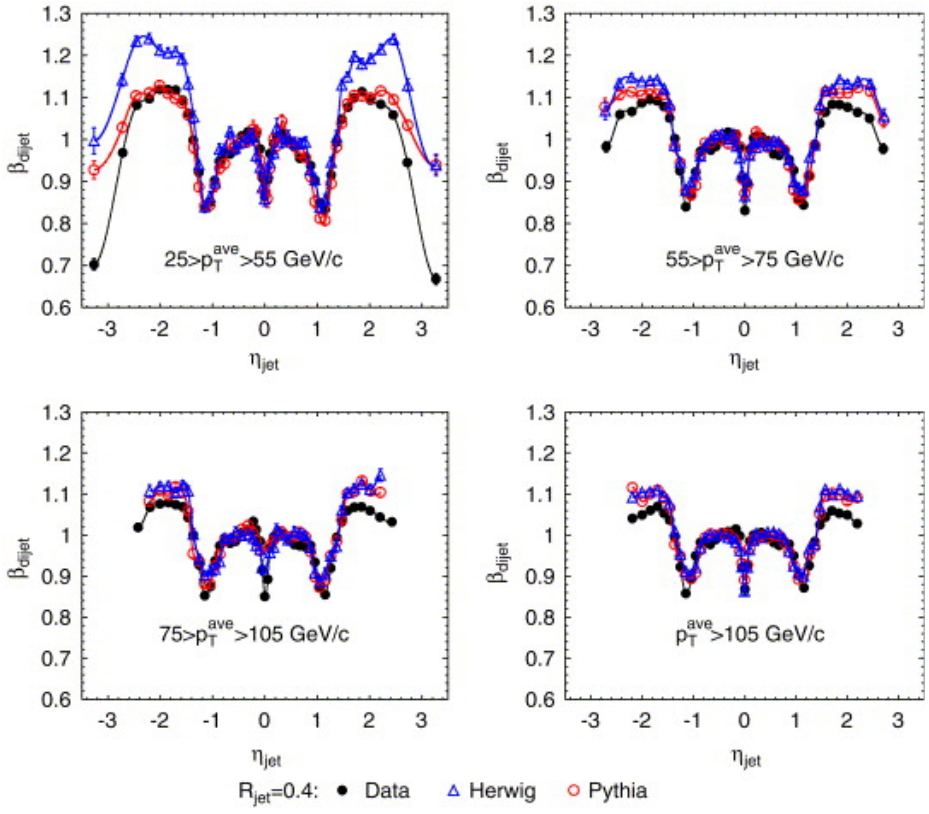

Figure 3.5: The η dependence of the correction factor, calculated for both data and simulation. The factor is calculated in different jet p_T and η region.

Multiple-interaction correction The number of interactions in each bunch crossing follows a Poisson distribution. At the Tevatron, the average number of vertices increases with the instantaneous luminosity, and ranges up to 8 for the highest instant luminosity. The energy correction is derived by measuring the energy deposited in a jet cone in a random direction with $0.1 < |\eta| < 0.7$ using events from the minimum-

bias trigger. The correction value depends on the cone size and number of vertices in the event, as shown in Figure 3.6.

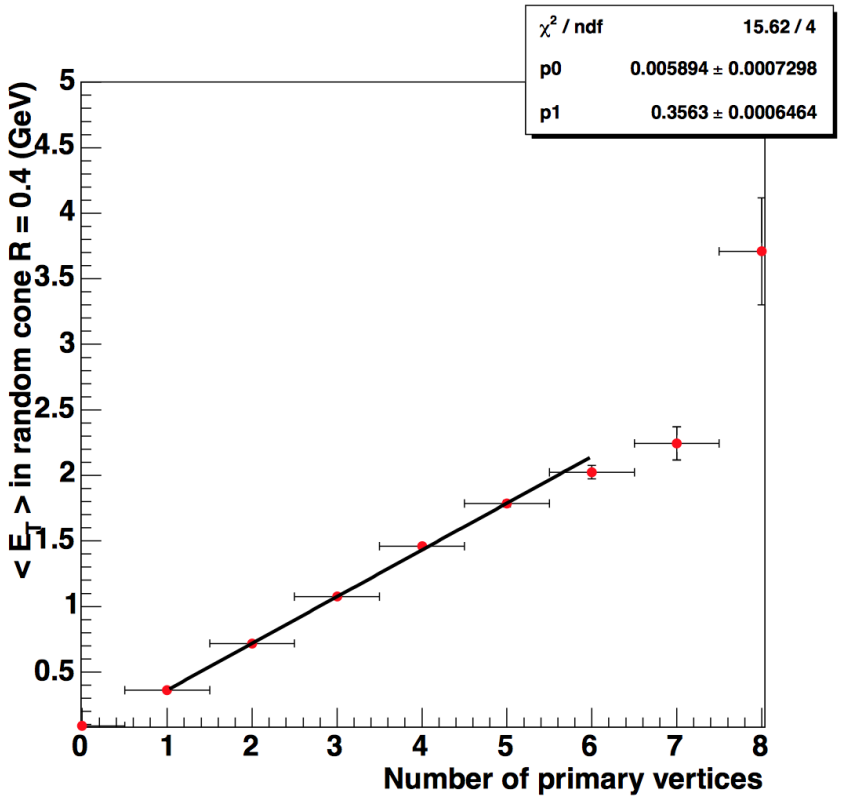

Figure 3.6: E_T correction as a function of number of vertices of 0.4 jet-cone size.

Calorimeter-response correction This correction is aimed to correct the jet energy measured in the calorimeter to the true energy of the particle that the jet originates from. This correction is derived from the simulation, by using inclusive dijet events. Jets are clustered both before and after the simulation of detector response using the same algorithm. The jets reconstructed at different levels are matched to each other if the distance in the $\eta - \phi$ plane is less than 0.1. The correction parameter is derived by comparing the two different level matched jets. Figure 3.7 shows the parameter as a function of jet p_T for three different cone sizes.

Underlying event and out-of-cone correction The L6 underlying event correction considers the energy from the partons not involved in the hard scattering or from the

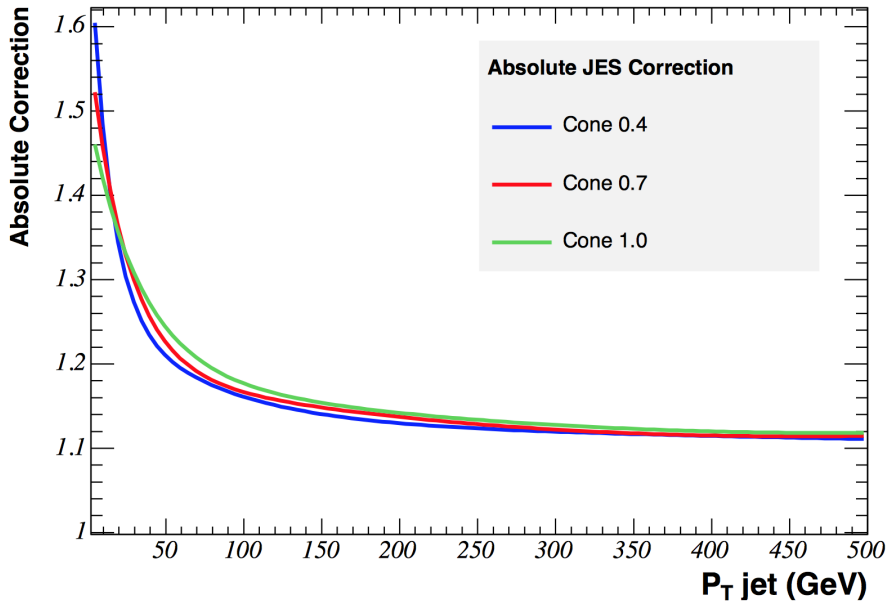

Figure 3.7: Calorimeter-response correction (L5) as a function of jet p_T for different cone size.

initial-state radiation gluons. This correction needs to be subtracted from the L5 corrected jet energy.

The L7 out-of-cone correction considers the energy coming from the same parton, but is deposited outside the jet cone. It is derived using the same method as the L5 correction.

Correction for jet originating from bottom quark Another correction, other than the standard ones described above, is also used in this analysis for the top-quark mass and the Higgs boson mass estimation. Since muons or neutrinos are much more likely to be produced in the showering process of a bottom quark, the standard jet energy correction is not sufficient here to fully reconstruct the energy of b jets. A special correction [46] to be applied to the L5-corrected jets is developed. In this correction, variables related to the b-jet tagging are used as input variables, and a neural network is developed to calculate the correction factor to be applied to the L5-corrected b jets. In the training process, a scaling factor is derived by comparing the true energy and the L5 corrected one in the Higgs boson decaying to bb simulations, similar

to the methodology used in the L5 correction. The distribution of correction values calculated from the neural network is shown in Figure 3.8. Although this method is derived in the Higgs boson simulation, as tested, it is also valid for the b jets in other processes.

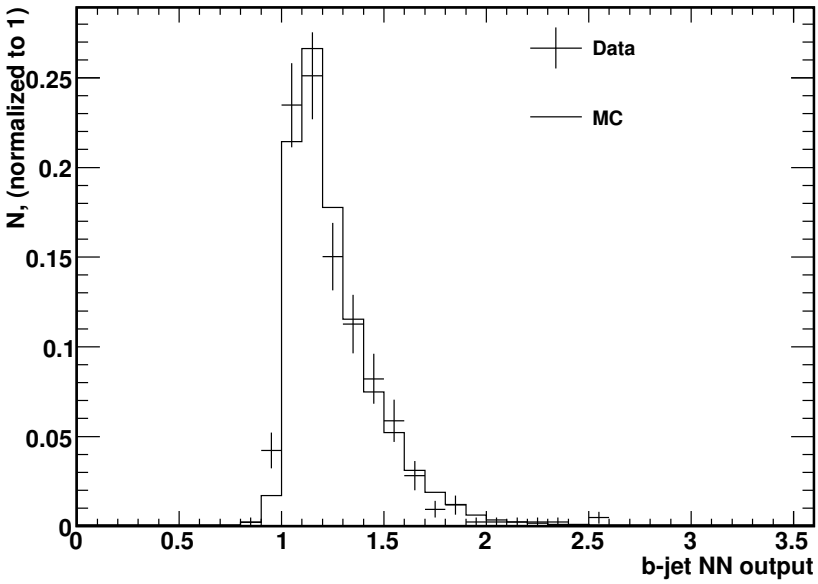

Figure 3.8: The jet energy correction value for b jets calculated by the neural network algorithm.

3.2.3 Neutrino Reconstruction

The neutrino is the only particle that cannot be detected by the CDF detector, as it leaves no energy in the detector. The transverse energy of the neutrino can be derived from the principle of total momentum conservation in the transverse plane. Thus the missing E_T is defined as

$$\not\!\!E_T{}^{raw} = -\sum_i \vec{E}_T^i, \tag{3.3}$$

where $\vec{E}_T^i = E \sin\phi \hat{n}$. this means that the transverse energy of a given tower is defined as the transverse component of the energy in the direction from the beam line to the tower. The missing E_T is then the negative vector sum of E_T of all the towers with more than 100 MeV energy deposited. This value is sometimes also noted as the raw $\not\!\!E_T$, since it is not corrected for the muons and the jet energy.

The final number of the $\not\!\!E_T$ used in the analysis needs to corrected for the muon energy, which leaves a minimum amount of energy in the calorimeter; and the corrected jet energy. The final $\not\!\!E_T$ can be calculated using this equation,

$$\not\!\!E_T = \not\!\!E_T{}^{raw} - \sum_{muons} p_T + \sum_{muons} E_T - \sum_{jets}(E_T^{corr} - E_T). \tag{3.4}$$

In this analysis, the $\not\!\!E_T$ is taken as the transverse component of the neutrino energy. However, the longitudinal component of the neutrino cannot be determined in the same way. Instead, the longitudinal component can be constrained by applying the W boson invariant mass requirement, since in this analysis all the neutrinos originate from the decay of a W boson. The z-component of the neutrino momentum is calculated by solving a quadratic equation, where the four vector of the charged lepton is well measured and the invariant mass of the W boson is well known. When there are two solutions, the smaller one is chosen; when there is no real solution, only the real part of the solution is used [47]. Comparison of the z-component of the neutrino momentum between the generator level and the reconstructed level are shown in Figure 3.9.

3.2.4 Top Quark Reconstruction

There are two b jets in this analysis. For the single top analysis, correctly choosing the one that from the top quark decay is important since it improves the measurement of the top quark mass. A neural network is developed to choose the correct jet from the top quark decay. The technical details of neural networks are described in Section 6.1. In this algorithm, the b-jet energy correction is applied to both jets in addition to the L5 jet energy correction. The following variables of both jets are used:

- jet p_T;
- invariant mass of one jet and the charged lepton $M_{\ell j}$;
- invariant mass of one jet, the charged lepton, and neutrino $M_{\ell\nu j}$;
- the charge of the lepton times the direction of the jet in the reconstructed top-quark rest frame $Q \times \cos\theta_j$.

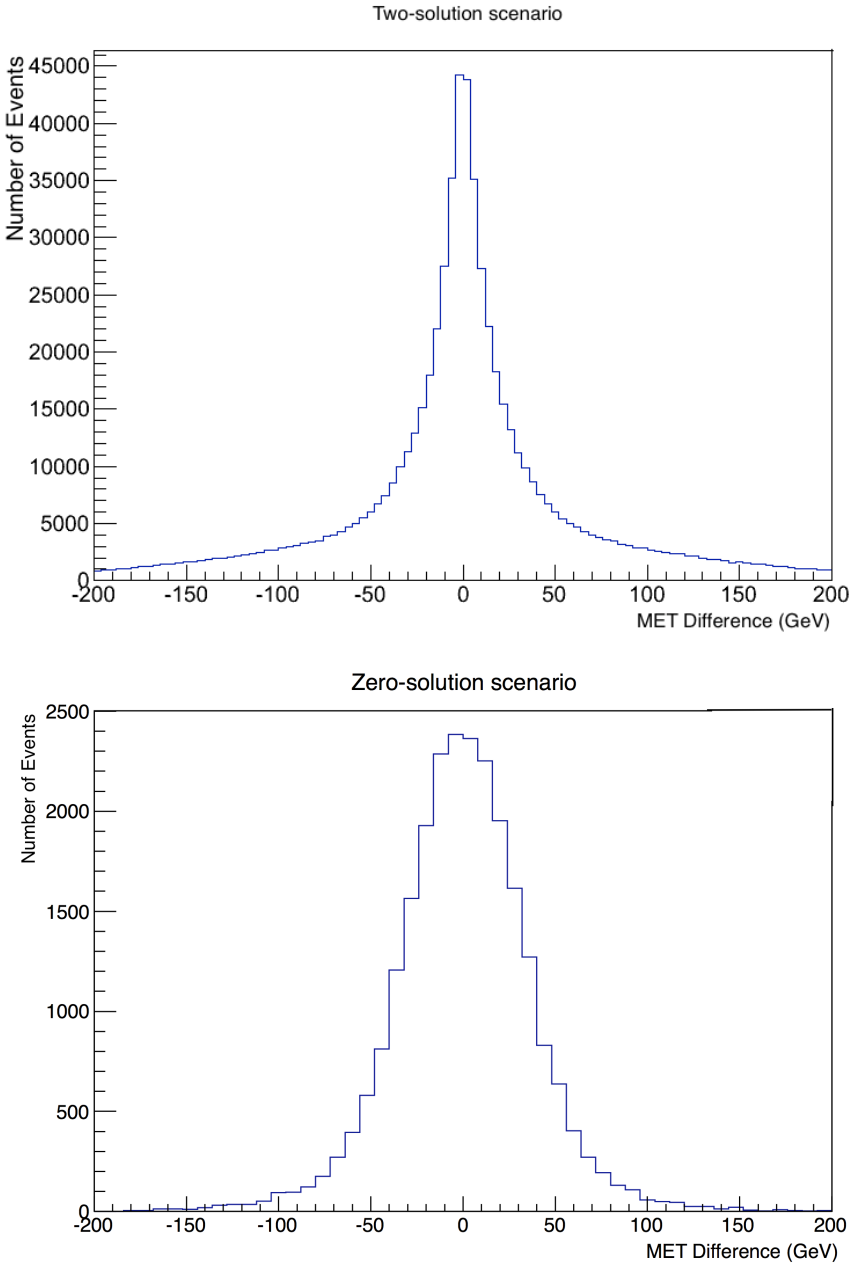

Figure 3.9: Difference between the generator level z component of neutrino momentum and reconstructed level one. The first figure is the two-solution scenario, while the second one is the zero-solution one.

The comparison of selected variables of the two jets are shown in Figure 3.10.

Based on the neural network output value, a decision is made to choose whether the jet with higher E_T is from the top quark or *vice versa*. Also, an optimal cut is selected to maximize the probability of choosing the correct jet. As tested with the *s*-channel single top quark simulation, the correct jet can be selected in about 82% of events. In the previous single-top-quark analysis at CDF, the jet with the smaller $|\eta|$ value is chosen to be the jet from the top quark, which is not appropriate for the *s*-channel measurement. A comparison of the reconstructed top quark mass resolution using this algorithm with the previous one is shown in Figure 3.11.

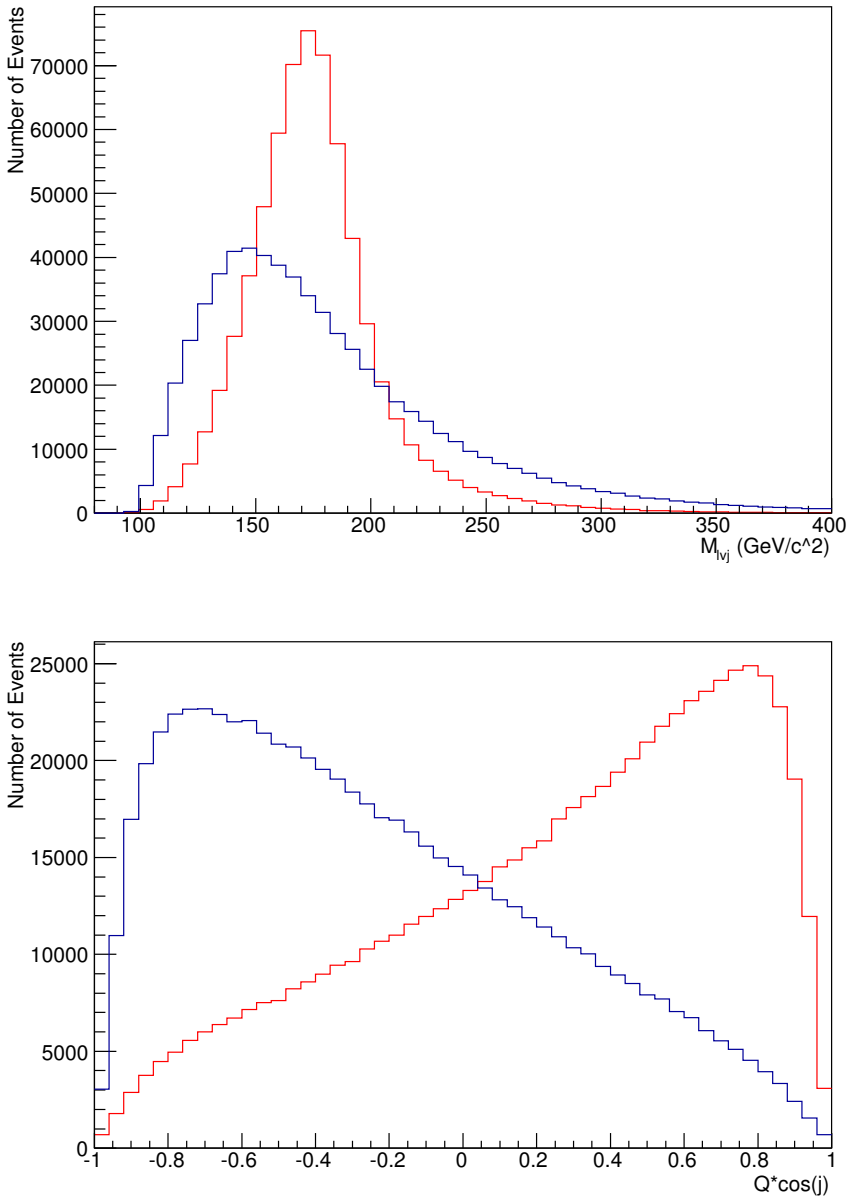

Figure 3.10: The comparison of input variable between the jet from top quark (the red one) and the jet not from top quark (the blue one), using single top quark s-channel simulation data. The top one is M_{lvj}; and the lower one is $Q \times \cos\theta_j$.

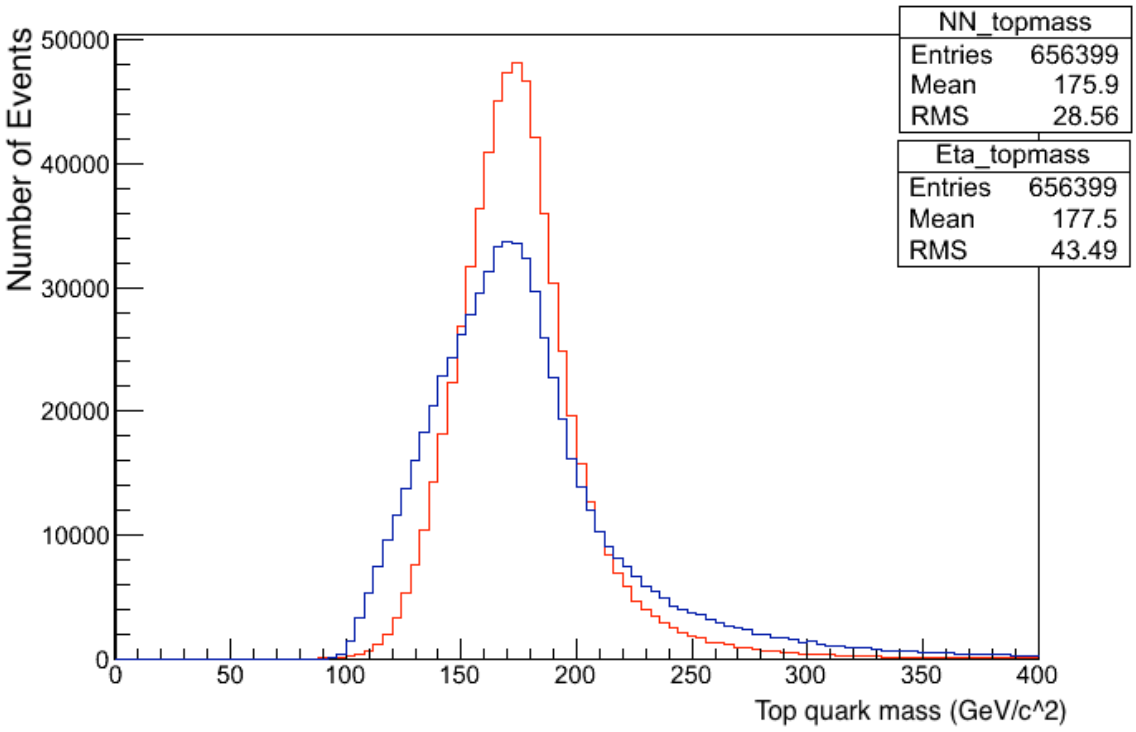

Figure 3.11: The comparison between the previous top quark reconstruction algorithm (the blue one) and the current one (the red one).

Chapter 4

Event Selection

In order to search for a Higgs boson or successfully measure the cross section of single-top-quark production in the s-channel, appropriate requirements must be applied to the recorded data to create a signal enriched sample without loosing too much of the signal events.

The final states for both the single-top-quark s-channel and the $WH \to \ell\nu\, bb$ processes are a W boson and two bottom quarks. In this analysis, only those Ws that decay into an electron or a muon are included. Actually, the branching ratio for the hadronic decay of W is twice as large as the leptonic decay. Moreover, τs have hardly been included in this analysis. (Only those τs that decay to produce an electron or a muon are included.) This means that only about 20% of τ events are included by our event selection requirements. However, these requirements are worth the loss of signal since backgrounds are significantly reduced by requiring one charged lepton in the final state. Thus, the signal-to-background ratio actually goes up.

The final particles that we are looking for are one charged lepton, one neutrino (large $\not\!\!E_T$), and two b jets. In order to choose events consistent with our requirements, two stages of event selection are applied: online selection, described in Section 4.1 and offline selection, described in Section 4.2. The final state of the single-top-quark s-channel process is the same as the final state of the WH analysis, thus the techniques used here are the same as the ones used in the WH search.

4.1 Online Event Selection

The online selection is achieved by applying trigger requirements. As described in Section 2.3, a powerful trigger system is implemented to select which events are interesting and should be recorded for offline analysis. Moreover, all events are stored into different data sets according to the trigger used. As discussed in the previous section, triggers associated with high-p_T leptons are used. In order to improve the muon coverage, $\not\!\!E_T$-based triggers are also included. The data sets used in this analysis are list below:

- High-p_T central electron: *bhel*;
- High-p_T plug electron: *bpel*;
- High-p_T central muon: *bhmu*;
- Large $\not\!\!E_T$: *emet*;

During the last iteration of the Higgs boson search at CDF, an inclusive trigger selection for CEMs and CMUPs was implemented to further improve the lepton trigger coverage. Moreover, new triggers dedicated to CMU or CMP muons were also added to improve the muon trigger acceptance. These improvements increased the total lepton acceptance by about 5%.

4.1.1 Electron Triggers

The trigger path used for central electrons is ELECTRON_CENTRAL_18, and all the events satisfy this trigger, along with other central electron related triggers, are stored in the *bhel* data set.

Similar to the offline CEM electron definition, the trigger requirement for CEM is an EM calorimeter cluster matched to a high-p_T track. The requirements are divided into three levels, with the most relaxed one at level one, and more and more sophisticated requirements later on. At level one, this trigger requires a reconstructed track with $p_T > 8$ GeV/c, one central calorimeter tower with $E_T > 8$ GeV, and for the tower $E^{HAD}/E^{EM} < 0.125$. At level two, an EM calorimeter cluster with $E_T > 16$ GeV is required and it must be

matched to a high-p_T track. At level three, where a full event reconstruction is performed, the E_T cut for the electron is increased to 18 GeV, and a matching requirement for $|\Delta z| < 2$ cm, the distance between the track and cluster in the z direction, is also applied.

Since no trigger is 100% efficient, the efficiency of the trigger must be estimated. For this electron trigger, the efficiency calculation comes from two parts of the detector: the tracking part and the calorimeter part. At CDF, the tracking efficiency is calculated by selecting a pure sample of events containing a real $W \to e\nu$ boson, using a trigger which does not require any information from the tracker. For the calorimeter part, a backup trigger is used. The average trigger efficiency for CEM is about 95.6%$\pm$0.3 with an E_T and η dependence.

Events with an electron in the forward region are triggered by PHX-related triggers, and are stored in the *bpel* data set. This type of trigger requires a track reconstructed by PHX algorithm because of the limited coverage of the COT detector. A $\not\!\!E_T$ cut is also applied to select a W-boson event. This lepton category is used in the Higgs boson search analysis, but has minimal sensitivity and it is not included in the single-top-quark s-channel measurement.

Untriggered CEM

Since the efficiency for the CEM trigger is not 100%, there are still some central electron events in the data that do not pass the trigger requirements. However, at CDF there is a special trigger designed to check all the events reconstructed at level three to look for a CEM electron. And if a CEM electron is found, the event will still be stored in the *bhel* data set under the name of ELECTRON_20_VOLUNTEER.

These extra CEM events are included. The purity of these extra events are checked to be the same as all other CEM events. Since these CEM events are selected from all of the level-1 and level-2 triggers, the same method to estimate the trigger efficiency cannot be used. A method called “bootstrapping” is used to estimate the full CEM trigger efficiency when these extra events are included. The new trigger efficiency is calculated using the

following equation:

$$\epsilon_{bhel} = \epsilon_{CEM} * (1 + Gain(\eta)) \tag{4.1}$$

Since there is little inefficiency for CEM trigger where $|\eta| < 0.5$, the gain by including extra CEMs also depends on η. Thus, the final efficiency number is calculated from the efficiency of the CEM trigger and a scale factor depending on η. As tested with data, the new trigger strategy increases the CEM events by 4.6%. This increases the trigger efficiency for CEMs to almost 100%.

4.1.2 Central Muon Triggers

Central muons are selected by two trigger paths: MUON_CMUP18 and MUON_CMX18, and all the events that fired these two triggers are stored in the *bhmu* data set.

Similar to the offline CMUP and CMX reconstruction, these two triggers also require a high-quality high-p_T track matched to a stub in the muon detectors. For CMUP, at level one, a track with $p_T > 4$ GeV/c and a stub in both the CMU and CMP detectors are required. At level two, the p_T requirement for the track is increased to 15 GeV/c, and the energy deposit in the calorimeters in the path of the reconstructed track must match to the signature of a minimum ionizing particle. At level three, a fully reconstructed track with $p_T > 18$ GeV/c is required, and the matching requirements, $|\Delta x_{CMU}| < 10$ cm and $|\Delta x_{CMP}| < 20$ cm, are also applied. The requirements for the CMX trigger are similar, except that the stub has to be in the CMX detector.

The trigger-efficiency calculation for CMUP and CMX trigger uses a sample of di-muon events, of which one muon is required to be a CMUP, while the other one has to be a CMX. The invariant mass of these two muons needs to be within the Z boson mass window. This ensures the purity of muons. In this way, the trigger efficiency for CMUP can be calculated using following equation:

$$\epsilon_{CMUP} = \frac{N_{CMUP\&CMX}}{N_{CMX}} \tag{4.2}$$

Similarly, the trigger efficiency for CMX is calculated by:

$$\epsilon_{CMX} = \frac{N_{CMUP\&CMX}}{N_{CMUP}} \tag{4.3}$$

As checked, both efficiency numbers do not depend on kinematic variables.

Untriggered CMUP

Similar to CEMs, there is also a trigger, MUON_CMUP18_VOLUNTEER, at level three to collect all the events that do not fire the CMUP trigger but with a CMUP muon. Including these extra CMUP events increases the CMUP acceptance by 12.6%. To calculate the final trigger efficiency for the CMUP muons, the same "bootstrapping" method as CEM is employed. Since the trigger efficiency for CMUP muons does not depends on the kinematics, a flat number for all CMUP muons is evaluated.

Thus, the final trigger efficiency number for CMUP is $\epsilon_{CMUP} = 98\%$ with all the recovered CMUP muons. The efficiency for CMX is $\epsilon_{CMX} = 89.5\%$ with standard CMX requirement.

Gap Muons

In the *bhmu* data set, there are two types of muons in addition to CMUP and CMX – CMU-only and CMP-only muons. They were not used in the previous analysis in this channel, and they were implemented into the analysis as the first step of my work at the CDF experiment.

As described in the detector part, there are gaps and cracks in both the CMU and CMP detector. The traditional way to define a reconstructed muon is to require that both the CMU and CMP detectors have a hit in the muon chambers. However, because of the imperfect coverage of the CMU and CMP detector, it is possible that a muon passes through the gaps of one detector and fires the other one. To improve the muon coverage, two dedicated triggers were implemented early in CDF Run II. However, those triggers were never used in the single top quark analysis, and these events were only included by $\not\!\!E_T$ triggers previously, which are not as efficient as the dedicated lepton triggers.

The online requirements for CMU and CMP triggers are similar to the CMUP triggers except that only one of the muon detectors is required to observe a muon signal, and the reconstructed track has to be matched to the gap of the other muon detector. This is possible only after fast online track reconstruction is achieved. The trigger designed for CMU is MUON_CMU18_ETAGAP_3DMATCH_DPS, and was implemented in the second half of the run, while the trigger dedicated to CMP is MUON_CMP18_PHIGAP_3DMATCH_DPS, and was implemented after one third of the run.

The trigger-efficiency calculations for these two triggers are challenging. A multivariate analysis method is employed. Neural networks are used to parametrize the trigger efficiency based on the p_T, η, and ϕ of the muon. The data samples used to calculate the trigger efficiency are selected using $\not\!\!E_T$-type triggers which is unbiased to the CMU and CMP triggers. During the calculation, the fiducial requirement of CMU and CMP leptons are applied to the training samples. The final average trigger efficiency number applied to the simulated events are about 61% for CMP and 41% for CMU. These numbers take the trigger live time and the prescale of triggers into consideration. The actual efficiency value applied to the simulation is calculated based on the kinematics of the muons of each event.

4.1.3 Large Missing Transverse Energy Triggers

Because of the limited muon detector and tracking system coverage, there are still many events with a high-p_T muon that escape our previous selection. To increase the event acceptance, three triggers that only require large $\not\!\!E_T$ or large $\not\!\!E_T$ with two jets are used. All the $\not\!\!E_T$-related triggers are stored in the *emet* data set. Moreover, since the muons leave limited amount of energy in the calorimeter and the $\not\!\!E_T$ value at trigger level is not corrected for the muon energy, the $\not\!\!E_T$ at trigger level is even more enhanced, so using $\not\!\!E_T$-based triggers is more efficient with muon events than what one would expect based on the neutrino E_T.

Since events could be stored into multiple data sets when two or more triggers are fired at CDF, in order to avoid double counting events, only events with loose muons

or ISOTRKs are selected (defined in previous chapter). Moreover, since CMU and CMP dedicated triggers in *bhmu* data set are used, events in the *emet* data set that fired the CMU or CMP trigger are vetoed.

The extra $\not\!\!E_T$ triggers used in this analysis are: MET45, MET2J, and METDI. The detail definition of these triggers changed over the data taking period due to the increase of the instant luminosity. However, the main characteristics remained the same and are listed below:

MET45 This trigger only requires the $\not\!\!E_T$ value. In the first third of the run, the $\not\!\!E_T$ cut was 45 GeV, and later on the cut value is decreased in order to increase the acceptance. The final version used for this trigger requires that the $\not\!\!E_T$ at level one is 28 GeV, and 40 GeV at level 2 and level 3. However, this $\not\!\!E_T$ cut is too high for some physics processes, so the following two triggers are also introduced.

MET2J This trigger requires the $\not\!\!E_T > 28$ GeV at level one, and two jets at level two. And one of the two jets has to be in the central region. At level three, the requirements increased to $\not\!\!E_T > 35$ GeV. This trigger has a dynamic prescale in order to decrease the trigger rate at high instantaneous luminosity.

METDI This trigger is similar to the previous one. The only difference is this one requires $\not\!\!E_T > 28$ GeV and at least one jet at level one.

From the description, it is obvious that all three $\not\!\!E_T$ triggers are correlated to each other. Thus, an algorithm [48] was developed to calculated the trigger efficiency when combining events from all three triggers. This algorithm comes in two parts: the first one is to parametrize the trigger efficiency versus $\not\!\!E_T$, second one is to choose the right trigger efficiency number and assign it to each simulated event.

The parametrization of the $\not\!\!E_T$ trigger is calculated by selecting the events from MUON_CMUP18 trigger, and cuts for the muon p_T and jets E_T are applied. After applying these cuts, the trigger efficiency for $\not\!\!E_T$ triggers are now independent of kinematics of muons and jets. Thus, the dependence of trigger efficiency versus $\not\!\!E_T$ value can be calculated.

To combine all three triggers, for each simulated event, the trigger efficiency for all three triggers are calculated. The $\not\!\!E_T$ trigger which has the largest trigger efficiency will be

assigned to scale the simulation event. This method will maximize the event acceptance when using the $\not\!\!E_T$-based triggers.

4.1.4 Data Quality and Luminosity Estimation

With all the triggers selected and trigger efficiency calculated, the next step is to apply quality requirements to all the data collected and calculate the corresponding integrated luminosity. The luminosity is a quantity to characterize the number of collisions in a collider, and is needed to estimate the expected number of events of any physics processes.

A common way to apply data quality requirement is to require that all sub-detectors are fully functional. However, in order to collect as much data as possible, a new way to require the data quality is assigned in the latest *WH* analysis. In this new method, the silicon detector (important for b tagging) and calorimeters (for jet reconstruction) are always required to be functional. But since only one lepton is required in each event, the detector used for electron detection (shower maximum detectors) and muon chambers are decoupled. They are not required to be operational at the same time. In this way, the available luminosity is increased by about 8%.

With the latest data quality requirement, the integrated luminosity varies for different lepton categories and are listed below for each category:

1. For CEM and PHX, $\int \mathcal{L} = 9.4\text{fb}^{-1}$
2. For CMUP, $\int \mathcal{L} = 9.5\text{fb}^{-1}$
3. For CMX, $\int \mathcal{L} = 9.4\text{fb}^{-1}$
4. For extend muons, $\int \mathcal{L} = 9.3\text{fb}^{-1}$

4.2 Offline Event Selection

With all the high-quality data selected, and all physics objects reconstructed, several selection cuts need to be applied in order to remove backgrounds as much as possible, and increase the signal purity in the desired region.

Since this analysis relies heavily on the simulation to predict most of the backgrounds, one general concern for the selection cuts is that the cut efficiency may be different for data and simulation. In these cases, a scale factor is applied to the simulation to solve the problem. Usually, the scale factor is defined as

$$SF = \frac{\epsilon_{data}}{\epsilon_{MC}} \tag{4.4}$$

In this analysis, scale factors are applied to leptons and b tagging to correct for the difference between simulation and data.

4.2.1 Event Vetoes

There are several classes of background events that could pass the online event selection requirements stated in the previous section. Luckily, some of them have unique event properties that can be used to distinguish them from signal events during offline analysis.

Primary Vertex Requirement

Most of the time, the hard scattering events, in which the signal process is produced, happen near the center of the detector. However, some background events, like cosmic ray events do not have this feature. Thus, those backgrounds can be removed by applying requirement on the position of the primary vertex along the beam line (the z axis). At CDF, we require $|z| < 60$cm. This requirement also ensures that the interactions happen at where the detector coverage is sufficient. However, some hard scattering events happen outside of this range. To correct this, the efficiency for this requirement is measured using beam data events and is applied as a correction to the measured luminosity:

$$\epsilon_{|z|<60\text{cm}} = 97.43 \pm 0.07\% \tag{4.5}$$

.

Cosmic Ray Veto

Muons which originate from the decay of cosmic-ray pions could pass the detector at the same time as a hard-scattering event. These muons fire the detector in the same way as muons from the collision. Thus, an algorithm utilizing information from the muon chambers, TOF, and COT detector is implemented to remove the cosmic-ray muon events.

Events that meet one of the following requirements are considered cosmic-ray muon events. Firstly, when there are two muon tracks in a event having the same impact parameter but with a large angle between them, then they are more likely to be from the same muon originating from outside of the detector. Events with this type of muon is labeled as cosmic-ray muons. Secondly, cosmic-ray muons are less likely to be close to the primary vertex. Thus, events with a large difference of energy-weighted primary vertex and the vertex with reconstructed muon tracks are labeled as cosmic-muon event. Lastly, the TOF timing system is also used to identify cosmic muons. When the time stamp of the bottom muons is more than 5 ns later than the upper muons, the event is identified as a cosmic ray muon event.

This vetoing algorithm removes about 100% of the cosmic-ray events, and with a negligible loss of signal.

Dilepton Veto

Top pair production ($t\bar{t}$) events are similar to the signal events except that they have two leptons. In order to reduce this kind of backgrounds, we look for all the possible leptons in an event, including loose leptons. The events with more than one lepton are rejected. This vetoing algorithm can significantly reduce the $t\bar{t}$ background.

Z Boson Veto

Z boson + jets events could also pass the event selection requirements, when one of the leptons from the Z boson decay fails to be reconstructed, and the mismeasurement of jet energy creates enough $\not\!\!E_T$ to pass the $\not\!\!E_T$ cut. A Z boson vetoing algorithm is implemented only for tight leptons: CEM, PHX, CMUP, and CMX. The reconstructed

lepton is matched with any loose leptons with an opposite charge (including clusters in the EM calorimeter or high-quality isolated tracks) to verify the invariant mass of the two objects. If the invariant mass falls into the Z boson mass range, from 76 to 106 GeV/c^2, this event is identified as a Z boson event and will be removed.

Multijet Background Rejection

Multijet backgrounds are events where a jet passes the high-p_T lepton selection requirement and the $\not\!\!E_T$ is produced due to mismeasurement of the jet energy. In this type of event there is no real W boson. Although the rate of a multijet event to fake a W boson event is low, multijet events happen with a very high event rate and this type of background is still a non-negligible background in this analysis.

To remove the multijet background as much as possible, a multijet rejection package is developed using the Support Vector Machine (SVM) algorithm [49].

SVMs are trained independently for the central and forward detector regions. The training samples used are the CEM and PHX samples. Since the input variables used are not related to some electron specific variables, such as cluster or tracks, the SVMs are also valid to other lepton categories.

The input variables used for CEM are

- M_T^W, $\not\!\!E_T{}^{raw}$, $\not\!\!p_T$, $\Delta\phi(\ell, \not\!\!E_T)$, $\Delta R(\ell, \nu)$, $\not\!\!E_T{}^{Sig}$, $\Delta\phi(jet1, \not\!\!E_T)$, $\Delta\phi(\not\!\!p_T, \not\!\!E_T)$,

while the variables used for PHX are

- M_T^W, $\not\!\!E_T{}^{raw}$, $\not\!\!p_T$, $\not\!\!E_T{}^{Sig}$, $\Delta\phi(jet1, \not\!\!E_T)$, $\Delta\phi(\not\!\!p_T, \not\!\!E_T)$.

The reason that less variables are used for PHX is that there is no high-quality reconstructed tracks in the forward region because of the limited coverage of the COT detector.

Because of the different contamination level of multijet events for different lepton categories, the cut value of SVMs applied are also different. The details are listed below,

- $SVM_{CEM,EMC} > 0$
- $SVM_{CMUP,CMX} > -0.5$

- $SVM_{PHX} > 1$

After this SVM multijet rejection, the amount of multijet events in this analysis are reduced to a sub-dominant level.

4.2.2 $W \to \ell\nu$ Selection

In this analysis, only the leptonically decayed W boson is considered. We look for one charged lepton and the corresponding neutrino in the final state. For the charged leptons, only events with one reconstructed electron or muon are selected. We do not explicitly look for a reconstructed τ, but the leptonically decayed τs are included by requiring an electron or a muon. Neutrinos cannot be detected by the CDF detector, we require $\not\!\!E_T$ in the final state as a signature of the undetectable neutrino.

Lepton Selection

As stated in the previous section, we select exactly one lepton in the final state. The charged lepton candidate comes from the lepton categories described in Section 3.2.1. The lepton categories used in this thesis are as follows: CEM, PHX (tight electron), CMUP, CMX (tight muon), BMU, CMU, CMP, CMIO, SCMIO, CMXNT (loose muon), and ISOTRK. By including all the lepton categories, the lepton coverage of the analysis is maximized.

The efficiencies for the reconstruction algorithms are different between the data and simulation. Thus, a scale factor is applied to the simulated events to match the data. The scale factors for lepton identification are calculated by comparing $Z \to \ell\ell$ events in simulation and data, using following equation

$$SF^{\ell} = \frac{eff_Z^{Data}}{eff_Z^{MC}} \tag{4.6}$$

The final scale factor for the full data set are summarized in Table 4.1.

However, the different reconstruction algorithms used here are not strictly orthogonal to each other. Some of them share the same $\eta - \phi$ space. This means that one lepton could be reconstucted by multiple algorithms. The scale factor calculation algorithm described

CEM	PHX	CMUP	CMX	BMU	CMU
0.973 ± 0.005	0.908 ± 0.009	0.868 ± 0.008	0.940 ± 0.009	1.06 ± 0.02	0.88 ± 0.02
CMP	CMIO	SCMIO	CMXNT	ISOTRK	
0.86 ± 0.01	0.97 ± 0.02	1.02 ± 0.01	0.940 ± 0.009	0.94 ± 0.04	

Table 4.1: Scale factors for lepton identification efficiencies for the full CDF Run II data set.

above does not take this effect into consideration. At CDF, the lepton reconstruction algorithm is prioritized in the following order: $CEM > PHX > CMUP > CMX > BMU > CMU > CMP > SCMIO > CMIO > CMXNT > ISOTRK$. When a simulated lepton is reconstructed by several algorithms, the simulated event should have a none-zero weight of other lepton categories in addition to the one with the highest priority. The following value is the scale factor applied to the event when it is considered as lepton categories with lower priority.

$$\epsilon_\ell = SF^\ell \prod_{\ell' > \ell} (1 - SF^{\ell'}) \tag{4.7}$$

where ℓ' are all the lepton categories with the higher priority than the ℓ category.

$\not\!\!E_T$ Selection

$\not\!\!E_T$ is the signature of the presence of a neutrino. Thus, a $\not\!\!E_T$ cut is applied to select events with a neutrino. The definition and reconstruction algorithm is discussed in the Section 3.2.3.

The $\not\!\!E_T$ cut values applied are different for different lepton categories. For tight muons, which includes all muon events selected by muon-type triggers, we require $\not\!\!E_T > 10$GeV, since this type of events are less likely to be contaminated by multijet backgrounds. For CEM and EMC lepton categories, we require $\not\!\!E_T > 20$ GeV to remove as much multijet background as possible. For PHX, the cut is $\not\!\!E_T > 25$ GeV.

4.2.3 Jet Selection

In the single-top-quark s-channel measurement, we require exact two tight jets in each event. The jets used in the analysis are reconstructed using the JETCLU algorithm de-

scribed in Section 3.2.2. The definition of tight jets are

- jet $E_T > 20$ GeV, and jet $|\eta| < 2.0$

Further requirements are applied to both jets to improve both the event modelling and signal-to-background ratio. The jet requirements are listed below,

- The invariant mass of two jets, $M_{jj} > 30\text{GeV}/\text{c}^2$
- The leading jet E_T, $E_T^{jet1} > 30\text{GeV}$

For the Higgs boson search analysis, the three-jet events are also included.

Since in single-top-quark s-channel events, both jets originate from bottom quark (b jet), and because of the relatively long life time of B mesons, it is possible to distinguish a b jet from other types of jets. In this analysis, we used the HOBIT algorithm to tag the b jets.

HOBIT b-Jet Tagger

The Higgs-Optimized-B-Identification-Tagger (HOBIT) [50] was developed for the Higgs boson searches at the CDF experiment. In the previous analysis at CDF, several different b-jet taggers were employed. Those taggers are developed based on different principles.

SecVtx tagger [51] Because of the large momentum and relatively long decay time of the B mesons, B hadrons travel about 7 mm on average before they decay. This tagger identifies a b jet by looking for a displaced secondary vertex. This was the most widely-used tagger at CDF before the HOBIT tagger.

Soft lepton tagger [52] The branching ratio for the semileptonic decay of B meson is about 10% per lepton flavor. Also the leptons originating from the B meson usually come with lower p_T compared to the prompt leptons, so they are called soft leptons. The b jet can be identified by looking for a soft lepton inside a jet cone. At CDF, only soft muons are used in this algorithm because of the difficulty of identifying a electron or tau inside a jet cone.

RomaNN tagger [53] Unlike the previous two algorithms, this algorithm uses a multivariate technique. Thus, this tagger can use as many discriminating variables as possible to identify a b jet. And this tagger can achieve a higher efficiency with similar purity. The RomaNN tagger tries to reconstruct multiple vertices to improve discrimination power.

Bness tagger [54] There are about 20% of b jets that do not have enough tracks to reconstruct a secondary vertex inside a jet. The Bness tagger is developed to evaluate each track inside a jet to determined whether the track is b-jet like or not. The advantage of this algorithm is that it does not rely on secondary vertex reconstruction.

The HOBIT tagger was developed to address the weaknesses in the taggers discussed above. It is constructed as a multilayer perceptron neural network implemented in the TMVA package [55]. There are 25 input variables used by the HOBIT tagger, while 14 of them are also used as the input variables to the RomaNN tagger. The track-by-track Bness NN output values of the 10 tracks in each jet with the highest score are also used. Also, the number of tracks in each jet that can be tagged by Bness is used. The importance of each input variable is listed in Table 4.2.

The efficiency of the newly developed HOBIT tagger is evaluated on Higgs simulated events, and compared with previous taggers, as shown in Figure 4.1. From the plot, for a given purity, the improvements in the efficiency of HOBIT compared to the RomaNN or Bness is about 10%, and 15% when compared with SecVtx. We defined two operating points for the HOBIT tagger, 0.72 for the loose tag and 0.98 for the tight tag.

In order to use this tagger in the analysis, the efficiency difference between simulation and data must be corrected. This requires the measurement of the tagging efficiency in both simulation and data using the same method, as well as the mistag rate. In this analysis, the scale factors and uncertainties on the scale factors are evaluated in two independent ways, and then combined together.

The principle of the first method is to measure the b-tag scale factor and the mistag rate scale factor simultaneously in the W+3-jet sample and the W+1-jet sample. Since in the W+3-jet sample, the number of events with light flavor is too low to measure the

Input variable	Importance
Bness 1	0.63
Bness 0	0.57
Bness 2	0.52
SecVtx Loose	0.40
RomaVtx three-dimensional displacement significance	0.38
Bness 3	0.38
SecVtx Mass	0.37
RomaVtx pseudo-cτ	0.34
RomaVtx three-dimensional displacement	0.33
M_{inv} of HF-like tracks	0.29
Number of HF-like tracks	0.28
Bness 4	0.27
ptFrac	0.27
Bness 5	0.19
Bness 6	0.14
RomaVtx Mass	0.13
Number of track-by-track NN tracks	0.13
Total p_T of tracks	0.12
Number of Roma-selected tracks	0.11
Bness 7	0.10
Bness 8	0.08
Bness 9	0.06
Muon p_T to jet axis	0.05
Number of muons	0.04
Jet E_T	0.02

Table 4.2: The importance of the input variables used in the HOBIT b-jet tagger.

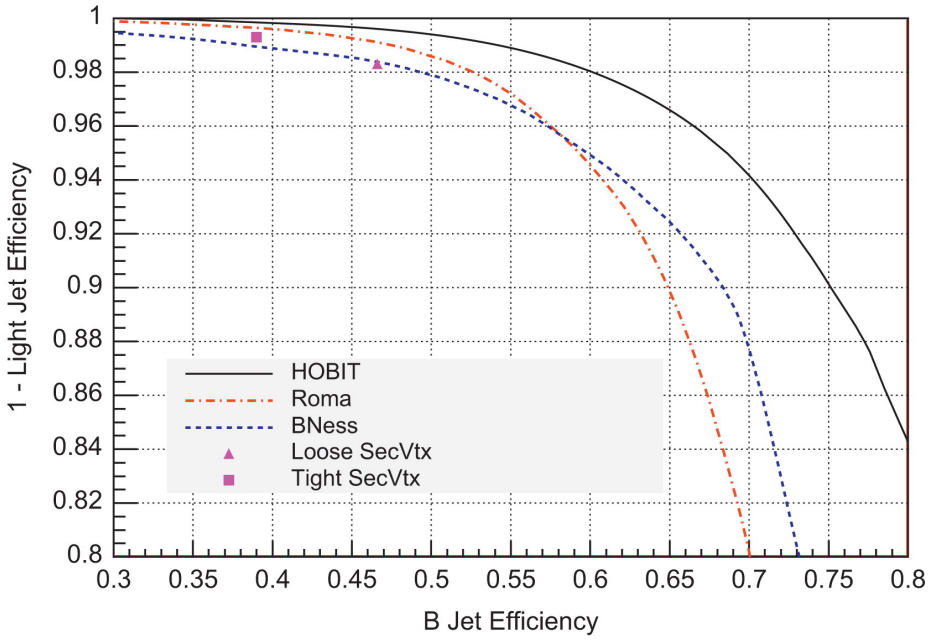

Figure 4.1: Comparison of the purity-efficiency trade-off for HOBIT and previous taggers.

mistag rate SF, the W+1-jet sample is added to provide extra constraints on the mistag rate SF. In this method, the tagging SFs are 0.997 ± 0.037 for loose tag and 0.917 ± 0.069 for tight tag. The mistag rate SFs are measured to be 1.391 ± 0.202 and 1.515 ± 0.291 respectively.

The second method is to measure the tagging efficiency and mistag rate on the jets which contains a soft electron, since only B hadrons have leptonic decay. In this method, events with back-to-back two jets are selected. And at least one of the two jets need to contain a soft electron. Photon conversions are also taken into account, as this process could also produce soft electrons. With the number of events of the tagged/pretag electron jets and the photon conversion jets, the tagging efficiency and mistag rate can be calculated. The tagging efficiency SFs obtained by this method are 0.986 ± 0.066 for loose tag and 0.949 ± 0.044 for tight tag, and the mistag rate SFs are 1.28 ± 0.17 and 1.42 ± 0.89 respectively.

By combining the SF values from the above two methods together, with the correlation of all the uncertainties considered, the final SFs used in the analysis are summarized in Table 4.3.

	Tagging efficiency SF	Mistag rate SF
Tight (0.98)	0.937 ± 0.037	1.492 ± 0.277
Loose (0.72)	0.993 ± 0.032	1.331 ± 0.130

Table 4.3: Combined results for the tagging efficiency scale factors and mistag rate scale factors.

The events that pass all the selection requirements but the b tagging one are classified as pretag events. Based on the pretag events, and using the HOBIT tagger, we constructed the following four tagging categories.

TT Both jets in the event have to be tight tagged.

TL One of the jets has to be tight tagged, while the other one is only loose tagged.

T Only one of the jets is tight tagged, while the other one is untagged.

LL Both jets are only loose tagged.

Chapter 5

Physics Process Modeling and Estimation

Both signal and background processes could pass all of the selection requirements discussed in the previous chapter. In order to study the process that we are interested in, both the event yield and the kinematic distributions of all the possible physics processes need to be well modeled.

In the first few sections of this chapter, the modeling of each background process and signal process is discussed. After all processes are well modeled, the estimation of event yields of each process is discussed.

5.1 Single Top Quark Processes

Single top quark processes are the processes in which the top quark is produced singly through electroweak interaction. There are three different channels in the single top quark production: s channel, t channel, and tW channel. The production cross section of these three channels are summarized in Table 5.1.

	Cross section (pb)
s channel	1.06 ± 0.06
t channel	2.12 ± 0.22
tW channel	0.22 ± 0.08

Table 5.1: Production cross section of three sub-channels for single top quark process [4].

The Feynman diagrams for the dominant channels at the Tevatron are shown in Figure 5.1. Since the t-channel events have the same final state as s channel, both channels

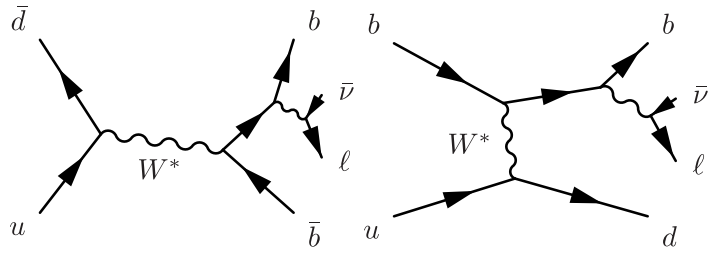

Figure 5.1: Feynman diagrams for the single top quark s (left) and t (right) channel.

need to be well modeled in order to distinguish the s channel from the t channel.

All single top quark processes are generated with POWHEG [39] up to next-to-next-to-leading-order (NNLO) accuracy in the strong coupling constant (α_s), and then showered by PYTHIA.

5.2 EWK Processes

Z+jets, diboson, top pair, and Higgs boson processes are grouped together into the EWK category and discussed in this section, because similar methods are used to model these processes. For the processes in the EWK category, the shapes, which is the distribution of kinematic variables, are predicted by Monte Carlo (MC) simulation and the normalizations, the total number of events, are predicted by MC or measurements.

5.2.1 Z+Jets

Z bosons produced through the Drell-Yan process can be generated in association with jets. For these $Z \rightarrow \ell\ell$ events, one of the leptons may not be identified if it escapes detection or fails one of the identification requirements. In that case, the Z+jets would meet the event selection requirements, and result in a background of this analysis. The Feynman diagram of this process is shown in Figure 5.2.

Z+jets processes are generated with ALPGEN at leading order, and then pass to PYTHIA for showering. In order to take the higher-order effects into consideration for the pre-

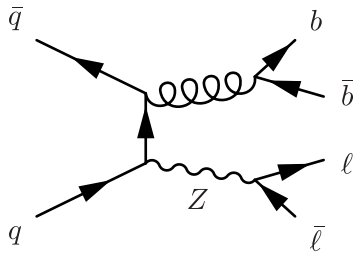

Figure 5.2: The Feynman diagram for the Z+jets process at leading order.

diction of the rate of this process, the predicted cross section is scaled according to the measurement of the on-shell Z+jets cross section [56].

5.2.2 Diboson

Diboson processes, including WW, WZ, and ZZ, can also contribute background events to this analysis. Certain decay channels of these processes have the same final state as single top quark s-channel as shown in the Feynman diagrams in Figure 5.3.

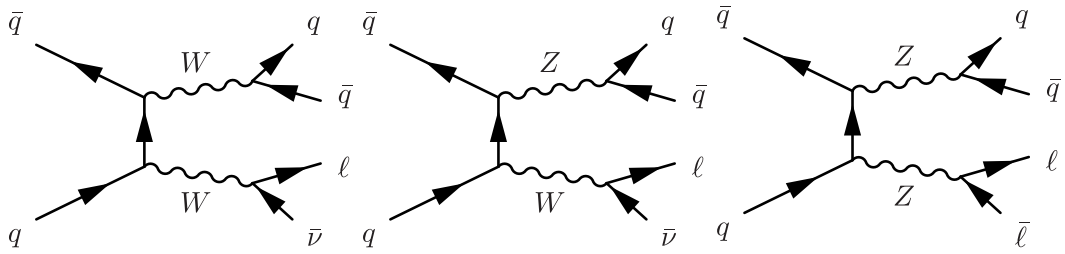

Figure 5.3: The Feynman diagrams for the WW, WZ, and ZZ process.

5.2.3 Top Pair

Top quarks can also be produced in pairs at the CDF experiment. When some of the final particles are misidentified, this process can pass the event selection requirements. According to Figure 5.4, this requires that one of the two W bosons escapes the CDF detector.

5.2.4 Higgs Boson

The Higgs boson was discovered at the LHC in 2012 and is therefore included as a background process for the single top quark analysis. As shown in the Figure 5.5, this process

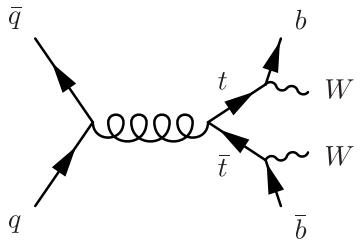

Figure 5.4: Feynman diagram for $t\bar{t}$ production.

has the exact same final state as the s-channel process.

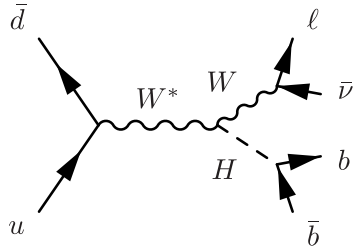

Figure 5.5: Feynman diagram for the Higgs boson associated production with W boson.

The diboson, $t\bar{t}$, and Higgs boson processes are all generated and showered using the PYTHIA event generator. The event yield for all of the processes are normalized to the theory prediction, as listed in Table 5.2.

	Cross section (pb)
WW	11.60 ± 0.70
WZ	3.46 ± 0.30
ZZ	1.51 ± 0.20
$t\bar{t}$	7.04 ± 0.44
Higgs	0.130 ± 0.009
Z+jets	787.4 ± 85.0

Table 5.2: Production cross sections for EWK processes.

5.3 W+Jets

Events resulting from direct W boson and two jets production (W+jets) contribute the dominant background in each of the b-tagging categories. This process is also the most difficult to model, because of the hundreds of possible Feynman diagrams that can produce a W+jets event. In this analysis, ALPGEN is used to calculate the matrix element (ME)

of each event at leading order (LO) because unlike PYTHIA it can calculate all color and spin correlations properly. PYTHIA is still used for parton showering (PS) of the events produced by ALPGEN.

Since there are many possible combinations of W plus jets, we generate more than a dozen MC samples to cover all of the possibilities:

- W plus 0, 1, 2, 3, ≥ 4 partons
- W+bb plus 0, 1, 2 partons
- W+cc plus 0, 1, 2 partons
- W+c plus 0, 1, 2, 3 partons

However, there is a double counting problem in this way of generating MC events. The heavy flavor partons can be generated from ALPGEN in the ME level. However, they can also be generated by the PS, for example from the splitting of a gluon. In order to avoid double counting the the same process from the ME and the PS, a cut is applied to both the PS and the ME level. A parton is defined to be matched to a jet if $\Delta R(parton, jet) < 0.4$ and $E_T^{jet} > 20$ GeV. For the events that the heavy-flavor quarks are generated by ME, we require the two partons not to be matched to the same jet. However, when the heavy-flavor quarks are generated by the PS, we require the two partons to be matched to the same jet. This is because the quarks coming from a gluon are more likely to be close to each other and these quarks are well simulated by the PS methods, while quarks generated by the ME are better simulated when they are far away from each other.

5.4 Multijet QCD

In the multijet QCD background, the events do not actually contain a W boson, but one of the jets is misidentified as a lepton. In order to pass event selection, the energy of one or more jets must also be mismeasured so that transverse energy is unbalanced and large $\not\!\!E_T$ is reconstructed in the event. The probability of these two effects to happen are so small that it is difficult to model this process by simulation. However, the cross section of

multijet events are so large that this process is not negligible in the analysis. Simulation isn't a viable option, so we use a data-driven method to predict this process.

The basic concept of the data-driven model is to select multijet events in which one jet has similar kinematic properties to a lepton. Since different leptons have significantly different kinematic distributions and trigger requirements, the multijet events are modeled using a different data sample for each lepton category. To ensure that the distribution of kinematics are similar to what would be selected, the lepton trigger requirements are applied to the events in the data-driven model.

5.4.1 Non-Isolated Muons

For all the reconstructed muons the isolation is required to be < 0.1. To model the multijet events related to muons, this requirement is flipped to be isolation > 0.2. With this requirement, the selected events still have similar kinematic distributions but is dominated by multijet backgrounds. This method is applied to CMUP, CMX, and EMC muon categories. The jet related to the non-isolated muon is removed from the jet multiplicity count.

5.4.2 Fake Electrons

The reversed isolation requirement is not applicable for the electrons, since this requirement is implemented at the trigger level to all triggered electrons. To model the multijet process for electrons a sample of fake electrons (anti-electron) is defined. The fake electrons use similar identification requirements as ordinary electrons, but are required to fail two out of five non-kinematic-related requirements. The five requirements are summarized in Table 5.3. With these requirements, the fake-electron events keep the same the kinematic property as the ordinary selected events.

5.5 Event Yield Estimation

With a model for each background process, the last step is to calculate the normalization of each process. This step is divided into two categories according to the methods used.

Anti-electron
$E^{Had}/E^{EM} < 0.055 + 0.0045E^{EM}$
$L_{shr} < 0.2$
$\chi^2_{CESstrip} < 10$
$\Delta z(CES, trk) < 3$ cm
$3.0 < q\Delta x(CES, trk) < 1.5$ cm

Table 5.3: The fake electron used in the multijet model for CEM has the same identification requirements as a CEM electron except it must fail two out of five requirements here.

5.5.1 Monte-Carlo-Based Background Estimation

For the processes that the production cross section is well known, the total event yield calculation is straight forward. The event yield of each process is calculated as

$$N = \epsilon\sigma\mathcal{L} \tag{5.1}$$

where ϵ is defined as the total efficiency, including the efficiencies for the detector system, trigger system, and all selection cuts. The scale factors for the lepton-identification algorithm and the b-tagging algorithm are also included. σ is the production cross section, and the numbers used for each process are listed in the Table 5.2. The last factor is the luminosity, $\mathcal{L}$, which is calculated for each lepton category, explained in Section 4.1.4.

The total efficiency ϵ can be decomposed into seven factors.

$$\epsilon = \epsilon_{tag} \cdot \epsilon^{MC} \cdot \epsilon_{BR} \cdot \epsilon_{trigger} \cdot \epsilon_{z0} \cdot SF_{lep} \cdot SF_{tag} \tag{5.2}$$

where the measurement of ϵ_{tag} is described in the Section 4.2.3. This efficiency number is parameterized as a function of five jet variables: jet E_T, jet η, the number of tracks in the jet, number of primary vertices in the event, and the z position of the jet. Thus, this value is calculated for each jet, and the scaling factor for correcting the b-tagging efficiency in the MC is applied so that it matches the measurement in data. The ϵ^{MC} is calculated from the number of MC events left after applying all event selection requirements versus the total number of events simulated, so this takes the detector acceptance and inefficiencies into account. The ϵ_{BR} is included, since in all MCs we forced the leptonic decay of the W boson, which has a probability of about 30%. The $\epsilon_{trigger}$ is calculated for each trigger we

used, and is discussed in detail in Section 4.1. A scaling factor for the lepton identification is also included to address the difference in the simulated events from the efficiencies measured in data. The ϵ_{z0} is applied because all simulated events are required to be within the range $|z| < 60.0$ cm. This number is measured from data and is the probability that a beam event is within the range.

5.5.2 W+Jets and Multijet Background Estimation

The method described in the previous section cannot be used to estimate the normalization of W+jets and multijet backgrounds. For the multijet background, it is because the normalization of a data-driven model must also be data driven. For the W+jets samples, the difficulty of calculating the normalization comes from several aspects. First of all, the number of diagrams to calculate the W+jets is enormous. The ALPGEN generator only calculates up to leading order, which underestimates the total cross section when compared with the next-to-leading-order calculation. Thus, both the normalization of multijet and W+jets sample has to be derived from data.

Pretag Region

The normalization of both samples are derived in a control region based on events that pass all event selection requirements but are not checked for the presence of b-tagged jets. This is referred to as the pretag region. The pretag control region is composed primarily of W+jets and QCD multijet events.

Since the multijet sample does not have a real neutrino, the reconstructed $\not\!\!E_T$ in multijet events is typically lower than what is reconstructed in a W+jets event. By removing the $\not\!\!E_T$ cut, a large number of multijet events are included. Now, it is possible to determine the normalization of both samples by fitting the $\not\!\!E_T$ distribution.

This $\not\!\!E_T$ fitting process is done in each lepton category separately because of the different detectors used in the lepton and trigger requirement. The fitting results for each lepton category are shown in Figure 5.6.

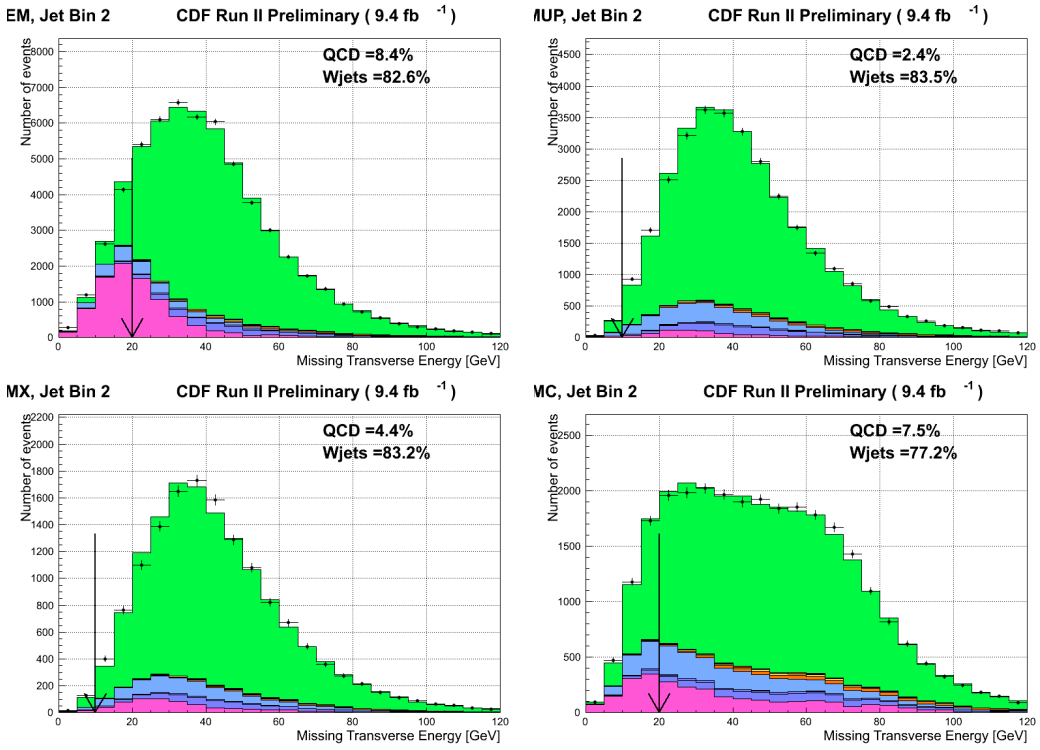

Figure 5.6: The $\not\!\!E_T$ fitting results for each lepton category. The multijet background is shown in pink and the W+jets is shown in green.

Tagged Region

After determining the normalization of both samples in the pretag region, the next step is to estimate the event yields in the tagged region. Different methods are employed for the multijet and the W+jets processes.

For multijet, in order to estimate the total event yield after apply the tagging requirement, the pretag multijet normalization is multiplied by a tag rate, as shown in the following equation,

$$N_{QCD}^{tag} = N_{QCD}^{pretag} \times \frac{N_{data}^{tag}}{N_{data}^{pretag}} \tag{5.3}$$

where the tag rate is derived by dividing the number of tagged data events by the number of pretag data events. This tag rate is calculated for each lepton and tagging category separately.

In order to calculate the normalization of W+jets sample in the tagged region, we separate the W+jets sample into two samples, W+heavy flavor jets and W+light flavor

jets, and use different methods to calculate the event yields for each. The W+heavy-flavor-jets sample includes W+bb, W+cc, and W+c, while the W+light-flavor-jets sample includes W boson associated production with light flavor quark jets or gluon jets.

For the W+heavy-flavor-jets sample, the following equation is used.

$$N^{tag}_{W+hf} = (N^{pretag} - N_{EWK} - N_{QCD}) \times f_{hf} \times K \times \epsilon_{tag} \tag{5.4}$$

In this equation, the number of events in the pretag region is first subtracted from the number of multijet events (N_{QCD}) in the pretag region and the total number of events of the MC estimated samples (N_{EWK}) to get the total number of events of all W+jets sample in the pretag region. Then, this number is multiplied with the heavy flavor fraction, f_{hf}; the K factor; and the tagging efficiency, ϵ_{tag}.

The heavy flavor fraction is defined as the number of W+heavy-flavor-jet events divided by total number of W+jet events. This number is estimated using the ALPGEN generator. The K factor is used to address the difference of heavy-flavor fraction observed in the ALPGEN sample and in the data. The K factor is measured in the W+1-jet sample, and calculated separately for W+bb, W+cc, and W+c sample. The value and uncertainty of K factor is summarized in Table 5.4. The tagging efficiency is the same number applied to the MC determined samples.

	K-factor
$W + bb$	1.40 ± 0.42
$W + cc$	1.40 ± 0.42
$W + c$	1.00 ± 0.33

Table 5.4: Summary for the K factor of heavy flavor fraction.

The W+light-flavor-jet sample is calculated by the following equation.

$$N^{tag}_{W+lf} = (N^{pretag} - N_{EWK} - N_{QCD} - N_{hf}) \times \epsilon_{Mistag} \tag{5.5}$$

Where the number of W+light-flavor-jet events is calculated by subtracting all of the other backgrounds from the total number events, include W+heavy flavor. Then, this pretag number is multiplied by the mistag rate ϵ_{Mistag} to get the total number of mistag W+light-

flavor events in the b-tagged sample. The mistag rate used here is calculated by averaging over all pretag data sample.

The shapes of W+heavy-flavor and W+light-flavor samples are derive by summing all tagged MC events weighted by the per event tagging efficiency and mistag rate.

5.5.3 Final Event Yield

By using the estimation method described in the previous sections, we obtained the final number of the event yield, as summarized in Table 5.5.

Category	TT	TL	T	LL
WW	1.7±0.4	13.2±2.7	184±23	24.8±3.9
WZ	17.8±2.2	21.2±2.0	52.7±5.4	9.9±0.9
ZZ	2.4±0.3	2.4±0.2	7.1±0.7	0.96±0.08
Z + jets	10.9±1.2	20.7±2.3	163±18	27.1±3.1
$t\bar{t}$	163±21	194±19	502±50	58.1±6.6
Higgs	6.1±0.6	6.4±0.4	10.3±0.7	1.7±0.2
Wbb	246±99	327±130	1166±468	109±44
Wcc	19.0±7.8	120±49	1158±467	164±67
W + Mistag	4.3±1.3	62±13	978±141	242±34
Multijet	29±12	47±19	281±112	45±18
t and Wt-channel	18.1±2.5	35.3±4.2	251±28	13.6±1.5
s-channel	54.5±6.7	61.2±5.6	109±10	17.8±2.1
Total Prediction	573±155	911±248	4860±1320	714±181
Observed	466	765	4620	718

Table 5.5: Summary of predicted event yields in backgrounds and signal processes in each tagging category, with systematic uncertainties included.

The stack plots of the invariant mass of the reconstructed top quark are shown in Figure 5.7 and Figure 5.8. In these plots, events are divided into two tagging categories and two lepton categories. From these plots, we observed nice agreements in all categories between the background model and the data.

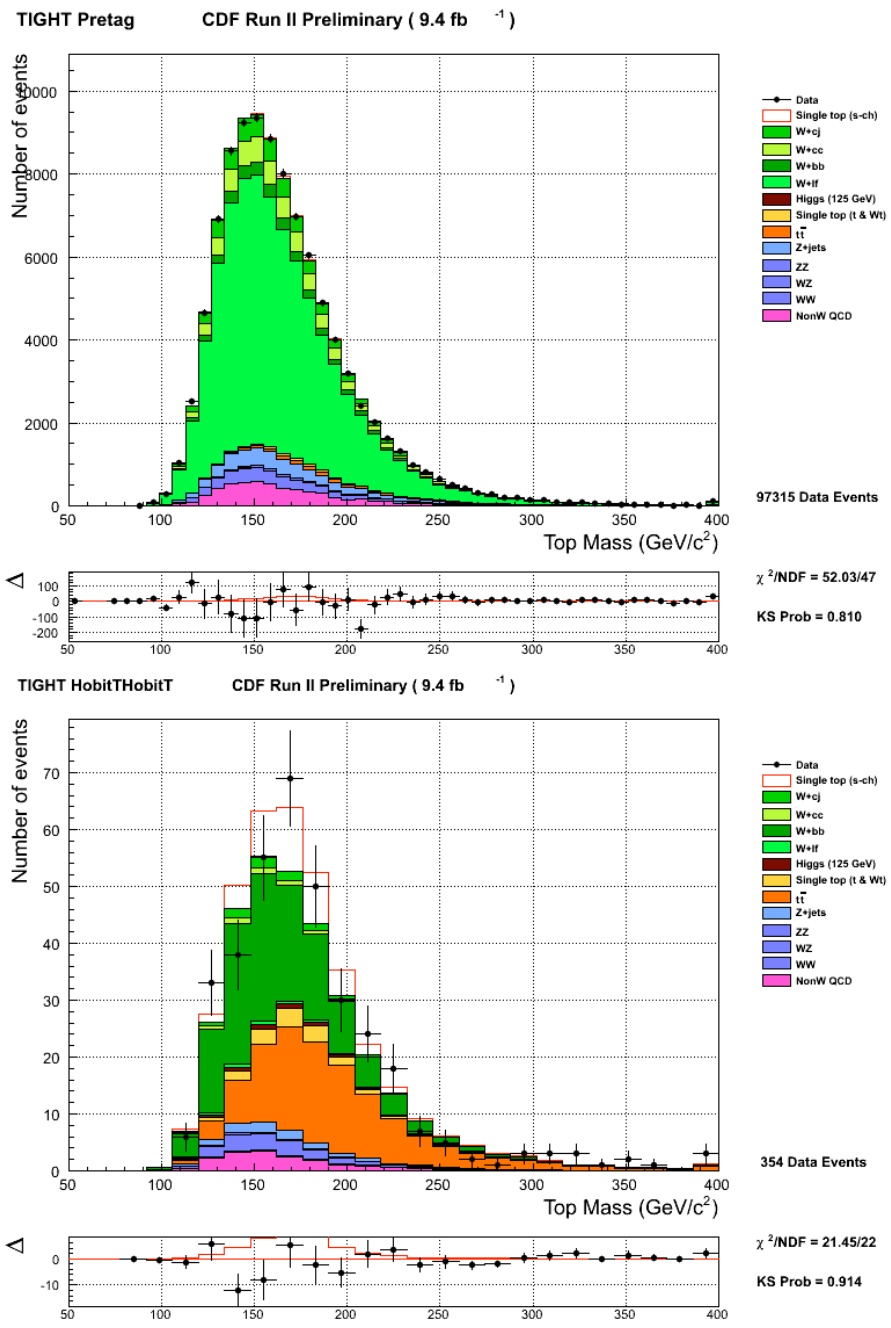

Figure 5.7: The distribution of the invariant mass of the reconstructed top quark in the pretag and TT region of tight leptons.

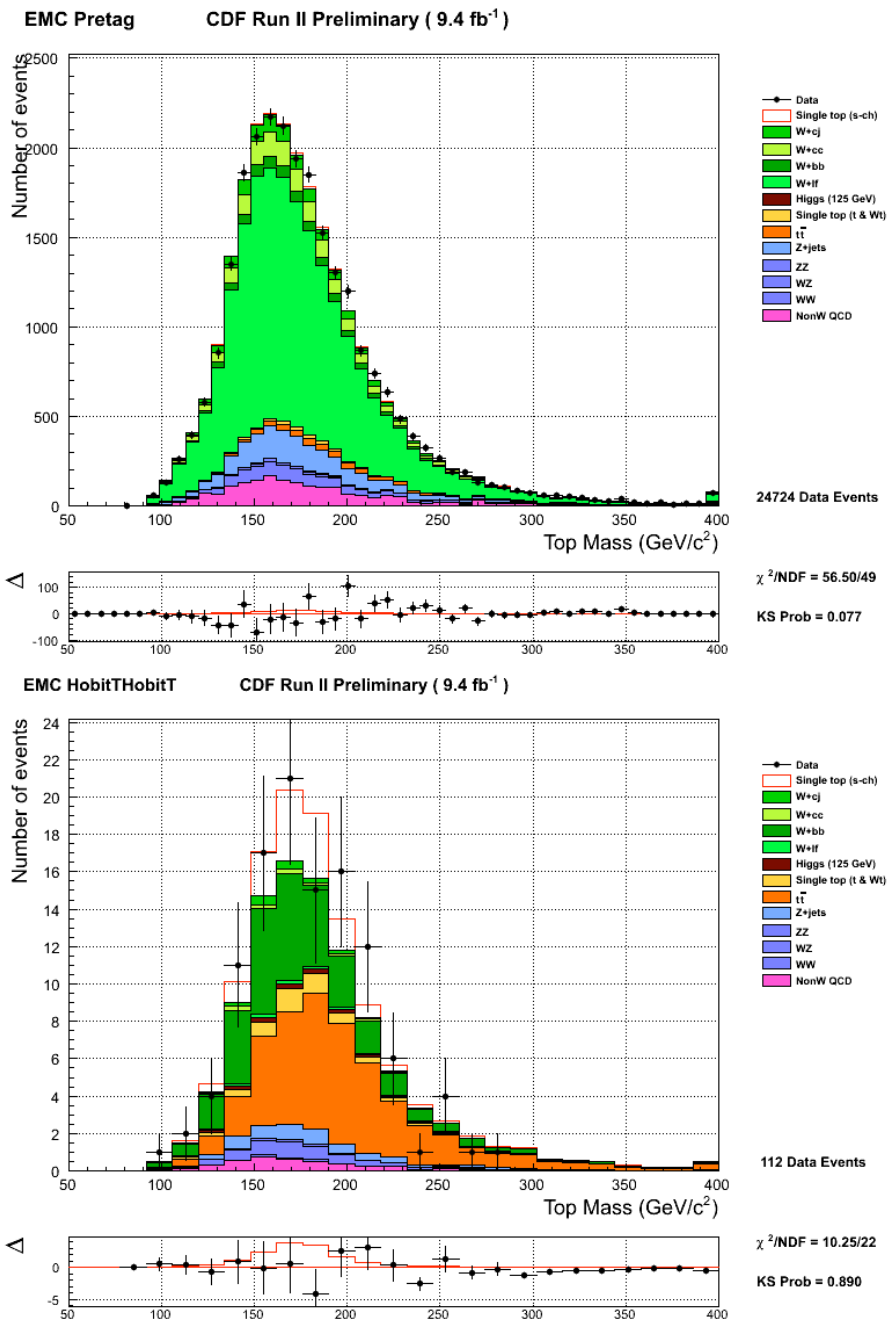

Figure 5.8: The distribution of the invariant mass of the reconstructed top quark in the pretag and TT region of extended muon category.

Chapter 6

Single Top Quark Analysis and Results

From the table of event yields in the previous chapter, we can see that the expected s-channel single top signal is even smaller than the estimated uncertainty on the total of all the backgrounds. Based on counting events in this sample it is impossible to draw any conclusion on the existence of the single top quark s-channel process.

In this analysis, we employ a multivariate analysis technique in order to train a final discriminant to separate the signal events from the background events as much as possible. The next step is to use the shape of the final discriminant to perform a binned likelihood fit, which also takes all systematic uncertainties into consideration. From the fitted results, we measured the s-channel single top quark production cross section. In the final step, the statistical significance of this result is evaluated.

6.1 Final Discriminant

The Toolkit for Multivariate Analysis (TMVA) [55] is used to develop the final discriminant to separate the signal process from the backgrounds. The TMVA package is integrated with the ROOT analysis package [57] and specifically designed to meet the needs of high-energy physics. The TMVA package provides many MVA technique options. In this analysis, we use the artificial neural network methods provided by TMVA.

6.1.1 Artificial Neural Network

The artificial neural network, generally speaking, is a set of simulated interconnected neurons. The whole set of neurons are able to produce a given output at the output neuron when given a set of input values. The response functions for each neuron, including intermediate neurons, are determined by the training process.

The structure of the neural network can be simplified by organizing neurons into layers, in which each neuron is only allowed to connect to the following layer, as demonstrated in Figure 6.1. This type of neural network is called the multilayer perceptron.

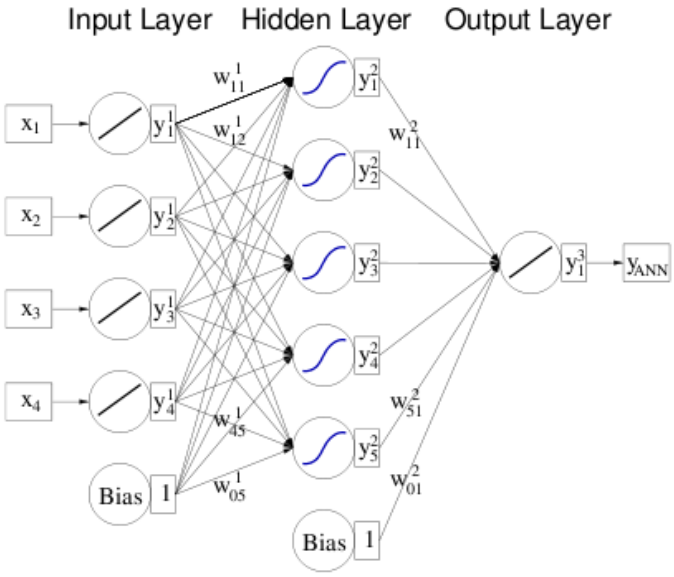

Figure 6.1: Multilayer perceptron with one hidden layer.

For the multilayer perceptron, the first layer is the input layer and the last one is the output layer. The response function for the whole neural network maps a set of input values to an output value. The whole function can be divided into two separate parts, the synapse function κ and the neuron activation function α. In this analysis these two functions have the following form:

$$\kappa : x^{l+1} = w^l_{0j} + \sum_{i=1}^{n} y^l_i w^l_{ij} \tag{6.1}$$

$$\alpha : y^l = \tanh x^l \tag{6.2}$$

Note that α has a nonlinear form so that the neural network can model a nonlinear relation between inputs and output.

The goal for the training process is to adjust the weight w_{ij} to achieve the maximum separation power for the final output variable y_{ANN}. The algorithm used here is a back-propagation algorithm.

For simplification, the output function of a neural network with only one hidden layer has the following form:

$$y_{ANN} = \sum_j^{n_h} y_j^2 w_{j1}^2 = \sum_j^{n_h} \tanh(\sum_i^{n_{var}} x_i w_{ij}^1) w_{j1}^2, \tag{6.3}$$

where n_h is the number of neurons in the hidden layer, and n_{var} is the number of input neurons. w_{ij} is the weight of synapses. Then, for each given set of w_{ij}, the error function $E(\mathbf{w})$ can be evaluated according to the following equation:

$$E(\mathbf{w}) = \sum_{a=1}^{N} \frac{1}{2}(y_{ANN,a} - \hat{y_a})^2. \tag{6.4}$$

This error is the sum of the errors of all training events, where a represents one event in the training set, N is the total number of events in the training set, and $\hat{y_a}$ is the desired output value of each training event.

In order to improve the performance of the neural network, which is equivalent to minimizing the total error $E(\mathbf{w})$, the steepest-gradient approach is used. In each iteration, the weight vector $\mathbf{w}$ is updated by moving a small distance η in the $\mathbf{w}$ space towards the direction where the $E(\mathbf{w})$ decreases most rapidly, as the following equation.

$$\mathbf{w}^{\rho+1} = \mathbf{w}^{\rho} - \eta \nabla_{\mathbf{w}} E \tag{6.5}$$

Achieving a good performance in the training sample may require increasing the complexity of it. The neural network complexity is proportional to the number of free parameters in it. When a neural network is too complex and there may be too little

information in the training set, the neural network is more likely to be over-trained. In order to avoid over-training, a Bayesian modification is implemented in the model. In this modification, an extra term is added to the error function.

$$\tilde{E}(\mathbf{w}) = E(\mathbf{w}) + \alpha|\mathbf{w}|^2 \tag{6.6}$$

In this way, the whole algorithm will avoid large weights, which are related to over-training.

This training algorithm has been extensively used at the CDF experiment, and has been proven to be robust.

6.1.2 Neural Network Training

In the training process, we developed a separate neural network optimized for each b-tag category, because the relative ratios between each background component are different in each category. In order to achieve the best optimized result in the training sample for each tagging category the fractions of each background are adjusted to be consistent with event yields shown in Table 5.5. The fractions used for each background sample are shown in Table 6.1.

Category	HTHT	HTHL	HT	HLHL
Signal (s-channel)	50%	50%	50%	50%
$t\bar{t}$	32.3%	11.4%	5.2%	4.1%
t-channel	1.6%	1.7%	2.1%	0.8%
Wbb	26.1%	20.7%	12.9%	8.3%
Wcc	1.1%	4.1%	7.0%	6.8%
Wcj	1.3%	4.7%	8.0%	7.8%
Wlf	0.4%	3.8%	10.4%	17.7%
Z+jets	1.1%	1.3%	1.8%	2.0%
WW	0.2%	0.8%	1.9%	1.8%
WZ	1.8%	1.3%	0.6%	0.7%
ZZ	0.2%	0.2%	0.1%	0.7%

Table 6.1: Composition of the training samples used to train the neural network for each tagging category.

In each b-tag category, events are further separated into tight leptons and the extended muon category (EMC). This is because the extended leptons are triggered by $\not\!\!E_T$-based

triggers. Thus, the kinematic distribution of the EMC events are different from those events that were triggered by a lepton-based trigger.

In order to achieve high separation power and good modeling, the input variables used in the neural network training need to be selected carefully.

The most powerful single variable is the reconstructed top quark mass, m^t. A good resolution of the reconstructed top quark mass will significantly improve the separation power of the final discriminant. In this analysis, a dedicated and optimized algorithm for the top quark reconstruction is developed, and discussed in the Section 3.2.4. Other variables that have some discrimination power are also used.

Moreover, in order to avoid any mismodeling of the trained neural network, only the variables that are well modeled are used. To be well-modeled means that the sum of predicted backgrounds is in agreement with measured data in various control and signal regions. The variables used in the neural network training are listed below and the modeling of the most powerful variable m^t is shown in Figure 5.7 and Figure 5.8.

- m^t: Reconstructed top quark invariant mass.
- m^{W^*}: Invariant mass of W^* boson.
- p_T^ℓ: p_T of the lepton.
- m_{jj}^{Corr}: Neural network b-jet energy corrected invariant mass of the two tight jets.
- H_T: the scalar sum of the transverse energies $H_T = \sum_{jets} E_T + p_T^\ell + \not{E}_T$. For this variable, we do not apply the neural network b-jet energy correction.
- $\cos\theta_{\ell j}$: where the $\theta_{\ell j}$ is angle between the lepton and the jet decayed from the top quark in the top quark rest frame.
- NN_{b-jet}: The neural network output from the top-quark b-jet selector.
- m_T^t: Reconstructed top quark transverse mass.

Most variables are used for NNs trained for both tight leptons and EMC. However, there are two exceptions. NN_{b-jet} is only used with NNs for the tight leptons, while m_T^t is only used with NNs for the EMC.

Overtraining could happen in the neural network training process. This happens when the neural network is optimized based on the fluctuations of the training data rather than the real underlying relations between variables. This can be checked by plotting the neural network distribution of the training sample and the test sample together. The overtraining checks for the NNs used in this analysis are shown in Figure 6.2. The agreement in the plots indicates that the neural networks are not highly tuned to the fluctuations in the training sample.

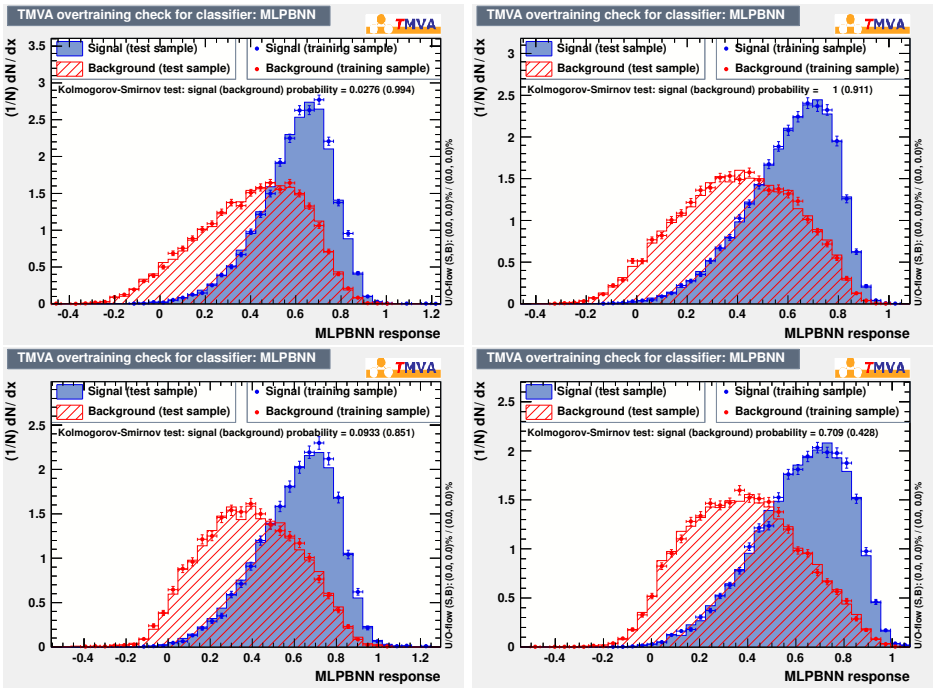

Figure 6.2: Overtraining check for each tagging category. From top left to bottom right are TT, TL, T, LL respectively.

The neural network output distributions for signal and different background processes are shown from Figure 6.3 to Figure 6.6. In these plots, the separation, as shown by the difference in the shape of the signal and backgrounds distributions, is clear.

Once the final discriminant is trained, we can construct the templates to be used for the final likelihood fit. The templates are the final discriminant output distributions of different processes in each tagging and lepton category. The stacked templates are shown in Figure 6.7 and Figure 6.8, with all lepton categories combined.

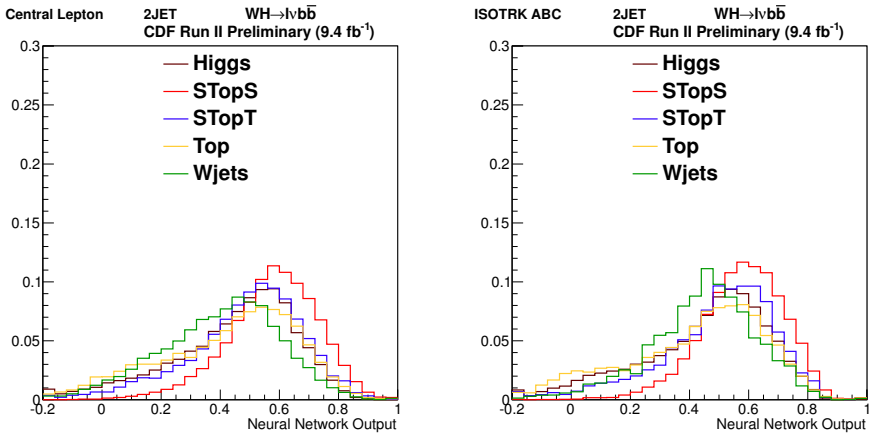

Figure 6.3: Comparison of the neural network output for signal and background events in the TT sample for TIGHT (left) and EMC (right). Signal and background histograms are each normalized to unit area.

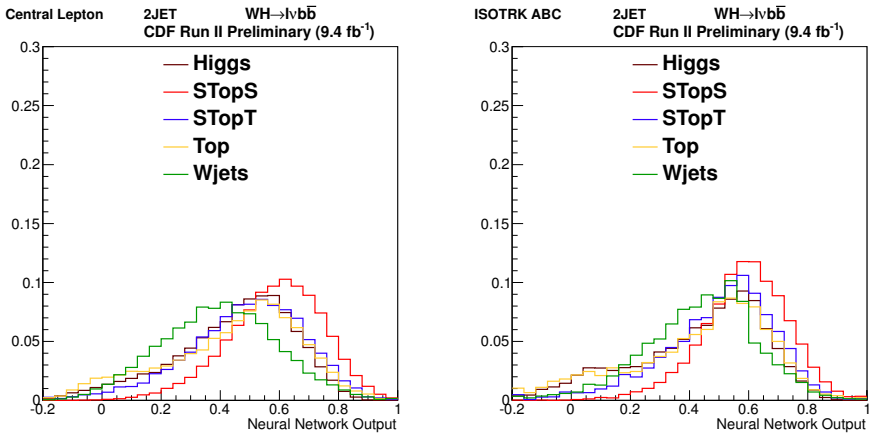

Figure 6.4: Comparison of the neural network output for signal and background events in the TL sample for TIGHT (left) and EMC (right). Signal and background histograms are each normalized to unit area.

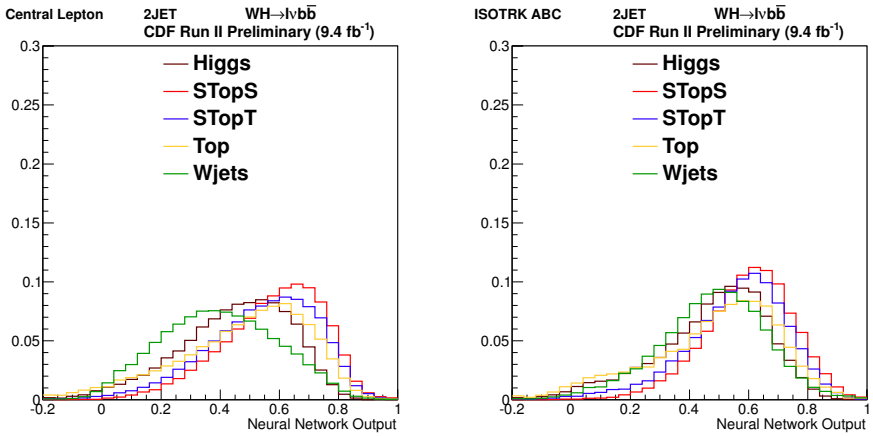

Figure 6.5: Comparison of the neural network output for signal and background events in the T sample for TIGHT (left) and EMC (right). Signal and background histograms are each normalized to unit area.

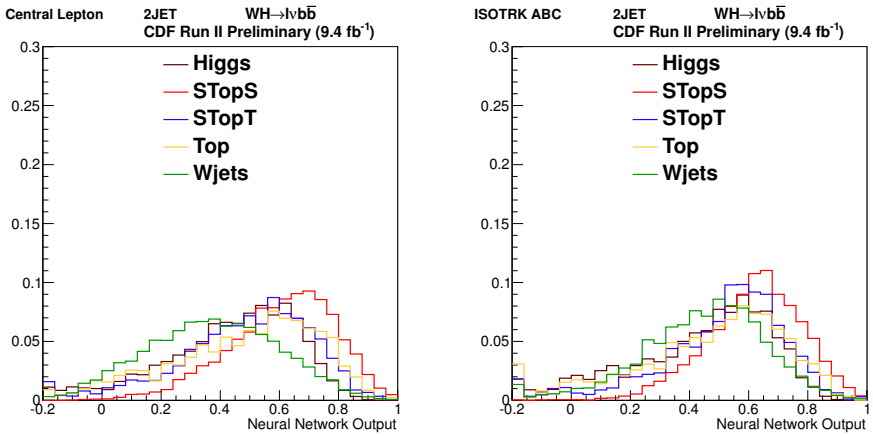

Figure 6.6: Comparison of the neural network output for signal and background events in the LL sample for TIGHT (left) and EMC (right). Signal and background histograms are each normalized to unit area.

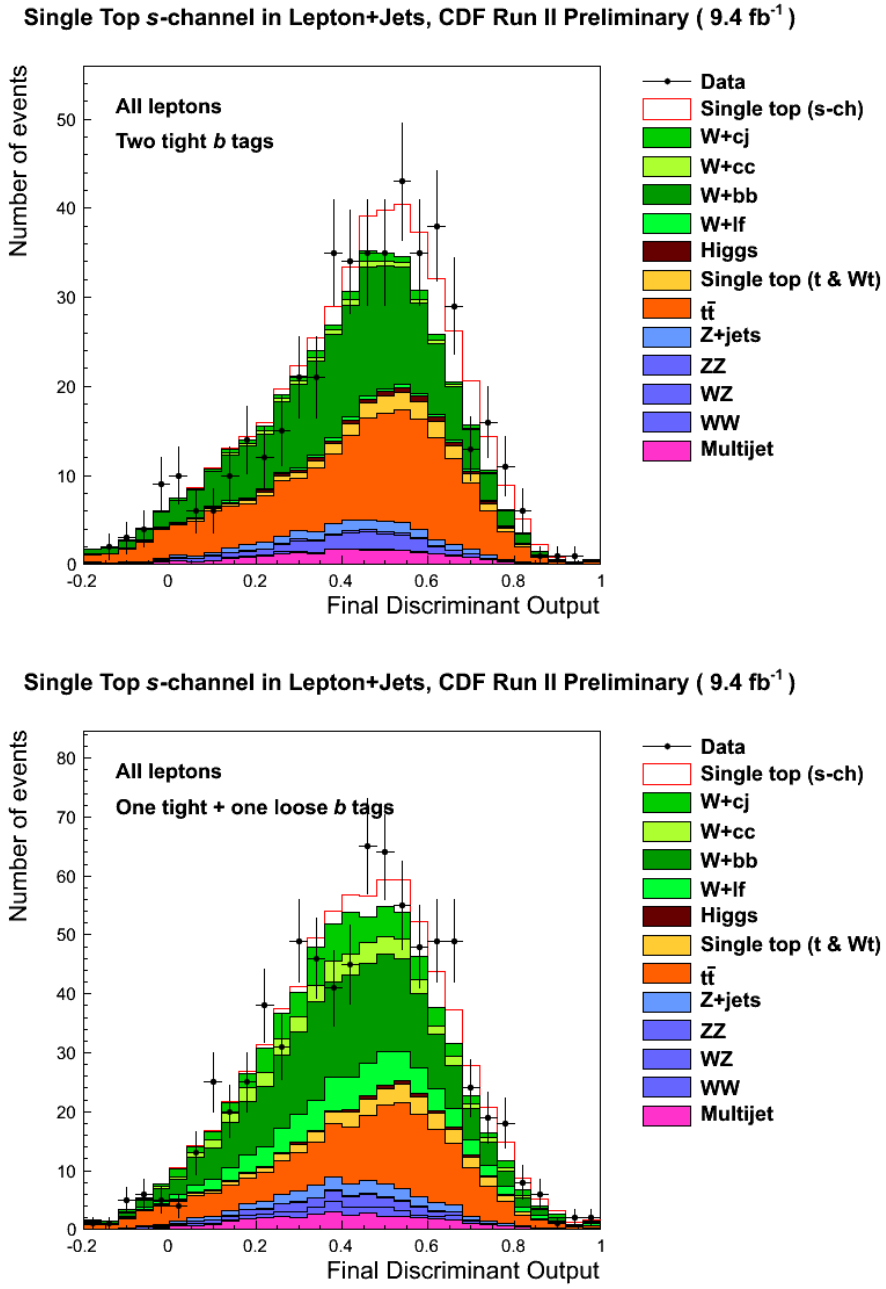

Figure 6.7: Final discriminant output distributions for TT and TL tagging category, with all leptons combined.

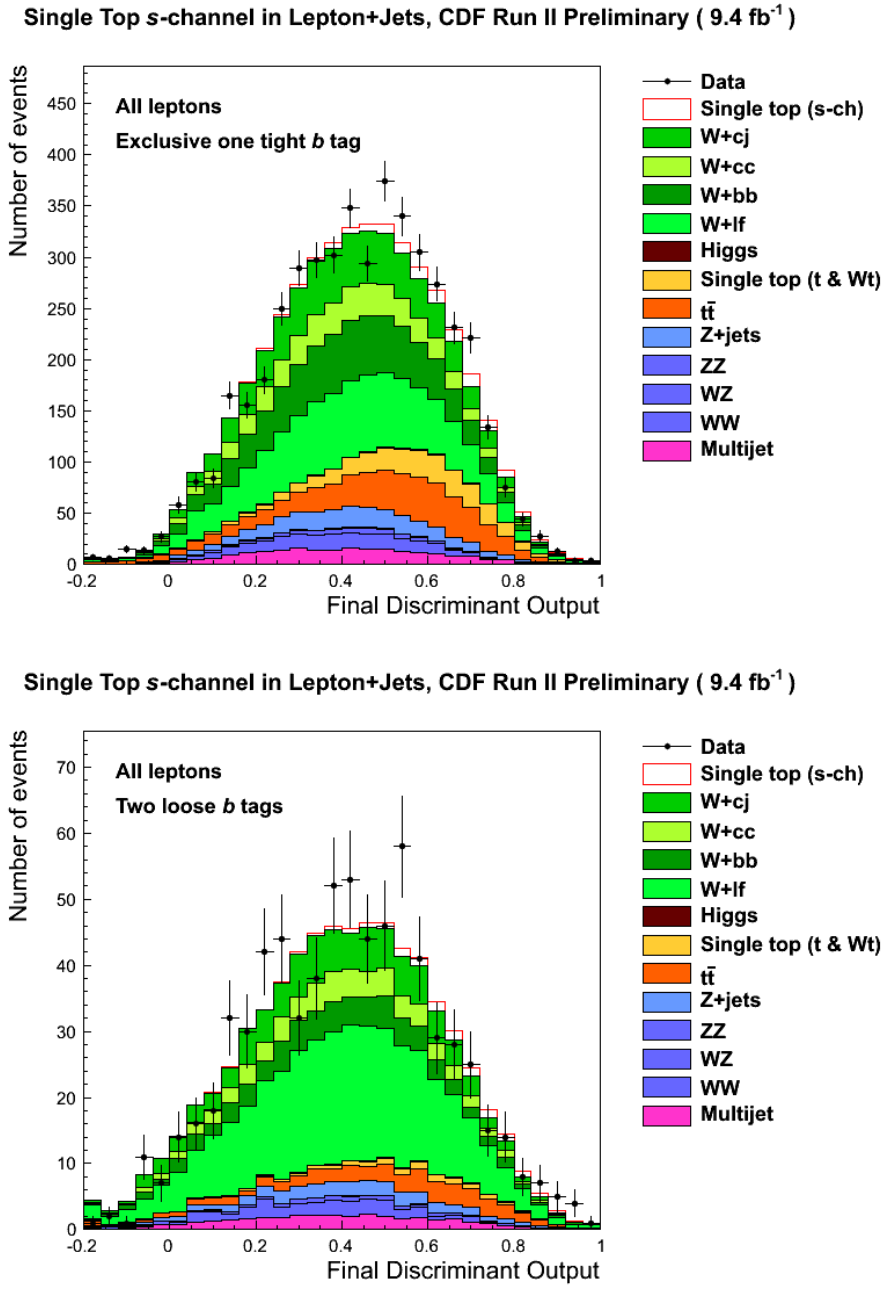

Figure 6.8: Final discriminant output distributions for T and LL tagging category, with all leptons combined.

6.2 Likelihood Function

With the templates of all processes generated, the final step of the analysis is to extract the production cross section. The Bayesian approach is used here to calculate the likelihood for varied signal production cross section with the given data. The posterior likelihood distribution is a function of the signal production cross section. From the distribution, the most probable cross section value is extracted, also the uncertainty on the cross section is estimated by finding the minimal interval which covers the 68% of the area of the probability density curve.

The binned likelihood function is constructed in the following steps. For a counting experiment with only one signal and one background process, the likelihood function is trivial.

$$L(\beta_s) = \frac{e^{-\mu}\mu^n}{n!}, \tag{6.7}$$

where $\mu = \beta_s N_s + N_b$, N_s is the expected number of signal events, N_b is the expected number of background events, and n is the number of events observed in each bin. β_s is a scaling factor for the standard model prediction. This function only includes the statistical fluctuation of a physical process, which follows the Poisson distribution.

When we take the distribution of a histogram and the multiple channels into consideration, the likelihood function becomes

$$L(\beta_s) = \prod_{i}^{Hist\ bins} \prod_{j} \frac{e^{-\mu_{i,j}} \mu_{i,j}^{n_{i,j}}}{n_{i,j}!} \tag{6.8}$$

Where $\mu_{i,j} = \beta_s N_s + \sum_q N_{b,q}$. This likelihood function also includes the situation where there are multiple background processes.

The last important step is to include the systematic uncertainties into the likelihood function. All the uncertainties are incorporated through nuisance parameters. We substitute the N_s and $N_{b,q}$ as a function of nuisance parameters δ_k.

$$N_s(\boldsymbol{\delta}) = N_s \prod_{k}^{Sys} (1 + \delta_k \epsilon_k) \tag{6.9}$$

$$N_{b,q}(\delta) = N_{b,q} \prod_{k}^{Sys} (1 + \delta_k \epsilon_{k,q}), \tag{6.10}$$

where ϵ_k is the relative ratio of the k-th systematic uncertainty to the central value. For rate uncertainties, this number is a flat value for all channels and bins. For shape uncertainties, this number is calculated bin-by-bin by comparing the shape systematic templates with the central one.

Since the distribution of all nuisance parameters should follow a Gaussian distribution and the final likelihood should be integrated over all nuisance parameters, one more factor should be added to the Equation 6.8,

$$L(\beta_s) = \int \prod_{i}^{Hist} \prod_{j}^{bins} \frac{e^{-\mu_{i,j}} \mu_{i,j}^{n_{i,j}}}{n_{i,j}!} \prod_{k}^{Sys} \mathrm{d}\delta_k \frac{e^{-\frac{\delta_k^2}{2}}}{\sqrt{2\pi}}. \tag{6.11}$$

This equation is the final likelihood function used in this analysis.

6.3 Systematic Uncertainties

Since this measurement relies heavily on the MCs to predict backgrounds and the final number of production cross section is derived from many physical quantities, the uncertainties of those numbers should be properly included. These kinds of uncertainties are called systematic uncertainties. They could affect either the total rate of the predicted process or the distribution of the final discriminant output of each process. All the uncertainties included in this analysis are summarized below.

Cross section The normalization of some of the processes are predicted by theoretical calculation of limited order or from previous measurement that are uncertain at some level. This kind of uncertainty only affects the rate of the given process. The value of the uncertainties used are listed in Table 5.2. Note that the cross section uncertainty on the single top quark *s*-channel process is not applied because it is the process that is to be measured.

***b*-tag scale factors** As discussed in Section 4.2.3, there is an uncertainty on the measured *b*-tagging scale factor. This uncertainty should be propagated to the final results.

The value of the uncertainty is listed in the Table 4.3. This uncertainty is applied to the processes which the normalization is predicted by theoretical calculation.

Luminosities The calculation of the absolute value of the production cross section relies on the measurement of the luminosity. We included 6% uncertainties [58] on the background processes which the normalization is predicted by theoretical calculation. This uncertainty is also applied on the single top quark *s*-channel.

Lepton acceptance This kind of uncertainty comes from two sources: the uncertainty on the trigger efficiency calculation and the uncertainty on the lepton identification scale factor. In the final cross section calculation, these two uncertainties are combined together quadratically for each lepton category, since they are uncorrelated with each other.

Multijet normalization This uncertainty is applied because the normalization of the multijet sample is derived from the $\not\!\!E_T$ fit and the data-driven model of the multijet background is not perfect.

***K*-factor uncertainties** This uncertainty is applied to the W+heavy-flavor-jet samples to cover the difference in the prediction of the heavy flavor fraction. The uncertainty applied on the W+bb/W+cc is considered to be uncorrelated with W+c because the first one is produced from strong interaction while the latter one is produced from electroweak interaction. The value applied is 30%.

***Z*+jets** The uncertainties we applied on this process is conservatively estimated to be 45% because the theoretical prediction of this process is poorly calculated.

Apart from the rate uncertainties listed above, we also included some shape uncertainties, as listed below.

Jet energy scale The imperfect estimation of the reconstructed jet energy can change both the rate and shape of the templates. To include this, systematic-uncertainty templates are produced in the same way as the central templates except that the jet energy is shifted up or down by 1 σ from the central value. In the final calculation,

both the rate and the shape of all MC processes are allowed to flow between the two systematics-uncertainty templates.

Factorization and renormalization scale The Q^2 is defined as the $M_W^2 + \sum_{partons} p_T^2$. This variable is used by the generator as the momentum scale of the hard interaction. However, this variable is not a physical observable, and choosing a different value could change the shape of the final templates. Thus, the W+jets templates are generated in the same way as the JES systematic templates with the Q^2 value doubled or halved.

Initial- and final-state radiation The estimation of the initial- and final-state radiation affects both the rate and shape in the same way as the JES systematic. In PYTHIA, ISR is estimated by "backwards evolution" and the uncertainty of it is constrained by studying the $Z/\gamma^* \to \ell\ell$ events [59]. The FSR effect in PYTHIA is tuned to LEP data. The ISR and FSR are considered to be 100% correlated, and the uncertainty is evaluated by doubling or halving the parameters affecting both effects at the same time. This systematic is only applied to the single top quark and $t\bar{t}$ processes.

Anti-electron model The anti-electron model we used in the analysis underestimated the number of events in the low $\not\!\!E_T$ range. This uncertainty is included to address this mismodeling of the anti-electron sample.

In order to avoid shape differences introduced by the statistical fluctuation, all shape systematic templates are smoothed (by using the average value of the 5-nearest bins) before they are used in the final calculation. Each systematic uncertainty is included in the likelihood function as one nuisances parameter to calculate the final result.

6.4 Cross Section Measurement

The final cross section measurement is calculated by extracting the β_s distribution from the likelihood function by marginalizing over all of the nuisance parameters. Since the β_s is the fraction of the standard model prediction, the final production cross section distribution is calculation by multiplying β_s with the standard model prediction.

The posterior probability density distribution is shown in Figure 6.9. Thus, the final

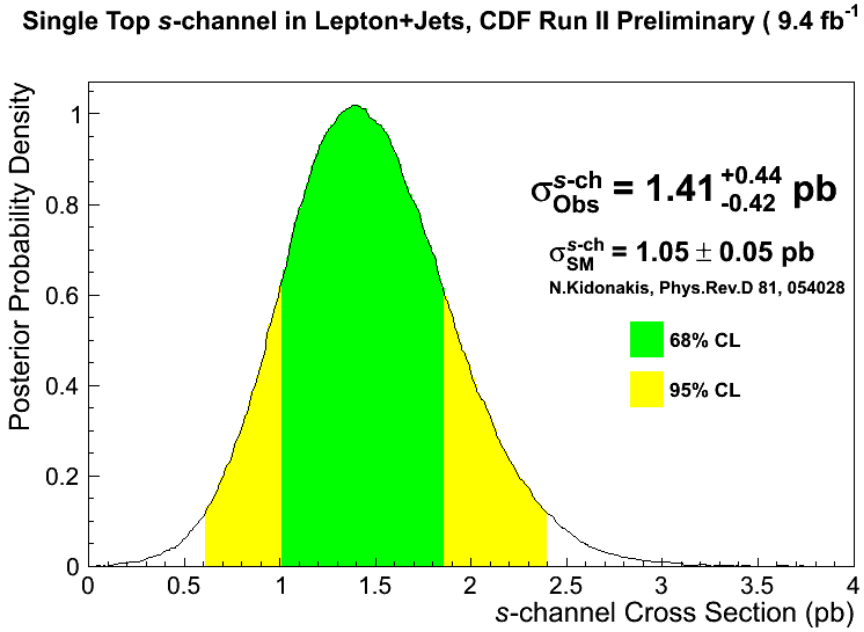

Figure 6.9: Posterior probability density distribution for the cross section measurement. The x-axis has been multiplied with the standard model prediction of the production cross section.

result is

$$\sigma_{s-ch} = 1.41^{+0.44}_{-0.42} \text{ pb}. \tag{6.12}$$

Several consistency checks are also performed to check the robustness of the analysis. We divide the data into several subsets, and measure the production cross section of the s-channel single top quark. The measured results are shown in the Figure 6.10, and the numbers are in good agreement with each other, with the result of whole data set, and with the theory prediction.

6.5 V_{tb} Measurement

Since the square of the CKM matrix element $|V_{tb}|^2$ is proportional to σ_{s-ch}, we can also measure the V_{tb} value from the posterior probability density distribution.

Since the V_{tb} calculation depends on the single top quark cross section, the uncertainty on the standard model prediction of all single top quark channels is included. Moreover,

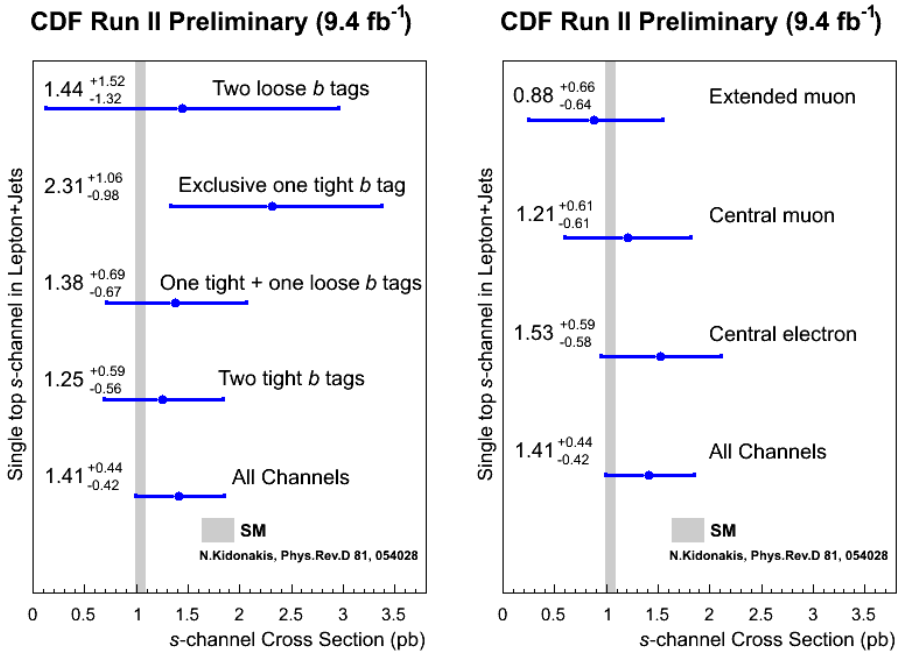

Figure 6.10: Measurements of the production cross section of s-channel single top quark in each tagging and lepton category.

since V_{tb} affects the coupling of both the s- and t-channel, both channels are treated as the signal process in the V_{tb} measurement. In the measurement, the ratio of number of events between s and t channel is fixed to the standard model prediction.

In this analysis, we included the extra systematic uncertainties on the standard model prediction. We also treated the s- and t-channel together as the signal, and fix the ratio between them to be agree with standard model prediction. Since $|V_{tb}|^2$ is limited between zero and one, the credibility interval is calculated starting from one. The result is limited to be

$$|V_{tb}| > 0.86 \tag{6.13}$$

at 95% credibility level, as shown in Figure 6.11.

6.6 Statistical Significance Evaluation

To compute the significance of the measurement, we need to calculate how likely it is that this result is due to fluctuations of the background-only hypothesis.

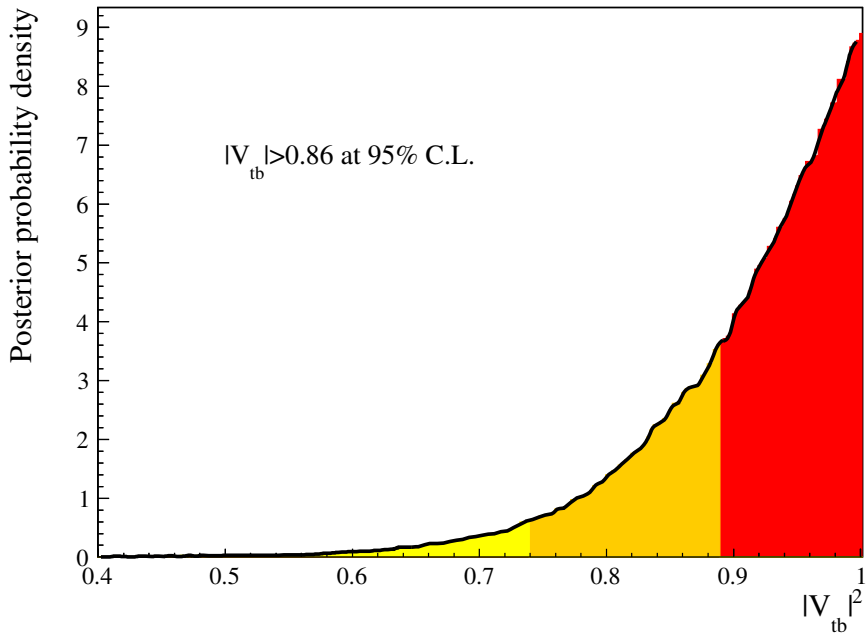

Figure 6.11: The likelihood distribution for $|V_{tb}|^2$ with 68% and 95% credibility interval set.

To measure the significance, we generated many pseudo-experiments (PE) with background only processes. These PEs are generated by varying the number of events in each bin of the templates randomly with extra requirements so that they follow the Gaussian distribution expected from all systematic uncertainties. Then, the measurement is performed on the pseudo-data with the background-plus-signal hypothesis. The distribution of PE outcomes is shown in Figure 6.12.

The final results is that the observed p-value is 0.000055. This can be interpreted as evidence for the single top quark s-channel process with a significance of 3.8 σ.

PEs including the signal process are also generated, as shown as the blue ones in the Figure 6.12. The measured results of these PEs represent the distributions of the expected cross section measurement outcomes with the analysis technique we used. Also, the p-value of the most probable expected cross section, the expected p-value, can be used to representing the expected sensitivity of the analysis. For this measurement, the expected p-value is 0.0019, and this corresponds to an expected significance of 2.9 standard deviations.

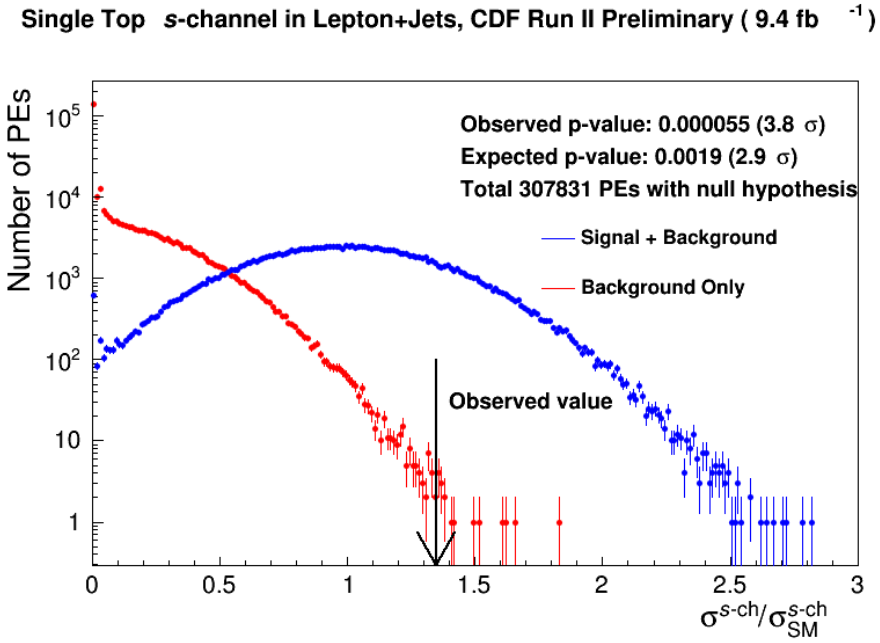

Figure 6.12: The possible outcome of pseudo-experiments (PE) measured with background plus signal hypothesis. The blue ones are PEs generated with background plus signal processes, while the red ones are generated with only background processes.

6.7 Combinations

This result is also combined with other measurements at the Tevatron to improve the sensitivity of the measurement.

6.7.1 CDF Combination

There is another measurement on this process at the CDF experiment which uses the $\not\!\!E_T$+jets final state. We combine these two measurements together to generate the combined CDF result [60].

In the $\not\!\!E_T$+jets analysis, events with leptons are vetoed to keep the data set orthogonal to the measurement described in this thesis. The $\not\!\!E_T$+jets final state is included because the lepton from the decay of the W boson could escape detection.

The combined cross section measurement is measured to be

$$\sigma_{s-ch} = 1.38^{+0.38}_{-0.37}\ \text{pb} \tag{6.14}$$

as shown in Figure 6.13.

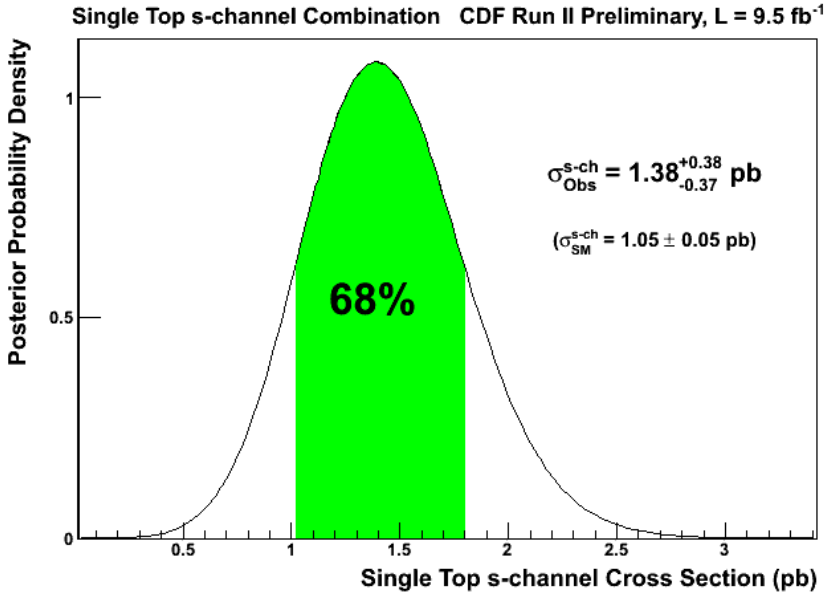

Figure 6.13: Posterior probability density distribution for the cross section measurement. The x-axis has been multiplied with the standard model prediction of the production cross section.

Similarly, we also measured the significance of this measurement. After combination, the observed significance increased to 4.3 standard deviations, as shown in the Figure 6.14.

6.7.2 Tevatron Combination

The D0 experiment previously reported evidence for the *s*-channel single top quark process [17]. In order to improve the sensitivity of the signal process, we combine the analyses of the CDF and D0 experiments together [61].

The production cross section is measured through the posterior probability density based on the combined likelihood. From the distribution, the measured cross section is $1.29^{+0.26}_{-0.24}$ pb, as shown in Figure 6.15.

In order to check the consistency of the combination, the combined cross section measurement is compared with the measurement in each independent channel, as shown in the Figure 6.16. The NNLO theory prediction is also drawn on the plot.

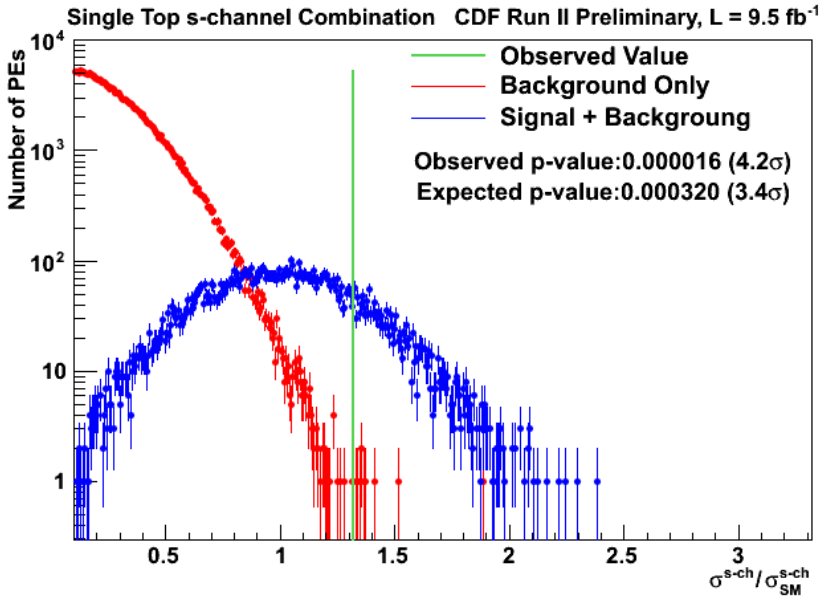

Figure 6.14: The possible outcome of pseudo-experiments (PE) measured with background plus signal hypothesis. The blue ones are PEs generated with background plus signal processes, while the red ones are generated with only background processes.

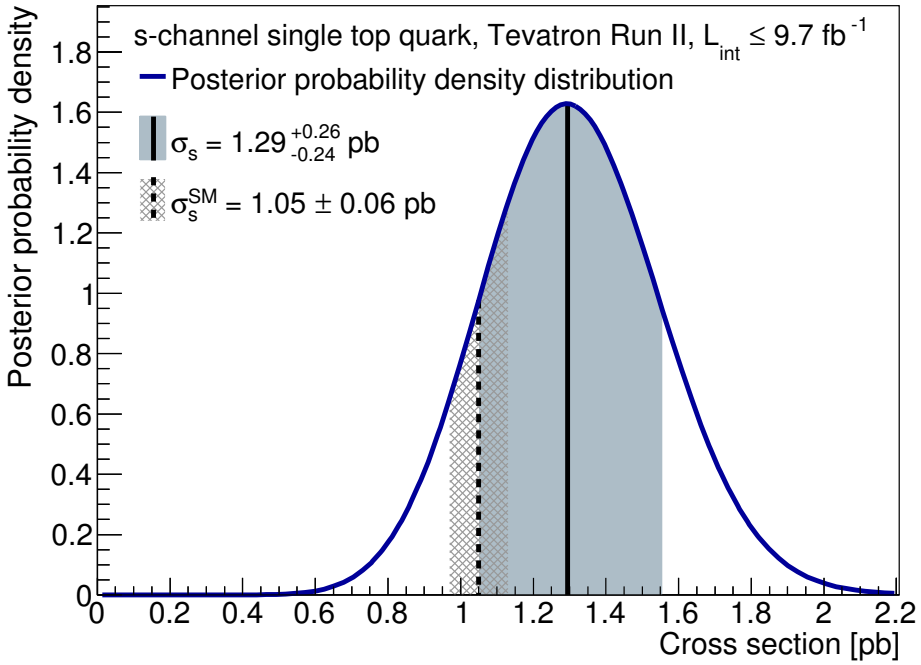

Figure 6.15: The posterior probability density distribution as a function of the production cross section.

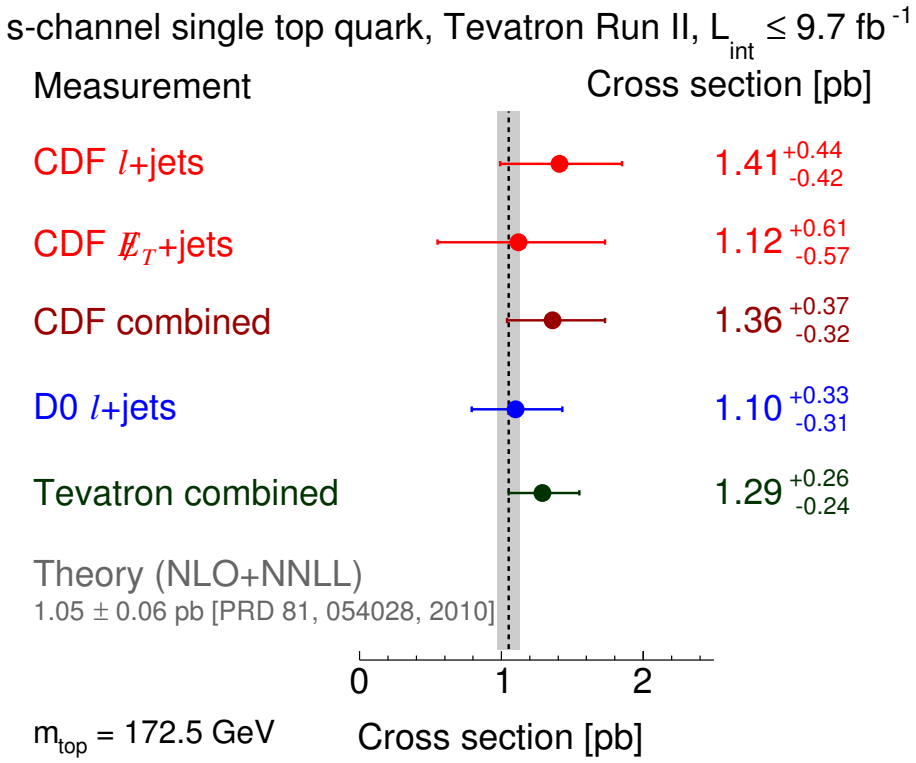

Figure 6.16: The summary of the measured cross section of each channel and the final combined result.

The p-value is used to estimate the significance of the signal process, and it is estimated through an asymptotic log-likelihood ratio approach, including systematic uncertainties, as shown in Figure 6.17. The observed p-value is 1.8×10^{-10}, corresponding to the significance of 6.3 standard deviation.

In summary, for the first time, we observed the *s*-channel single top quark process at the Tevatron. The measured *s*-channel single top quark production cross section is $1.29^{+0.26}_{-0.24}$ pb.

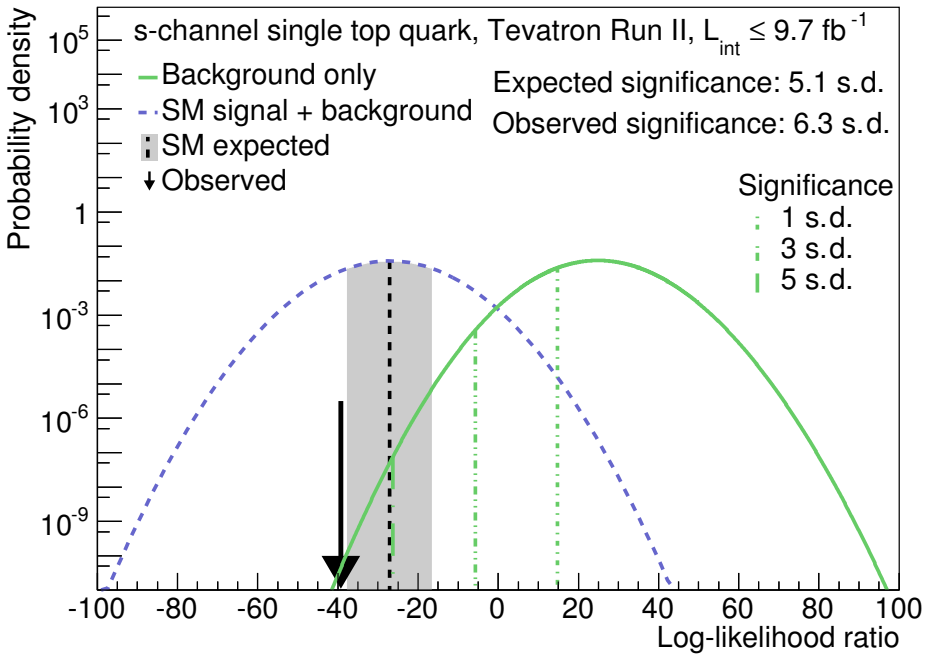

Figure 6.17: Log likelihood ratio for the background-only and signal-plus-background hypotheses from the combined measurement.

Chapter 7

Higgs Boson Analysis and Results

The Higgs boson, the last missing piece of the standard model, was discovered by the CMS and ATLAS experiments in 2012 [19, 20]. However, the experiments at the Tevatron also made important contributions to the search for the Higgs boson.

As discussed in the Chapter 1, the Higgs boson can decay into either fermions or bosons, such as, $H \to \gamma\gamma$, $H \to ZZ$, $H \to WW$, $H \to \tau\tau$, and $H \to bb$. As shown in Figure 7.1, the experiments at the LHC are sensitive to almost all of them. However, for the $H \to bb$ channel, the Tevatron has similar sensitivity as the CMS experiment. Thus, the contributions from the Tevatron can be an important supplement to the results from the LHC.

In this chapter, first of all, we discuss the search for the WH process at CDF, of which the tools serve as the foundation for the single top quark s-channel cross section measurement already discussed. In the following sections, the combination of the $H \to bb$ searches, and also the combination with analyses of all other decay modes at both CDF and the Tevatron are discussed. Evidence of both the presence of the $H \to bb$ decay mode and the standard model Higgs boson are found when the searches from the CDF and D0 experiments are combined.

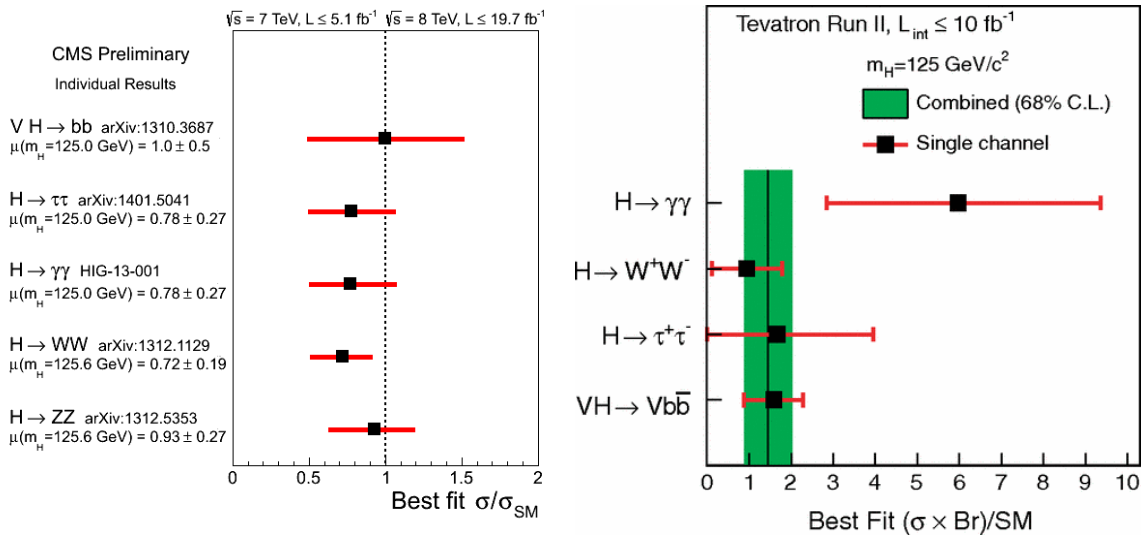

Figure 7.1: Tests of the Higgs boson signal strength of different decay modes. The plot on the left shows the CMS experiment results, on the right shows the Tevatron results.

7.1 $WH \to \ell\nu bb$ at CDF

The most sensitive search channel for the Higgs boson in the low mass range ($m_H < 130$ GeV/c^2) at the Tevatron is the Higgs boson associated production with a W boson, as shown in Figure 7.2. The search for the WH process is discussed in the Ref [62].

As discussed in the previous chapters, this channel has the same final state as the single top quark s-channel process, so this search shares many common analysis techniques with the measurement of the single top quark cross section. The common list includes event selection, b-jet tagging algorithm, background modeling, systematic-uncertainty evaluation, and etc.

There are also some differences between the two analyses. One important difference is that a few extra event categories are included in the Higgs boson search. We added the PHX lepton, the single loose b-tag channel, and events with three jets. Secondly, because of the different signatures between the two physics processes, different input variables for the final discriminant are used. In the Higgs boson search the most important input variable is the invariant mass of the two jets, which is expected to be the jets originating from the Higgs boson decay. The Higgs boson signal can be reconstructed as an enhancement (broad peak) in the invariant mass distribution of the two jets.

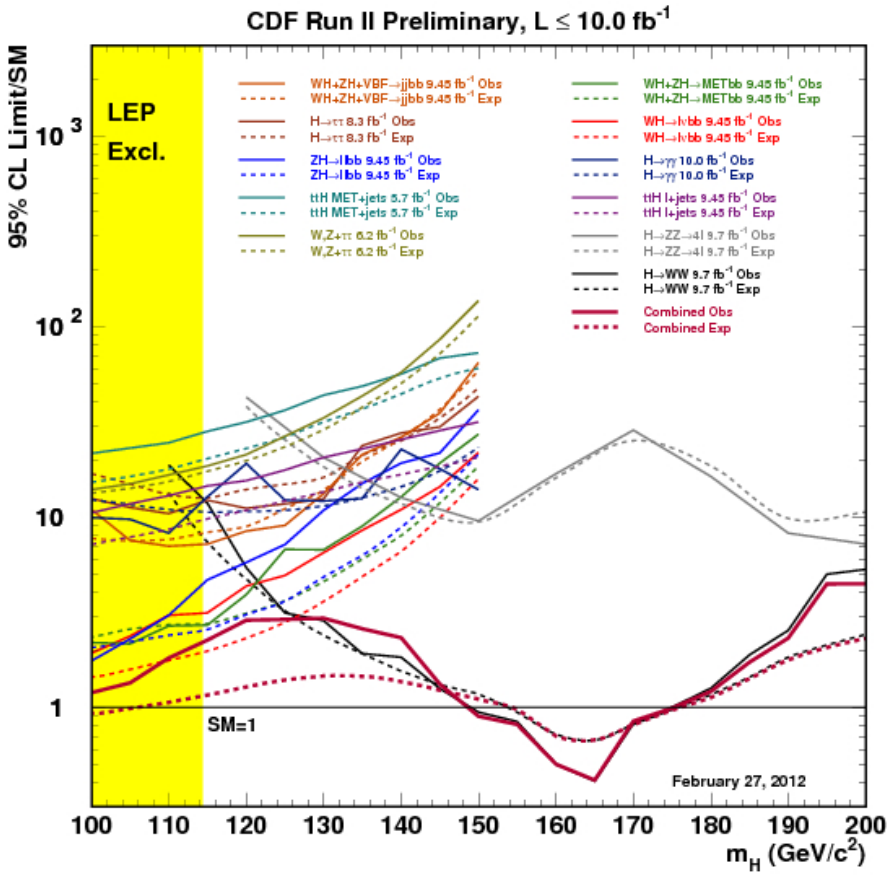

Figure 7.2: Comparison of both observed and expected limits of different Higgs final states at the CDF experiment. The red line represents the *WH* process, which is the most sensitive channel in the low mass range.

Since at the time this work was conducted the Higgs boson mass was not yet determined, we test the Higgs boson hypothesis with different mass assumptions. The observed and expected limits are shown in Figure 7.3. In the plot we see a broad excess

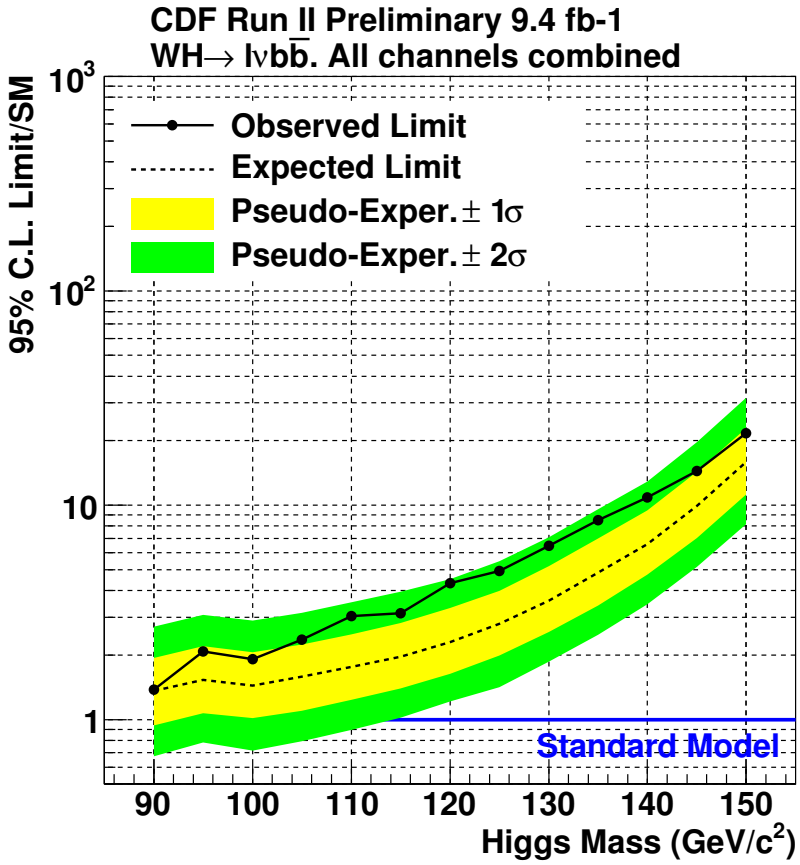

Figure 7.3: Observed and Expected upper limits of the 95% credibility level on WH production cross section times $b\bar{b}$ branching ratio as a function of Higgs boson mass. Combined with all lepton and tagging categories.

over the full mass range. Actually, this excess is consistent with the presence of a standard model Higgs boson in the low mass range and the existence of the broad excess is because of the limited jet energy resolution at the CDF experiment.

7.2 Higgs Boson Coupling to Bottom Quarks

There are other targeted analysis at the Tevatron to test the Higgs-bottom-quark coupling. Besides the WH channel, we also use the $ZH \to \ell\ell bb$ [63] and the $VH \to \not\!\!E_T bb$ [64]

channel. We combined them together to increase the sensitivity to the $H \to bb$ coupling. The combinations discussed in this section covers the Higgs boson mass assumption from 90-150 GeV/c^2.

The combination is first carried out at the CDF experiment [65]. With the help from other channels, the sensitivity to the presence of Higgs boson is increased, as shown in the Figure 7.4. However, no conclusive statement regarding the existence of a Higgs boson can be made from these data alone.

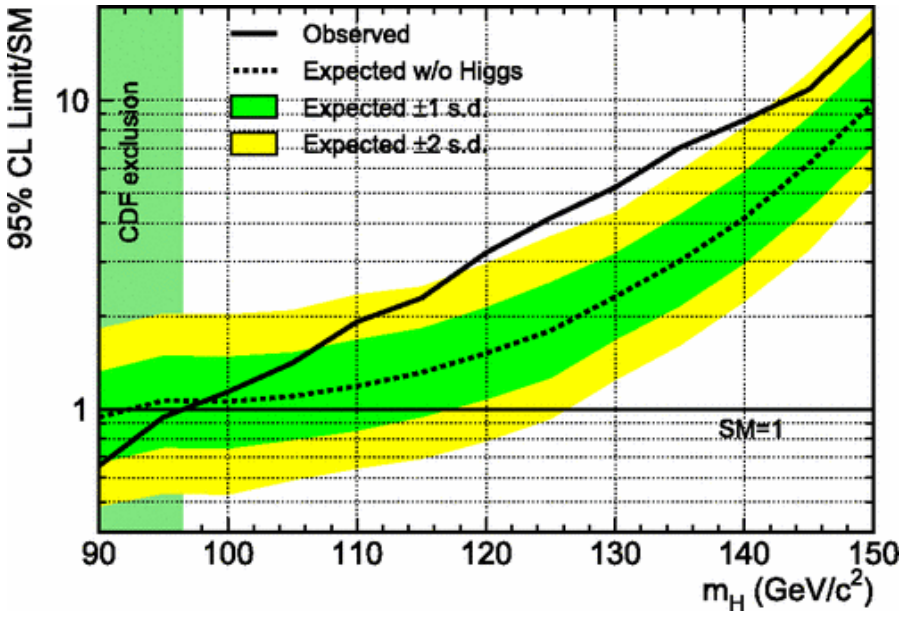

Figure 7.4: The expected and observed upper limit of the 95% credibility level on the Higgs boson production as a function of Higgs boson mass for the combined result from the CDF experiment.

The search for the $H \to bb$ at CDF is also combined with the same search at D0 to further improve the sensitivity [21]. The limit plot, similar to the CDF combination, is shown in Figure 7.5. The two limit plots look similar to each other. However, there are two differences that demonstrate the higher sensitivity of the Tevatron combination. Firstly, for the CDF combination, the Higgs boson is excluded at 95% credibility level for a Higgs mass smaller than 96 GeV/c^2. This exclusion goes up to 106 GeV/c^2 when the CDF and D0 results are combined. Secondly, the excess of the observed credibility limit is higher in the Tevatron combination.

We calculate the p-value of the Tevatron combination, as shown in the Figure 7.6. The

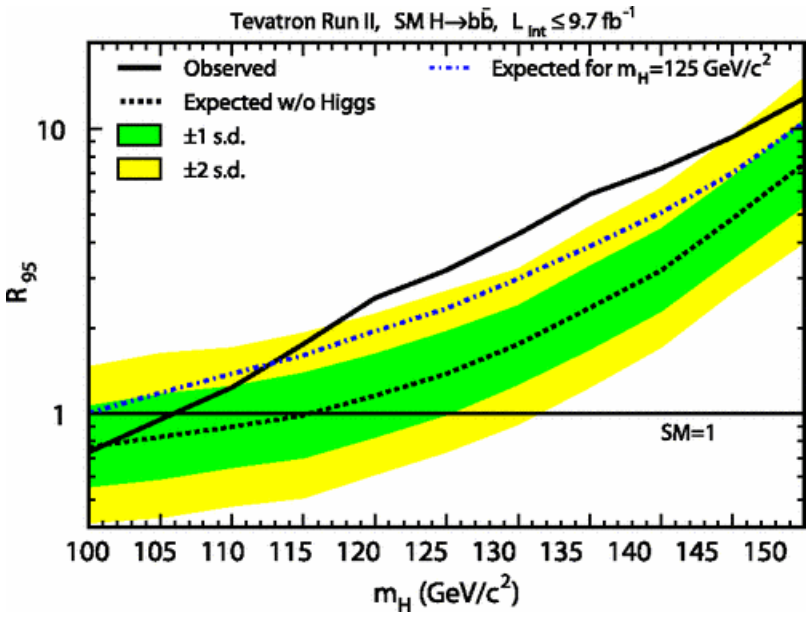

Figure 7.5: The expected and observed upper limit of the 95% credibility level on the Higgs boson production as a function of Higgs boson mass for the combined results from the CDF and D0 experiments.

p-value is interpreted as the probability to obtain the observed result with the background-only hypothesis.

The Look-Elsewhere Effect (LEE) [66] accounts for fluctuations of the local p-value over the mass range tested. Correcting for the LEE effect, the significance for the global excess is 3.1 standard deviations. Thus, we interpret this result as evidence of the presence of a particle that is produced in association with a W or Z boson and decays to a bottom-antibottom quark pair. The dip in the p-value plot is from 120 to 140 GeV/c^2, and the width of the dip is consistent with the production of the SM Higgs boson within this mass range.

7.3 Standard Model Higgs Boson

We also combine the $H \to bb$ decay mode with other channels to test the full standard model Higgs boson theory. The combined result at the CDF experiment is reported in the Ref. [67], and the Tevatron combination is discussed in the Ref. [68]. In the combinations, the Higgs boson mass hypotheses from 90-200 GeV/c^2 is covered.

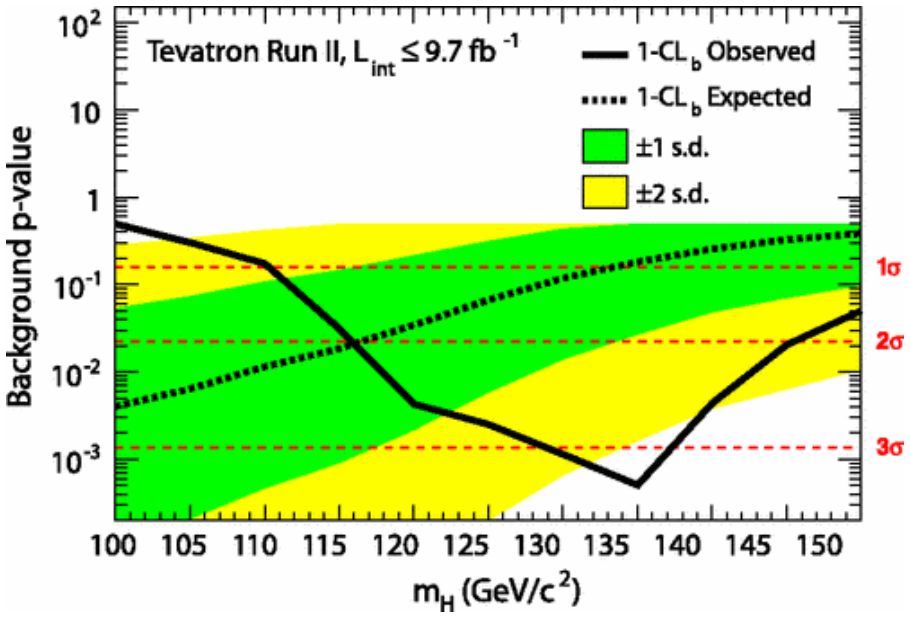

Figure 7.6: Background-only p-value as a function of Higgs boson mass for the Tevatron combined search.

The upper limit plot and the p-value test plot for the Tevatron combination are shown in Figure 7.7 and Figure 7.8 respectively.

In the limit plot, when interpreted in the same way as the previous sections, the standard model Higgs boson is excluded from 90-109 GeV/c^2 and 149-182 GeV/c^2. Also, a broad excess is observed in the range of m_H from 115-140 GeV/c^2.

The significance of this excess is evaluated by computing the p-value against the background only hypothesis. In Figure 7.8, the expected p-value assuming the existence of 125 GeV/c^2 Higgs boson is also shown. The maximum observed local significance is 3.1 standard deviations. Moreover, the width of the dip in the observed p-values from 115-140 GeV/c^2 is consistent with the resolution of the combination of the $H \to bb$ and $H \to WW$ channels, as illustrated by the injected signal curves in the same figure.

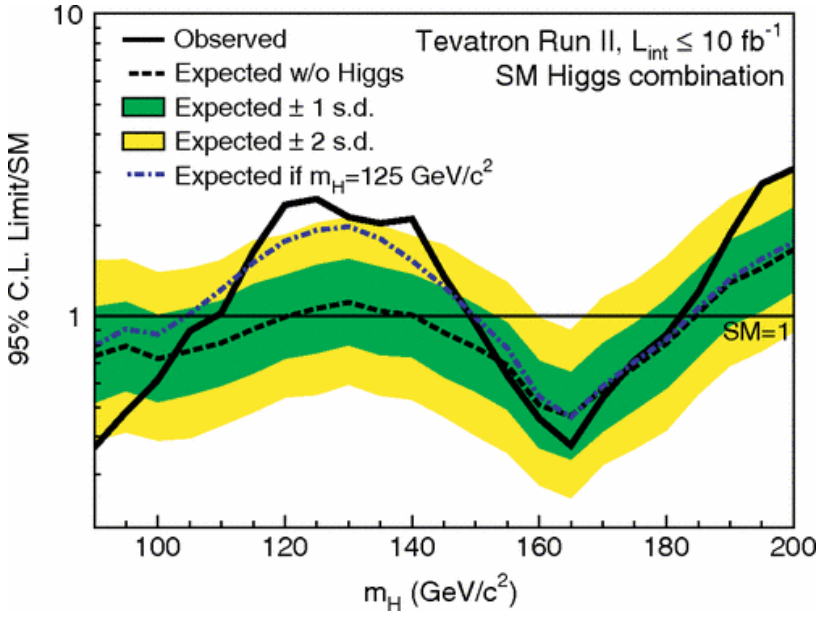

Figure 7.7: The Tevatron combination result for the SM Higgs. The upper limit of the 95% credibility level of Higgs boson production as a function of Higgs boson mass.

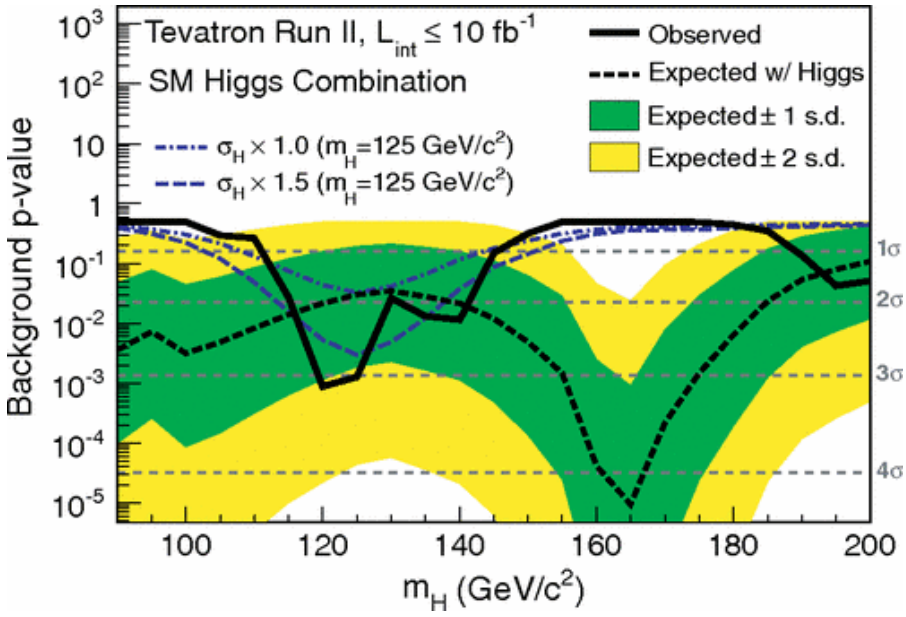

Figure 7.8: The Tevatron combination result for the SM Higgs. The background-only p-value as a function of Higgs boson mass.

Chapter 8

Conclusion

The Tevatron collider took its last proton-antiproton collision in September 2011. Despite the shutdown of the machine, many important physics results were produced in the following years based on its unique data set.

The top priority after the Tevatron shutdown was to update the Higgs boson search to the full data set. Several improvements were implemented in the last iteration compared to the previous rounds of analyses. For the *WH* search, we worked to update to the full data set, incorporate a new *b*-tagging algorithm, and integrated new trigger paths into the analysis for the first time. By including the gap lepton trigger and the inclusive trigger for CEM/CMUP, a major contribution from this thesis work, the overall lepton acceptance was increased by about 5%.

Moreover, the CDF *WH* analysis is the most sensitive channel in the low mass range among all the Higgs boson searches at the Tevatron. By combining all of the searches for the Higgs boson at the Tevatron, we are able to claim evidence of the standard model Higgs boson and the first evidence for the Higgs boson decay into bottom quarks. In the $H \to bb$ channel, the Tevatron result from 2012 is still more significant than the LHC searches in this channel.

As stated in the previous chapters, the single top quark *s*-channel process shares the same final state as the *WH* process. It is natural to migrate all of the techniques developed for the *WH* search to the single top quark analysis. In addition, for the first time, we optimized the analysis to measure the *s*-channel production cross section. At the time of

this work, the s channel had never been observed, and due to the differences in particle content of the colliding beams, this process is even more difficult for the LHC experiments to measure compared to the Tevatron.

We measured the single top quark s-channel production cross section to be $1.41^{+0.44}_{-0.42}$ pb with an observed significance for this measurement of 3.8 standard deviations. For the first time, we found evidence of this process in the CDF data set, confirming the recent results from the D0 experiment.

Our result was an important component to a combination that includes another CDF measurement and the measurement done by the D0 experiment. The combined production cross section for the s-channel is $1.29^{+0.26}_{-0.24}$ pb, and the significance for the presence of the s-channel process is 6.3 standard deviations. This result is interpreted as the first observation of this rare process, and for the reason stated above, this measurement should remain the best in the world for years to come.

Bibliography

[1] Excerpt from http://en.wikipedia.org/wiki/Standard_Model.

[2] J. Beringer *et al.* (Particle Data Group), Phys. Rev. D **86**, 010001 (2012), and 2013 partial update for the 2014 edition.

[3] Fermilab. Tevatron Operations Rookie Books. Concepts Rookie Book. http://www-bdnew.fnal.gov/operations/rookie_books/Concepts_v3.6.pdf.

[4] N. Kidonakis, Phys. Rev. D **83**, 091503 (2011).

[5] R. G. Wagner, Tech. Rep. CDF-5456 (2003).

[6] U. Grunder *et al.*, Tech. Rep. CDF-8262 (2006).

[7] F. Abe *et al.* (CDF Collaboration), Phys. Rev. Lett. **74**, 2626 (1995).

[8] S. Abachi *et al.* (D0 Collaboration), Phys. Rev. Lett. **74**, 2632 (1995).

[9] T. M. P. Tait and C.-P. Yuan, Phys. Rev. D **63**, 014018 (2000).

[10] T. Aaltonen *et al.* (CDF Collaboration), Phys. Rev. Lett. **103**, 092002 (2009).

[11] V. M. Abazov *et al.* (D0 Collaboration), Phys. Rev. Lett. **103**, 092001 (2009).

[12] V. Abazov *et al.* (D0 Collaboration), Phys. Lett. B **705**, 313 (2011).

[13] S. Chatrchyan et al. (CMS Collaboration), J. High Energy Phys. 12 (2012) 035.

[14] G. Aad *et al.* (ATLAS Collaboration), Phys. Lett. B **717**, 330 (2012).

[15] G. Aad *et al.* (ATLAS Collaboration), Phys. Lett. B **716**, 142 (2012).

[16] S. Chatrchyan *et al.* (CMS Collaboration), Phys. Rev. Lett. **110**, 022003 (2013).

[17] V. Abazov *et al.* (D0 Collaboration), Phys. Lett. B **726**, 656 (2013).

[18] T. Aaltonen *et al.* ((CDF Collaboration)), Phys. Rev. Lett. **112**, 231804 (2014).

[19] S. Chatrchyan *et al.* (CMS Collaboration), Physics Letters B **716**, 30 (2012).

[20] G. Aad *et al.* (ATLAS Collaboration), Physics Letters B **716**, 1 (2012).

[21] T. Aaltonen *et al.* (CDF Collaboration and D0 Collaboration), Phys. Rev. Lett. **109**, 071804 (2012).

[22] C. S. Hill, Nucl. Instrum. Methods Phys. Res., Sect. A **530**, 1 (2004).

[23] A. Sill, Nucl. Instrum. Methods Phys. Res., Sect. A **447**, 1 (2000).

[24] A. Affolder *et al.*, Nucl. Instrum. Methods Phys. Res., Sect. A **453**, 84 (2000).

[25] T. Affolder *et al.*, Nucl. Instrum. Methods Phys. Res., Sect. A **526**, 249 (2004).

[26] S. Cabrera *et al.*, Nucl. Instrum. Methods Phys. Res., Sect. A **494**, 416 (2002).

[27] L. Balka *et al.*, Nucl. Instrum. Methods Phys. Res., Sect. A **267**, 272 (1988).

[28] S. Bertolucci *et al.*, Nucl. Instrum. Methods Phys. Res., Sect. A **267**, 301 (1988).

[29] M. Albrow *et al.*, Nucl. Instrum. Methods Phys. Res., Sect. A **480**, 524 (2002).

[30] G. Apollinari, K. Goulianos, P. Melese, and M. Lindgren, Nucl. Instrum. Methods Phys. Res., Sect. A **412**, 515 (1998).

[31] P. De Barbaro *et al.*, IEEE Trans. Nucl. Sci. **42**, 510 (1995).

[32] G. Ascoli *et al.*, Nucl. Instrum. Methods Phys. Res., Sect. A **268**, 33 (1988).

[33] T. Dorigo, Nucl. Instrum. Methods Phys. Res., Sect. A **461**, 560 (2001).

[34] A. Artikov *et al.*, Nucl. Instrum. Methods Phys. Res., Sect. A **538**, 358 (2005).

[35] R. Downing, N. Eddy, L. Holloway, M. Kasten, H. Kim, J. Kraus, C. Marino, K. Pitts, J. Strologas, and A. Taffard, Nucl. Instrum. Methods Phys. Res., Sect. A **570**, 36 (2007).

[36] B. Ashmanskas *et al.*, Nucl. Instrum. Methods Phys. Res., Sect. A **518**, 532 (2004).

[37] H. Lai, J. Huston, S. Kuhlmann, J. Morfin, F. Olness, J. Owens, J. Pumplin, and W. Tung, Eur. Phys. J. C **12**, 375 (2000).

[38] M. L. Mangano, F. Piccinini, A. D. Polosa, M. Moretti, and R. Pittau, J. High Energy Phys. 07 (2003) 001.

[39] S. Alioli, P. Nason, C. Oleari, and E. Re, J. High Energy Phys. 09 (2009) 111
Using CTEQ61 [69] parton distribution functions.

[40] R. Brun, F. Carminati, and S. Giani, Tech. Rep. CERN-W5013 (1994).

[41] G. Grindhammer, M. Rudowicz, and S. Peters, Nucl. Instrum. Methods Phys. Res., Sect. A **290**, 469 (1990).

[42] F. Snider (CDF Collaboration), Nucl. Instrum. Methods Phys. Res., Sect. A **566**, 133 (2006).

[43] C. Gerald *et al.*, Tech. Rep. CDF-5293 (2000).

[44] A. Bhatti *et al.*, Nucl. Instrum. Methods Phys. Res., Sect. A **566**, 375 (2006).

[45] T. Aaltonen *et al.* (CDF Collaboration), Phys. Rev. D **88**, 092002 (2013).

[46] T. Aaltonen, A. Buzatu, B. Kilminster, Y. Nagai, and W. Yao (CDF Collaboration, D0 Collaboration), (2011), arXiv:1107.3026 [hep-ex] .

[47] T. Aaltonen *et al.* (CDF Collaboration), Phys.Rev. **D82**, 112005 (2010), arXiv:1004.1181 [hep-ex] .

[48] A. Buzatu, A. Warburton, N. Krumnack, and W.-M. Yao, Nucl. Instrum. Methods Phys. Res., Sect. A **711**, 111 (2013).

[49] F. Sforza, V. Lippi, and G. Chiarelli, J. Phys. Conf. Ser. **331**, 032045 (2011).

[50] J. Freeman, T. Junk, M. Kirby, Y. Oksuzian, T. Phillips, F. Snider, M. Trovato, J. Vizan, and W. Yao, Nucl. Instrum. Methods Phys. Res., Sect. A **697**, 64 (2013).

[51] D. Acosta *et al.* (CDF Collaboration), Phys. Rev. D **71**, 052003 (2005).

[52] D. Acosta *et al.* (CDF Collaboration), Phys. Rev. D **72**, 032002 (2005).

[53] P. Mastrandrea, *Study of the heavy flavour fractions in z+jets events from proton-antiproton collisions at energy = 1.96 TeV with the CDF II detector at the Tevatron collider*, Ph.D. thesis, Siena University (2008).

[54] J. Freeman, W. Ketchum, J. Lewis, S. Poprocki, A. Pronko, V. Rusu, and P. Wittich, Nucl. Instrum. Methods Phys. Res., Sect. A **663**, 37 (2012).

[55] A. Hoecker *et al.*, PoS **ACAT**, 040 (2007).

[56] T. Aaltonen and other (CDF Collaboration), Phys. Rev. Lett. **100**, 102001 (2008).

[57] R. Brun and F. Rademakers, Nucl. Instrum. Methods Phys. Res., Sect. A **389**, 81 (1997), see also http://root.cern.ch/.

[58] D. Acosta *et al.*, Nucl. Instrum. Methods Phys. Res., Sect. A **494**, 57 (2002).

[59] A. Abulencia *et al.* (CDF Collaboration), Phys. Rev. D **73**, 032003 (2006).

[60] T. Aaltonen *et al.* (CDF Collaboration), Phys. Rev. Lett. **112**, 231805 (2014).

[61] T. Aaltonen *et al.* (CDF Collaboration and D0 Collaboration), Phys. Rev. Lett. **112**, 231803 (2014).

[62] T. Aaltonen *et al.* (CDF Collaboration), Phys. Rev. Lett. **109**, 111804 (2012).

[63] T. Aaltonen *et al.* (CDF Collaboration), Phys. Rev. Lett. **109**, 111803 (2012).

[64] T. Aaltonen *et al.* (CDF Collaboration), Phys. Rev. Lett. **109**, 111805 (2012).

[65] T. Aaltonen *et al.* (CDF Collaboration), Phys. Rev. Lett. **109**, 111802 (2012).

[66] L. Lyons, Ann. Appl. Stat. **2**, 887 (2008).

[67] T. Aaltonen *et al.* (CDF Collaboration), Phys. Rev. D **88**, 052013 (2013).

[68] T. Aaltonen *et al.* (CDF Collaboration and D0 Collaboration), Phys. Rev. D **88**, 052014 (2013).

[69] D. Stump, J. Huston, J. Pumplin, W.-K. Tung, H.-L. Lai, S. Kuhlmann, and J. F. Owens, J. High Energy Phys. 10 (2003) 046.